Strål
säkerhets
myndigheten
Swedish Radiation Safety Authority

Author: Ki-Bok Min
Jaewon Lee
Ove Stephansson

Technical Note

2013:37

Rock Mechanics –

Evolution of fracture transmissivity within different scenarios in SR-Site – Main Review Phase

Report number: 2013:37 **ISSN:** 2000-0456
Available at www.stralsakerhetsmyndigheten.se

SSM perspektiv

Bakgrund

Strålsäkerhetsmyndigheten (SSM) granskar Svensk Kärnbränslehantering AB:s (SKB) ansökningar enligt lagen (1984:3) om kärnteknisk verksamhet om uppförande, innehav och drift av ett slutförvar för använt kärnbränsle och även inkapslingsanläggning. Som en del i granskningen ger SSM konsulter uppdrag för att inhämta information och göra expertbedömningar i avgränsade frågor. I SSM:s Technical Note-serie rapporteras resultaten från dessa konsultuppdrag.

Syfte

Det övergripande syftet med projektet är att ta fram synpunkter på SKB:s säkerhetsanalys SR-Site för den långsiktiga strålsäkerheten hos det planerade slutförvaret i Forsmark. Syftet med detta projekt är att undersöka och bedöma möjliga variationer av bergsprickornas transmissivitet (genomströmnings-förmåga) som en följd av de belastningar som kommer att verka på slutförvaret. Projektet utvärderar SKB:s antaganden gällande bergsprickornas transmissivitet, vilka ligger till grund för de belastningsscenarier som SKB har föreslagit för SR-Site och i sin tillståndsansökan om att få bygga ett slutförvar för använt kärnbränsle i Forsmark.

Författarnas sammanfattning

Detta granskningsuppdrag består av en litteraturstudie samt oberoende modellering för att bedöma betydelsen av transmissivitetsförändringar hos bergsprickor, driven av skjuvbelastning på grund av förhållandena i SKB:s termiska, glaciala och jordbävning belastningsscenarier för ett KBS-3-förvar vid Forsmark.

Rapportens inledande del består av en genomgång av SKB:s laboratorieexperiment på skjuvinducerad sprickutvidgning samt en litteratursammanställning av kunskapsläget gällande bergsprickors transmissiviteten vid normal- och skjuvbelastning. SKB:s laboratorieförsök på bergsprickor från Forsmark visar att dilatationen (ökad öppning) av sprickor i samband med skjuvbelastning är betydande. I likhet med SKB:s arbete visar den internationella litteraturen att redan små skjuvdeformationer av bergsprickor under normalspänningar upp till 20 MPa leder till en bestående ökningar i transmissiviteten och att denna ökning kan ha betydelse för radionuklidtransporten under den termiska och långsiktiga utvecklingen av slutförvaret.

Den andra delen av rapporten beskriver resultaten från egna modelleringar av transmissivitetsförändringar pga. termiskt inducerad skjuvning av sprickor i slutförvaret. Generiska sprickor, verkliga spricknät från Forsmark samt stora deformationszoner på långt avstånd från slutförvaret har studerats med en kombination av diskreta elementmodeller med beräkningskoden UDEC och diskreta spricknätverksmodeller (DFN-modeller). Resultaten visar bl a att transmissiviteten kan öka upp till två tiopotenser för en spricka med en initiell spricköppning på 30 μm och att detta kan ske på ett avstånd av mer än 10 m från en deponeringstunnel. Både transmissivitetens magnitud och avstånd från en deponeringstunnel till en spricka där ökningen kan ske är större än vad SKB anger. Den ökade transmissiviteten till följd av skjuvningen är icke-reversibel vilket innebär att den ökade genomströmningen till följd av belastningen under uppvärmningsfasen kvarstår under avsvalnandet och senare. Denna permanenta ändring kan påverka buffertens och återfyllningens egenskaper och inverka på radionuklidtransporten och den långsiktiga säkerheten hos slutförvaret.

Den tredje och fjärde delen av rapporten behandlar transmissivitetförändring till följd av en glaciationscykel samt jordskalv från någon av de närliggande större deformationszonerna i Forsmarksområdet. Undersökningarna gjordes med samma DFN modeller som användes vid modelleringen av termiskt inducerad skjuvning av sprickor. Modelleringsresultaten visar att inverkan av belastningen från en inlandsis är mestadel elastisk och fullt reversibel. Inverkan av ett jordskalv simulerades genom syntetiska markrörelser på modeller med korta sprickor på 5, 10 och 15 m, vilket visar att en irreversibel ökning av spricköppning på upp till 20 μm sker när spänningsförhållandet är nära sprickans skjuvhållfasthet. Dock, för DFN modeller i närområdet av transporttunnel och deponeringshål visar modelleringsresultaten att en irreversibel spricköppning inte förekommer. Detta utesluter inte att enskilda sprickor med ogynnsam orientering i förhållande till rådande spänningstillstånd i berget kan genomgå irreversibel dilatation på grund av ett jordskalv. Det finns behov av ytterligare modellering av jordskalv för att studera effekten på transmissiviteten för olika DFN modeller.

Projekt information

Kontaktperson SSM: Flavio Lanaro
Diarienummer ramavtal: SSM2011-3631
Diarienummer avrop: SSM2013-2462-6
Aktivitetsnummer: 3030012-4062

SSM perspective

Background

The Swedish Radiation Safety Authority (SSM) reviews the Swedish Nuclear Fuel Company's (SKB) applications under the Act on Nuclear Activities (SFS 1984:3) for the construction and operation of a repository for spent nuclear fuel and for an encapsulation facility. As part of the review, SSM commissions consultants to carry out work in order to obtain information and provide expert opinion on specific issues. The results from the consultants' tasks are reported in SSM's Technical Note series.

Objective

The general objective of the project is to provide review comments on SKB's postclosure safety analysis, SR-Site, for the proposed repository at Forsmark. The objective was to evaluate the range of possible variation of fracture transmissivity of natural fractures at Forsmark due to the loading configurations covered by SKB's scenarios. The argumentations provided by SKB for supporting the assumptions about fracture transmissivity in SR-Site should be evaluated from the viewpoints of plausibility and coverage of all the possible loading cases.

Summary by the authors

The current review assignment consists of a literature review and independent modeling for assessing the importance of fracture transmissivity change especially driven by shear loading due to SKB's thermal, glacial and earthquake loading scenarios for the KBS-3 repository at Forsmark.

In the first part of the report, SKB's laboratory experiments on shear fracture dilation and extensive literature review on shear fracture dilation in-situ and in laboratory under moderate normal stress show that dilation can become important even under moderate normal stress of about 20 MPa. Importantly, the increase of transmissivity induced by shear dilation would not recover to its initial state after cooling of the repository because the process occurs at shear failure, as demonstrated by the experiments in the literature. This permanent change of transmissivity can impact on the safety assessment of the repository for issues related to buffer resaturation time and radionuclide transport.

In the second part of the report, a modeling study focuses on the transmissivity change from thermally-induced shearing of fracture around repository on three types of geometries with a single fracture, realistic Discrete Fracture Network (DFN) models for Forsmark, and a far-field model with large scale deformation zones at the Forsmark site. The thermal shearing analysis was conducted by means of a discrete element method code, UDEC. DFNs were independently generated based on the fracture data provided by SKB. It was shown that transmissivity increase can be up to 2 orders of magnitude for an initial fracture aperture of 30 μm. These large transmissivity changes can occur around 10 m from the deposition tunnel. This indicates that significant changes are possible anywhere between adjacent deposition tunnels because dilation occurs and shear stresses can exceed the frictional strength of the fractures and deformation zones. Furthermore, because the frictional strength of some fractures was exceeded, irreversible shear dilation occurs, which does not recover to its initial state in the models after cooling of the repository. The magnitude and spatial extent of the transmissivity change is greater than the investigations reported by SKB. The significance and limitation of the modeling was discussed in view of parameters from fracture characterization, two-dimensionality of the used DFNs and numerical code. In the far-field model, the gently dipping deformation zones were most prone to shear dilation under thermal loading.

The third and fourth part of the report concern the effect of glacial and earthquake loading on transmissivity change. Investigations were made on the same DFN models used for the thermal study. The effect of glaciation on fracture transmissivity change was negligible due to the fact that glacial loading were increased in an almost isotropic manner, which does not promote shear slip. Furthermore, induced shear displacements in the models recovered after the retreat of the ice, which indicates that shear behavior of the fractures during a glacial cycle is mainly elastic. Earthquake modeling was conducted by applying synthetically generated ground motion to the models surrounded by viscous boundaries. Earthquake loading on a conceptual model containing a single fracture with size of 5, 10 and 15 m shows that there can be up to 20 μm of permanent aperture increase when the stress condition is close to shear failure. This result shows that the effect of an earthquake needs to be investigated, not only in terms of canister integrity, but also in terms of fracture transmissivity change. Earthquake modeling on DFN models, however, showed that actual shear dilation is negligible due to the fact that fracture orientation is not favorable to shearing. Further systematic investigation may be required on the effect of various DFN statistics and earthquake conditions.

Project information

Contact person SSM: Flavio Lanaro
Reference: SSM2013-2462-6

Strål
säkerhets
myndigheten

Swedish Radiation Safety Authority

Author: Ki-Bok Min[1], Jaewon Lee [1], Ove Stephansson [2]

[1] Seoul National University, Seoul, Korea

[2] Stephansson Rock Consulting, Berlin, Germany

Technical Note

2013:37

Rock Mechanics –

Evolution of fracture transmissivity within different scenarios in SR-Site – Main Review Phase

Date: May 2015
Report number: 2013:37 **ISSN:** 2000-0456
Available at www.stralsakerhetsmyndigheten.se

Contents

1. Introduction

This assignment is part of Main Review Phase conducted by the Swedish Radiation Safety Authority (SSM) on the SR-Site safety assessment of the final disposal of spent nuclear fuel at the Forsmark in the application for construction license submitted by the Swedish Nuclear Fuel and Waste Management Company (SKB).

This assignment concerns the evaluation of ranges of possible variation of fracture transmissivity of natural faults and fractures at Forsmark due to the loading configurations covered by SKB's scenarios. The argumentations provided by SKB for supporting the assumptions about fracture transmissivity in SR-Site are evaluated from a point of view of plausibility and coverage of all the possible loading cases. Furthermore, independent analyses of the hydro-mechanical behavior of rock fractures are carried out, presented and discussed. Cases with explicit realizations of the Discrete Fracture Network models (DFN) are evaluated to infer the possible ranges of variation of transmissivity for the different fracture sets occurring at Forsmark. Relevant realizations of the DFN models used for the independent modelling were provided by SSM in agreement with other external experts in the field of fracture network description and simulation (see Appendix 2).

The evaluations of possible transmissivity ranges from the provided DFN model are related to the hydrogeological models used for determination of the groundwater flow into the deposition holes. The Authors have also investigated the loading scenarios in relation to their effects on fracture transmissivity with the purpose of highlighting possible omissions by SKB. In conjunction with the hydro-mechanical analyses, normal and shear displacements on rock fractures in the DFN realizations are evaluated for different scenarios presented in SR-Site, in particular to evaluate the cumulative evolution of fracture transmissivity resulting from the thermal, glacial and earthquake scenarios. The magnitude and regional extent of transmissivity change investigated by SKB have been evaluated and compared with the results by current independent study in view of safety assessment of geological repository.

An error in the DFN realizations that were input to an earlier version of this report was discovered on March 7, 2014. The error was corrected and new modelling simulations of the evolution of fracture transmissivity were carried out as reported here.

1.1. Background

Several studies have shown that shear displacement and dilation of fractures can be sources of mechanical instability and significant fluid pathways in fractured rock. The thermal stress generated from heat-generating spent nuclear fuel and nuclear waste is in the order of up to 20 MPa and this can alter the stress state around a repository (Figure 1a), generate slip along existing fractures and induce changes of transmissivity. While the effect of the excavation is expected to be produced in the near-field, which means within a few times of the equivalent diameter of the repository tunnel, the influence of thermal stresses will reach mid- and far-field, which can be a few hundred meters from the peripheries of a repository. A field investigation by Barton et al. (1995) supports the statement that critically-stressed fractures are the ones carrying a major portion of the fluid flow in the rock mass. A similar finding was numerically demonstrated by Min et al. (2004). In a deep geological repository, thermal stresses are generated due to the confined nature of the rock mass at depth and they can be a source of shear slip and dilation of faults and fractures in the repository area (Min et al., 2013). Results from the study by Min et al. (2013) shows the thermal stress evolution, the state of stress after 100 years of disposal plotted as Mohr Circle and the shear slip zone due to thermal stresses based on fracture data from Forsmark (Figure 1). It was also concluded that "thermo-shearing", which is the phenomenon of shear displacement and dilation of faults and fractures due to thermal loading, is an important mechanism to be studied to ensure the safe disposal of nuclear waste in deep geological repositories (Min et al., 2013).

The transmissivity change associated with thermo-shearing is also expected to affect the pattern of fluid flow underground and is especially important since increased transmissivity due to shear dilation may not be reversible during the cooling phase of the repository. The candidate site at Forsmark proposed by SKB indicates a high stress ratio (i.e. the ratio of major principal stress to minor principal stress) and this implies that many fractures in the site area are critically or nearly-critically stressed under the current stress state according to SKB's site investigations (Glamheden et al., 2007). This means that even a slight change of stress can trigger a shear slip. Furthermore, the sparsely fractured rock at Forsmark will have relatively high elastic modulus and this will induce higher thermal stresses. It is noted that thermal loading of the repository occur in the far-field at relatively early time after closure (about 1,000 years) and has a direct effect on the radionuclide transport and overall performance of the repository.

Ice loading due to a glaciation and occurrence of earthquakes also inevitably alters the state of stress in the rock mass resulting in the shear slip of fractures. The analysis of the effect of earthquakes on the transmissivity change is necessary given that most of previous earthquake analyses focus on canister integrity resulting from fracture shear displacement (e.g. Fälth et al., 2010). Although small earthquakes may not affect the large-scale integrity of the repository, they can possibly induce notable transmissivity changes by shear slip. Therefore, the cumulative effect of thermal, earthquake and glacial loading deserves a systematic investigation based on realistic DFN models.

In summary, the change of transmissivity will have an impact on the performance assessment of a deep geological repository, and there is not yet in SKB documentation a complete quantitative analysis related to the transmissivity change induced by the thermal, glacial and earthquake scenarios.

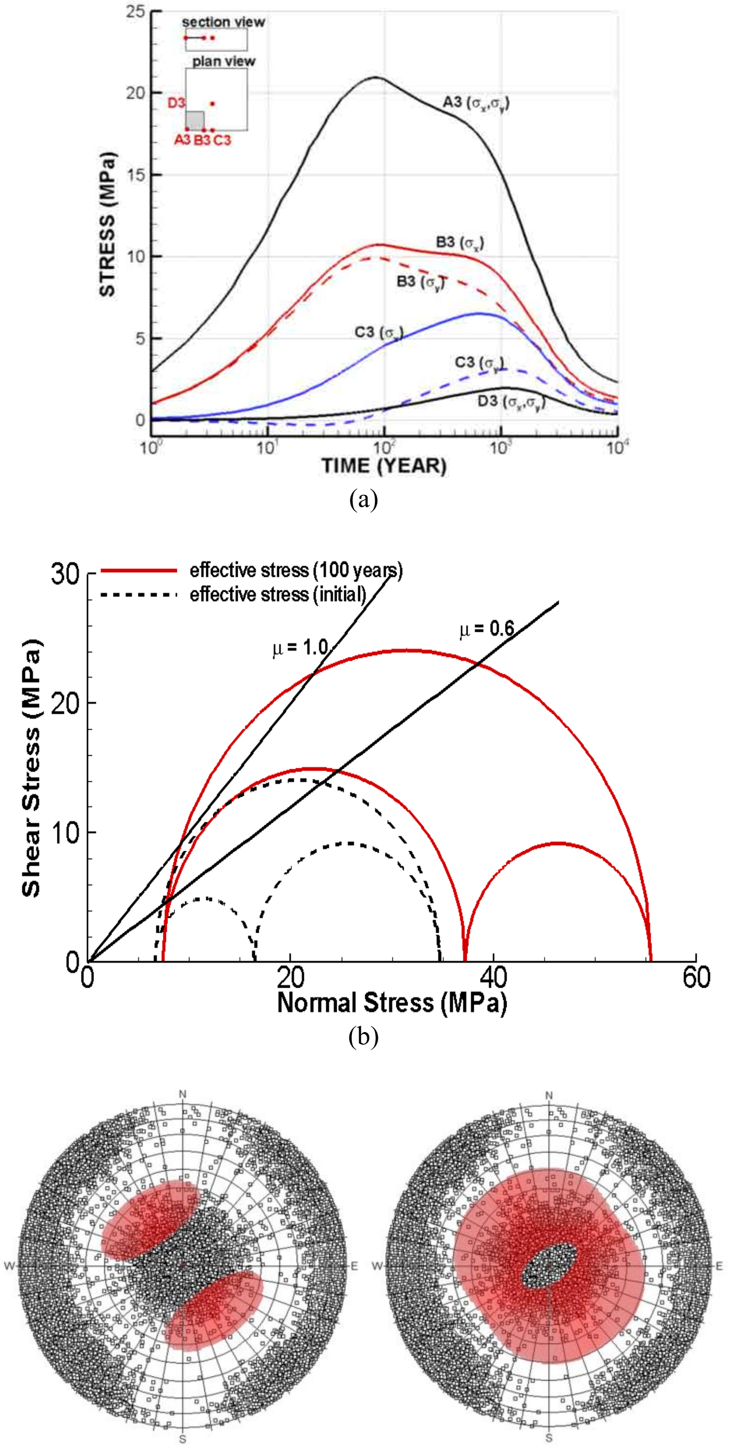

(a)

(b)

Initial state

After 100 years

(c)

Figure 1. The geological repository performance for shear slip potential. (a) evolution of notable compressive stresses at selected points at a repository level of about 400 m, (b) initial stress and stress after 100 years, and (c) shear slip zone shown in stereonet at an initial state and after 100 years (Min et al., 2013).

1.2. Scope of the current assignment

This study brings up technical issues that were not covered in sufficient detail by SKB for the construction license application of the final repository for spent nuclear fuel at Forsmark. The following tasks related to evolution of fracture transmissivity within different scenarios in SR-Site were performed for this study:

- Task 1. Literature review on the shear dilation of fractures in laboratory and in situ under moderate normal stress (5 to 25 MPa).

- Task 2. Transmissivity evolution for the thermal phase of the repository:
    1. Transmissivity change in a conceptual model
    2. Transmissivity change in the near-field DFN model from Forsmark
    3. Transmissivity change in far-field model from Forsmark

- Task 3. Transmissivity evolution for the glacial phase of the repository:
    1. Transmissivity change in a conceptual model
    2. Transmissivity change in the near-field DFN model from Forsmark

- Task 4. Transmissivity evolution for an earthquake occurring close to the repository:
    1. Transmissivity change in a conceptual model
    2. Transmissivity change in the near-field DFN model from Forsmark.

Task 1 undertakes a literature review of the existing knowledge about shear dilation in a fracture under moderate normal stress. Although SKB's license application did conduct a literature review and cited several important studies (Fransson, 2009), there is a significant underestimation of the shear dilation due to thermal stress.

Task 2 focuses on the transmissivity change due to thermally-induced shearing (thermo-shearing) of fractures around the repository. This task was conducted on three types of geometries, namely: (i) a conceptual model with a single fracture, (ii) a realistic DFN model and (iii) a far-field model with large scale deformation zones at the Forsmark site.

Task 3 focuses on transmissivity change from glacial loading around the repository. A conceptual model containing a single fracture was tested first. Main study was conducted on a realistic DFN model and was meant to reveal the effect of glaciation superimposed on the thermally induced change of transmissivity.

Task 4 deals with the effect of an earthquake on the transmissivity change around the repository. This task starts with a simple conceptual model containing a single fracture followed by applications on more realistic DFN model. The earthquake loading was applied at a few selected times on the repository model subjected to thermal and glacial loading.

The analyses in the current study were mainly conducted by applying the two-dimensional Discrete Element Method (DEM) code UDEC (Itasca, 2014). The study was conducted with an explicit consideration of fractures to overcome the limitation in SKB's work, which only used an elastic thermo-mechanical calculation and neglected shear dilation. While Min and Stephansson (2009) used a combination of thermo-mechanical continuum and mechanical DEM analyses, the current study directly uses the DEM code for coupled thermo-mechanical analyses. This approach gives a more realistic estimation of thermal shearing of rock fractures.

Key mechanisms focused on in this assignment include transmissivity increase due to shearing and irreversibility of displacements at shear failure of rock fractures. For dilated fractures under high normal stress, a permanent increase of transmissivity is anticipated contrary to the usual expectation that transmissivity will recovery after unloading. Figure 2 shows an illustration of the topics covered in this assignment.

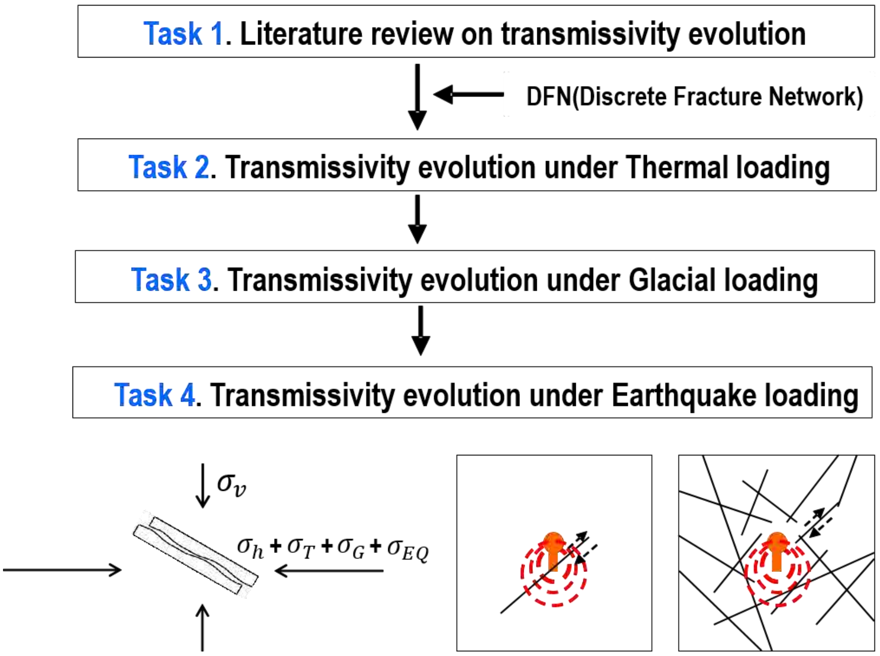

Figure 2. Illustration of the topics covered in this assignment.

2. Literature and laboratory studies on transmissivity evolution

2.1. SKB's presentation

2.1.1. Literature review conducted by SKB

Fransson (2009) reviewed previous works on the relationship between normal stress or normal stiffness and hydraulic aperture. Particular focus was given to experiences from field experiments. Those fields are listed below:

- Coaraze Laboratory, France (Cappa et al., 2006; Guglielmi et al., 2008a, b)
- Röda Sten Rock Laboratory, Sweden (Alm, 1999)
- Rock Mechanics Laboratory of Luleå University of Technology, Sweden (Rutqvist et al., 1998)
- Underground Research Laboratory (URL), Canada (Martin et al., 1990)
- Äspö Hard Rock Laboratory, Sweden (Rutqvist et al., 1998)
- Laxemar (HLX), Simpevarp (HSH), Ävrö (HAV), Äspö (HAS) (Rhén et al., 2008).

Figure 3 shows the compilation of equivalent hydraulic aperture and normal stiffness values by Fransson (2009).

Detailed field data on shear deformation and transmissivity were not found. However, the relationship between shear stress and deformation were derived by previous studies (Bandis et al., 1983; Barton et al., 1985; Olsson, 1998; Olsson and Barton, 2001). During fracture shear movements the aperture will change due to dilation. Especially transmissivity increases considerably for shear displacements exceeding a couple of millimeters, and transmissivity increase appears to be sensitive to normal load variations (Figure 4). SKB argues that most of the previous studies were conducted under low normal stresses. It is found that higher stress suppressed the joint dilation thus limiting the increase of hydraulic aperture. Gouge production would also tend to reduce transmissivity. Consequently, SKB assumed that transmissivity increases caused by shear dilation taking place under effective normal stresses higher than around 6 to 7 MPa were sufficiently small to be ignored.

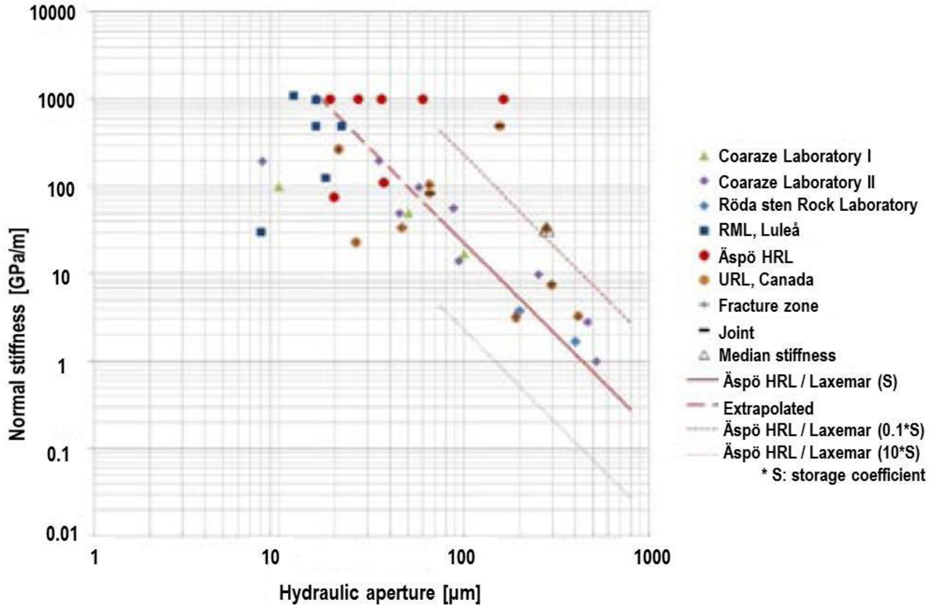

Figure 3. A compilation of equivalent hydraulic aperture and normal stiffness values (Fransson, 2009). Note that the original figure is slightly modified here to improve the resolution.

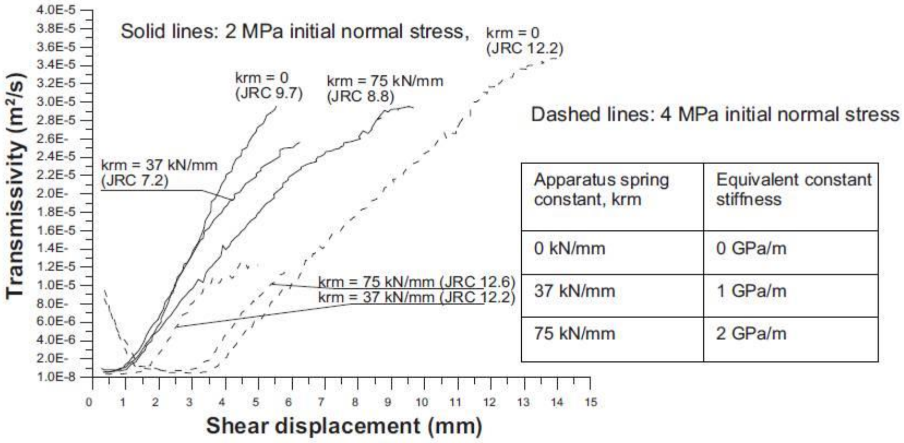

Apparatus spring constant, krm	Equivalent constant stiffness
0 kN/mm	0 GPa/m
37 kN/mm	1 GPa/m
75 kN/mm	2 GPa/m

Figure 4. Measured transmissivity of fractures of Ävrö granite as a function of shear displacement. The hydro-mechanical shear tests were conducted under different values of normal stiffness (Olsson, 1998).

On the other hand, Esaki et al. (1999) conducted direct shear tests under normal stress of 1, 5, 10 and 20 MPa using granite replicas. The measured hydraulic conductivity, which varied in proportion to the square of aperture, increased almost 2 orders of magnitude with shear displacement of 20 mm and normal stress of 20 MPa. The observed shear dilation was 2.9 mm and 1.0 mm under normal stress of 1 MPa and 20 MPa, respectively. These results show that change of shear dilation and hydraulic conductivity can be significant even under high normal stress. Note that the 2 orders of magnitude change in hydraulic conductivity corresponds to 3 orders of magnitude change in transmissivity.

2.1.2. Transmissivity change due to normal closure

An exponential expression (Liu et al., 2003) was used in the SR-Can assessment of thermo-mechanical and hydraulic rock processes (THM) (Hökmark et al., 2006).The exponential expression for aperture (e) versus normal stress was given by:

$$e = e_r + e_{\max} \exp(-\alpha\sigma_n) \qquad \text{Eq. (2.1)}$$

where e_r is the residual aperture, σ_n the effective normal stress whereas e_{max} and α are model parameters. The transmissivity T of individual fractures is a function of hydraulic aperture e given as:

$$T = \frac{\rho g}{12\mu} e^3 \qquad \text{Eq. (2.2)}$$

where g is the gravitational acceleration, ρ is the fluid density and μ is the dynamic viscosity of the fluid.

While SKB acknowledged the distinction between mechanical and hydraulic apertures, the mechanical aperture was used for the investigations because of the difficulty in obtaining accurate hydraulic apertures determinations in hard rock. This is considered to be a conservative and reasonable approach given the nature of the problem. Once stress-aperture relations are established, the relative transmissivity is given by the following expression using the cubic flow law:

$$T / T_0 = \left(e / e_0\right)^3 \qquad \text{Eq. (2.3)}$$

where T_0 and e_0 are the initial transmissivity and aperture, respectively.

SKB choses two normal stress-transmissivity models (denoted as Models A and B) to estimate normal stress-induced transmissivity changes. In both models, the residual aperture at high normal stress was based on reported transmissivity values for fractures below 400 m depth in the fracture domain FFM01 at Forsmark (Follin et al., 2007). Model A can be considered a “worst case” based on lower bound of the normal stiffness estimates of the fracture and is therefore very sensitive to normal stress variations. Model B is based on average fracture normal stiffness estimates and is less sensitive to variations in normal stress. Figure 5 shows the normal stress versus aperture relations and the parameter values for each stress-transmissivity model as indicated in Hökmark et al. (2010).

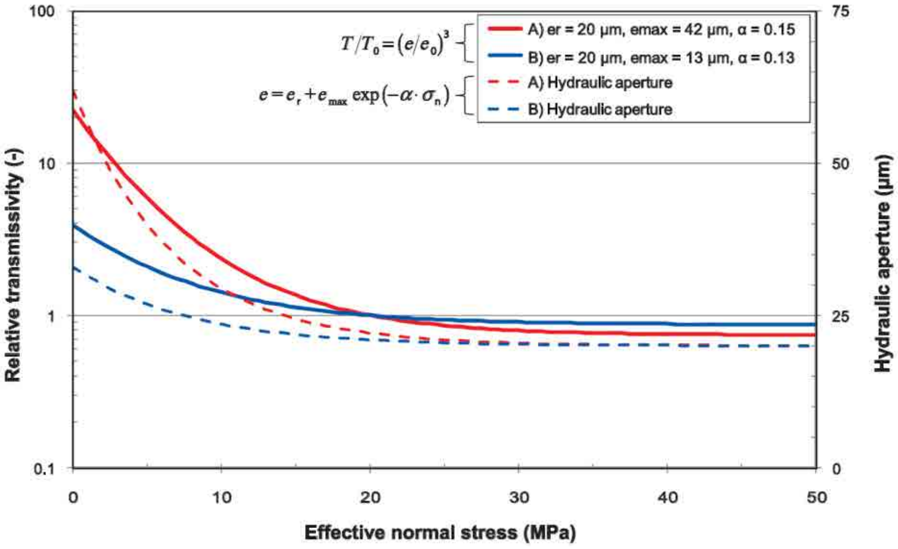

Figure 5. Relative transmissivity and hydraulic aperture versus effective normal stress used by SKB (Hökmark et al., 2010).

2.1.3. Transmissivity change due to shear stress

The dilation angle of a fracture can be calculated by means of Eq. (2.4) as suggested by Barton and Choubey (1977):

$$\phi = JRC\log(\frac{JCS}{\sigma_n}) \qquad \text{Eq. (2.4)}$$

where ϕ is dilation angle, *JRC* is Joint Roughness Constant, *JCS* is Joint wall Compression Strength, and σ_n is effective normal stress. The dilation angle can be reduced by half as necessary.

The actual change of the aperture induced by shearing can only be calculated from an elasto-plastic analysis with an explicit representation of the fractures after shear failure. Instead of conducting this type of analyses, SKB only estimated the maximum shear displacement (Δu) at given monitoring lines based on the stress drop τ_{drop} defined as the difference between the shear stress acting on the fracture plane and the strength of the fracture (Hökmark et al., 2010):

$$\Delta u = \frac{24}{7\pi G}\tau_{drop}a \qquad \text{Eq. (2.5)}$$

where G is shear modulus and a is the half fracture length.

It can be noted that there was no estimation by SKB of the transmissivity change due to shear dilation. The rationale for not doing this estimate is summarized as follows (Hökmark et al., 2010):

- There is no quantitative model to estimate the transmissivity change due to shearing of intact rock and fractures;

- The stress distribution in real fractures is different than that in the conceptual model, which makes it difficult to predict the dilation behavior;
- Dilation behavior under high normal stress regime (> 5 MPa) is sufficiently small to be ignored;
- Gouge production due to asperity damage will reduce the fracture transmissivity.

2.1.4. Measured dilation on samples from Forsmark

SKB did conduct laboratory tests on a number of fracture samples to measure the dilation behavior of rock fractures at Forsmark (Glamheden et al., 2007). Depending on the distance from the deposition tunnel and holes in the repository, normal stress acting on the fractures will vary between less than 5 MPa very close to the openings (less than a few meters), and as much as close to 40 MPa when the fracture plane is perpendicular to the maximum horizontal stress at the repository level.

Figure 6 shows the dilation angle obtained from laboratory tests on a total of 57 fracture specimens taken from different fracture domains and deformation zones at Forsmark. The empirical equation that provides the dilation angles is also reported. The laboratory tests show that the mean dilation angle under normal stress of 5 MPa and 20 MPa are 7.7 ° and 3.2 °, respectively (see Table 1).

The secant dilation angle ψ was determined for a shear deformation between 0.3 mm and 1.3 mm at the 0.5 MPa normal stress level, between 0.5 mm and 1.9 mm at 5 MPa and between 0.7 mm and 2.1 mm at 20 MPa, respectively. Many samples showed dilation angles higher than 10°. These laboratory results on rock samples from Forsmark agreed reasonably well with the existing empirical results (Figure 6b). Dilation angles of 7.7° and 3.2° corresponded to the normal opening at 14% and 6% of the maximum shear displacement, respectively. For example, when there is maximum shear displacement of 27.8 mm, which is expected to occur in the center of a 150 m long fracture (Hökmark, 2010, Figure 6-27), there will be around 3500 μm and 1500 μm shear dilation for 5 MPa and 20 MPa, respectively. These values imply that there will be at least 1 to 2 orders of magnitude increases of the aperture given that the initial aperture is usually less than 100 μm, and accordingly there can be 3 to 6 orders of magnitude changes in transmissivity given the cubic relations shown in Eq. (2.3).

Figure 7b shows the range of fracture shear displacement, dilation and associated relative fracture transmissivity. The maximum shear displacement considered for a fracture is 5000 mm, which is the threshold for canister damage due to earthquake loading in the repository. The larger the fracture size becomes, the greater the magnitude of the shear displacement and dilation. The expected relative transmissivity change for the maximum shear displacement three orders of magnitude for an initial aperture of 30 μm, and this can become up to five orders of magnitude for a dilation angle 15°. This figure demonstrates the importance of considering fracture shear displacement and dilation for thermo-mechanical, glacial and earthquake loading scenarios.

Obviously, there are issues regarding the size of fractures, the distinction between mechanical and hydraulic apertures and whether or not such dilation will hold throughout the full shear displacement. However, it is important to pay due attention to the measured dilations even under high normal stress as shown in Figure 6.

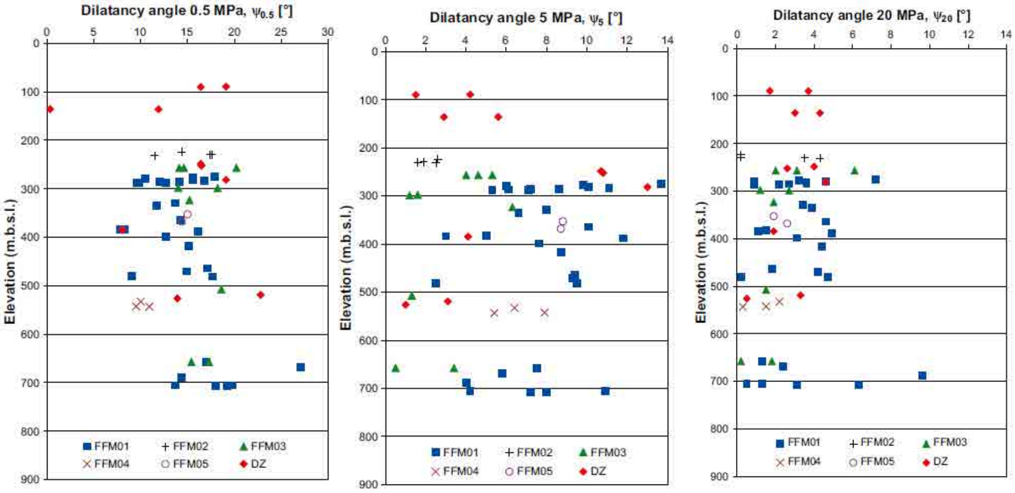

(a)

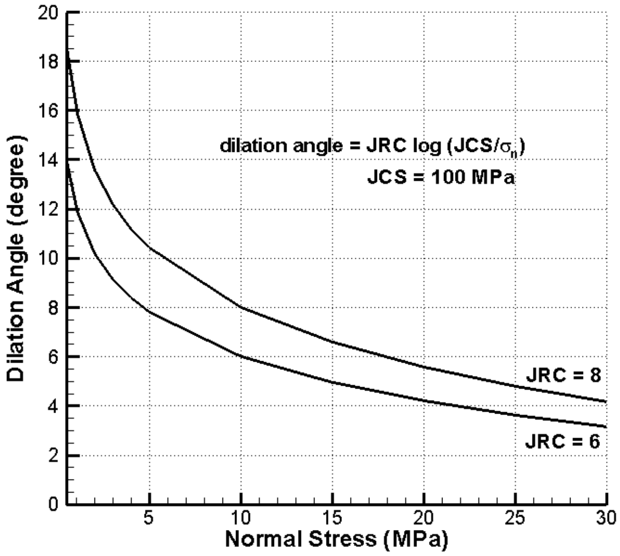

(b)

Figure 6. (a) the dilation angle from the laboratory tests on fracture samples taken at Forsmark (Glamheden et al., 2007) and (b) empirical equation for shear dilation for two JRC values (Barton and Choubey, 1977).

Table 1. Dilation angles from direct shear tests on fractures from the fracture domain FFM01 at Forsmark (Glamheden et al., 2007).

Normal load (MPa)	Mean (°)	Std. dev. (°)	Minimum (°)	Maximum (°)	Uncertainty of mean (%)
0.5	14.6	4.1	7.8	27.1	±10.2
5	7.7	2.7	2.5	13.7	±12.8
20	3.2	2.1	0.2	9.6	±23.9

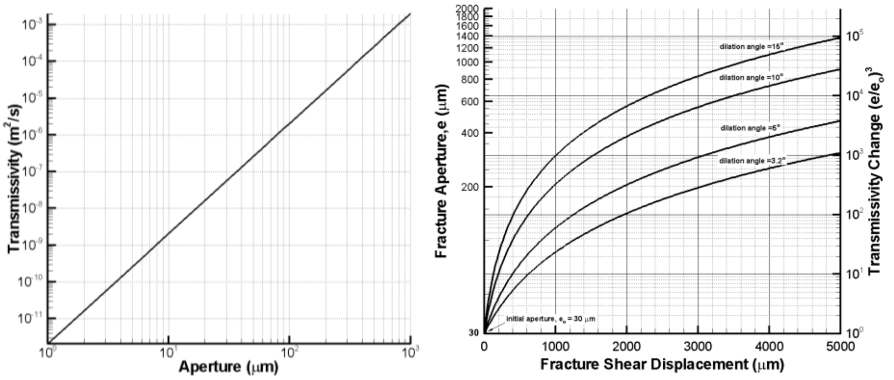

(a) (b)

Figure 7. Fracture shear displacement, aperture and transmissivity. (a) the relationship between aperture and transmissivity based on Eq. (2.2), (b) estimated fracture aperture and transmissivity change with respect to fracture shear displacement. Note that initial aperture is assumed to be 30μm in this plot.

2.2. Motivation of the assessment on SKB's literature and laboratory studies

2.2.1. Shear dilation behavior

The prediction of the dialtion phenomenon of irregular fractures subjected to direct shear loading has been addressed by numerous researchers. Figure 8 shows the compilation of dilation angle for different normal loads from direct shear tests (Bandis et al., 1981; Barton, 1982; Barton et al., 1985; Wibowo et al., 1994; Lee, 1999; Yeo et al., 1998; Homand et al., 2001; Huang et al., 2002). In Figure 8, the graph for the shear dilation angle at Forsmark is calculated by means of Eq. (2.4) with reduction factor by a half.

Data derived from several types of rock; granite (Barton, 1982; Barton et al., 1985; Lee, 1999), sandstone (Bandis et al., 1981), marble (Lee, 1999), and rock replicas (Homand et al., 2001; Huang et al., 2002; Wibowo, 1994; Yeo et al., 1998). All data except those from Barton et al. (1985) were obtained under low normal stress (less than 6 MPa), and the range of obtained dilation angles was between 0° and 20°.

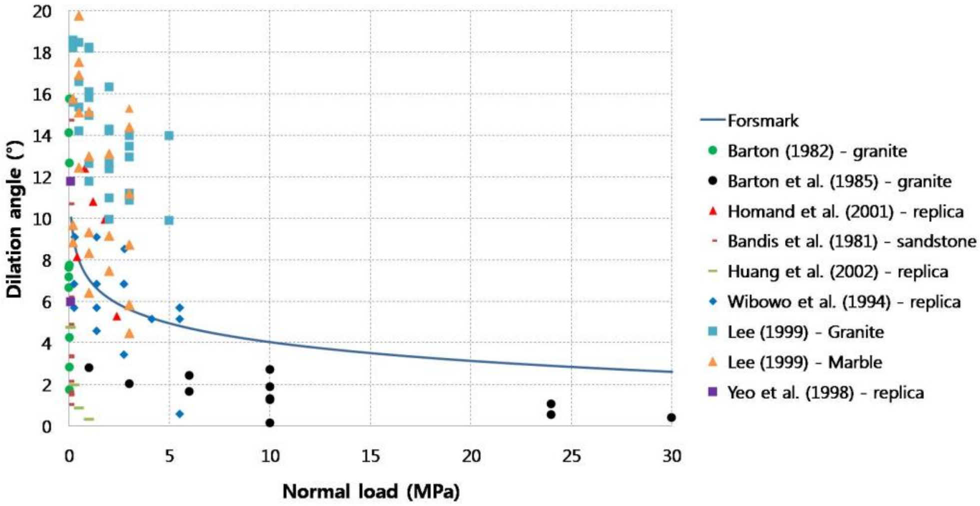

Figure 8. Compilation of the dilation angle versus normal load from direct shear tests. The solid line shows data from the Forsmark site.

Chen et al. (2000) measured the fracture volume and permeability under different confining pressures and shear displacements to study the effects of confining pressure and shear displacement on fracture aperture and permeability. Figure 9 shows the shear dilation angle as a function of confining pressure for a sample of granite with JRC equal to 9. The experimental results were compared to the dilation angle calculated with previous empirical equations by Barton et al. (1985) and Willis-Richards et al. (1996):

$$\phi_{dil}^{eff} = \frac{\phi_{dil}}{1 + 9\sigma_n' / \sigma_{nref}} \qquad \text{Eq. (2.6)}$$

where ϕ_{dil}^{eff} is effective shear dilation angle, ϕ_{dil} is shear dilation angle at zero stress, σ_n' is effective normal stress, and σ_{nref} is effective normal stress that gives 90% reduction in the compliant aperture. From Figure 9, it can be seen that sample had about 2.2° shear dilation angle under a confining pressure of 20 MPa, which is similar or lower than the confining stress at Forsmark.

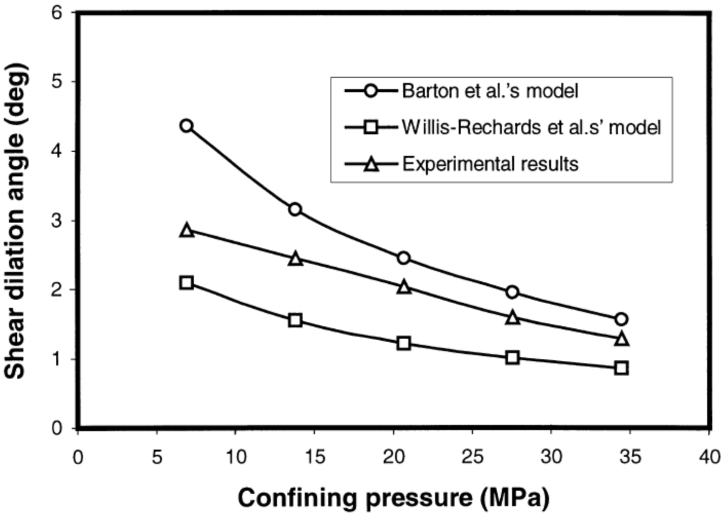

Figure 9. Shear dilation angle as a function of confining pressure for sample GO1 (Chen et al., 2000).

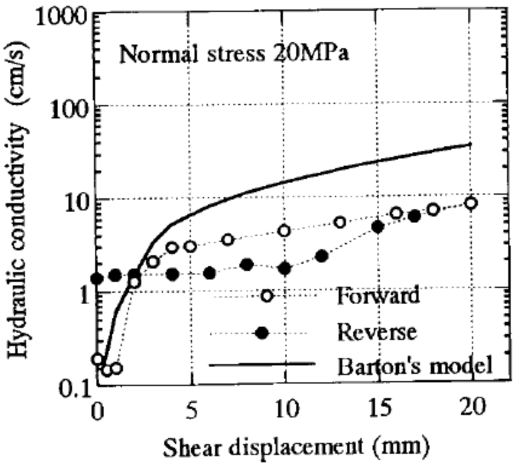

Figure 10. Hydraulic conductivity versus shear displacement of artificially created granite fracture at 20 MPa normal stress (Esaki et al., 1999).

Esaki et al. (1999) also showed the increase of hydraulic aperture, and increase of the hydraulic conductivity, versus shear displacement under 20 MPa normal stress from direct shear test (Figure 10), where the conductivity increased by two orders of magnitude. After reversing the movement, the hydraulic aperture did not decrease and return to its initial state, but left a residual aperture. That result means that shear dilation is an irreversible process. In the context of geological repository of nuclear waste, increased hydraulic aperture induced by thermal loading will remain unchanged even after temperature has decreased due to cooling of the canisters. In other words, in the vicinity of the repository, the shearing is not likely to be reversed after elasto-plastic fracture deformation has taken place.

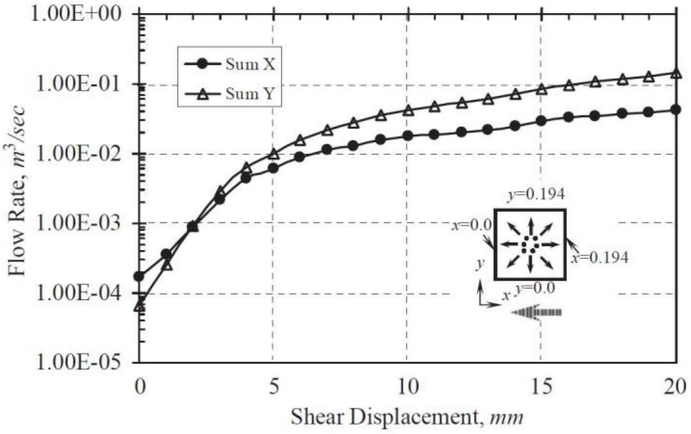

Figure 11. Total flow rates in different directions as a function of shear displacements (Koyama et al., 2006).

Figure 11 shows the test results of total flow rates in a fracture in different directions as a function of the shear displacements (Koyama et al., 2006). In this figure, the flow rate perpendicular to shear was larger than the flow rate parallel to shear. Flow channels newly formed perpendicularly to the shear direction were responsible for this particular behavior. Similar findings were also reported by Yeo et al. (1998) where anisotropy ratio decreased from 0.86 to 0.66 after 2 mm shearing indicating relatively larger flow perpendicularly to the shearing direction (the test was conducted on aperture replica of natural sandstone).

A numerical study conducted by Park and Song (2009) with the DEM code PFC showed that shear dilation is inhibited by large normal stresses. However, that study also showed that shear dilation is still significant enough to be considered.
Figure 12a show the layout of the numerical test used for the numerical analyses. That shear opening due to dilation can be up to 400 μm for a shear displacement of 1.6 mm under a normal stress of 15 MPa (Figure 12b). This finding also indicates that the existing empirical equation described by Eq. (2.4) may indeed underestimate actual shear dilation (Figure 12c).

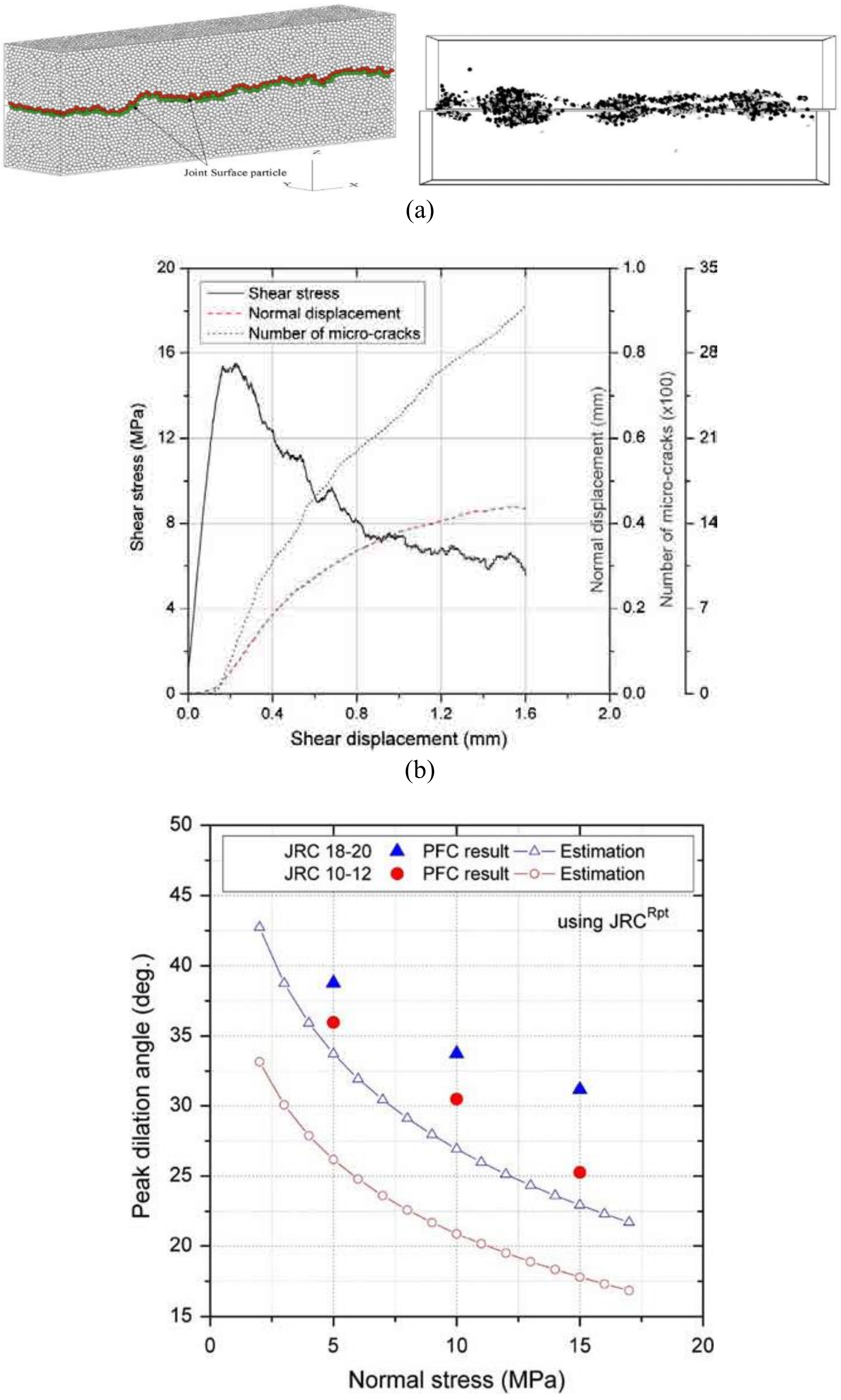

(a)

(b)

(c)

Figure 12. Numerical PFC-DEM simulations of dilation of a single fracture (Park and Song, 2009). (a) single fracture model, (b) shear stress-shear displacement versus normal displacement relationship, and (c) normal stress versus peak dilation angle relations for two different joint roughness coefficients.

2.2.2. Irreversibility of shear dilation

It has been observed that shear dilation can be irreversible, which means that hydraulic aperture would not recover to its initial state when reversing the shear load (Esaki et al., 1999). Due to the behavior of fractures in post-frictional failure, most of the induced shear displacements are not recovered even when the effect of thermal stress becomes negligible after cooling of the repository. We argue here that the irreversible nature of transmissivity change is important because any significant shear-induced transmissivity change can become permanent. Furthermore, total transmissivity can even be enhanced because of normal opening due to reduced normal stress during the thermal phase. A recent study by Min et al. (2013) showed through DEM modelling that the equivalent permeability of a rock block with size 5 m × 5 m actually increased by a factor of two due to contribution from the normal opening after cooling. There are few experimental or in situ observations about irreversibility of shear-induced transmissivity under full cycle of heating and cooling, and therefore further investigations including in situ test should be carried out to study the mechanisms and its extent.

2.3. The Consultants' assessment on SKB's literature and laboratory studies

The Authors have the opinion that SKB underestimates the transmissivity change under shear dilation. In fact, during SSM's Initial Review Phase, it was found (Min and Stephansson, 2012) that SKB had ignored shear-induced transmissivity changes under moderate normal stress, typically larger than 5 MPa (Hökmark et al., 2010). However, experimental and numerical studies support transmissivity changes of up to two orders of magnitude are expected for normal stress up to 20 MPa (see Esaki et al., 1999). For this reason, the laboratory experiments conducted by SKB contradicted their own modelling assumptions as presented in Hökmark et al. (2010). In conclusion, although the results of shear dilation tests performed by SKB show that dilation behavior is not sufficiently small to be ignored, the effect of shear dilation was not considered in any of the THM calculations by SKB (e.g. Hökmark et al., 2010).

As presented in the literature, hydraulic aperture can increase due to shear even under high normal stress (Chen et al., 2000; Esaki et al., 1999). Moreover, it has been observed that shear process in the rock fractures can be irreversible, which means that hydraulic aperture would not recover to its initial state when reversing the shear load (Esaki et al., 1999). Finally, it was found that fluid flow perpendicular to shear direction increased more than the flow parallel to shear direction (Koyama et al., 2006), which is not considered by SKB.

The Consultants' assessment is summarized as follows:

- The dilation angle of rock fractures obtained from direct shear tests conducted by SKB was 14.6 °, 7.7 ° and 3.2 ° for normal stress of 0.5 MPa, 5 MPa and 20 MPa, respectively. These results show that shear dilation should be considerable during thermal phase of the repository due to the fact that the normal stress variations at repository level are in the vicinity of 20 MPa. However, these data were not utilized for the safety assessment and their implications for long-term safety were not considered by SKB.

3. Modelling of the evolution of fracture transmissivity during the thermal phase of the repository

3.1. SKB's presentation

SKB divided the source of transmissivity changes into normal stress and shear stress, and transmissivity changes of the repository rock mass were then analyzed separately for thermal and glacial phases. Their results are presented in the following section focusing on the thermal phase, including the heating (about 1,000 years after closure) and cooling (up to about 10,000 years).

3.1.1. Transmissivity changes due to normal stress

The change of transmissivity due to normal stress was calculated by SKB based on effective normal stress at selected vertical monitoring lines in the repository. The monitoring scanline A, B and C are indicated in Figure 13 together with the calculated relative transmissivity change. The increase in transmissivity was found to be around a factor of 2 along different scanlines throughout the cooling period of the repository up to 10,000 years (Hökmark et al., 2010). It is important to note, however, that these results are entirely dependent on the chosen stress-transmissivity relation for rock fractures. As the fractures at around 400 m depth are already close to residual aperture/transmissivity, normal stress changes of several MPa do not impact on the aperture variation. This is the main reason for a small variation in transmissivity calculated by SKB. As the normal stress reduces with time due to the cooling, SKB assumes that the transmissivity will recover to its initial value.

When transmissivity change was analyzed in near-field fractures, the effect of relaxed stress around the tunnel had a direct impact on the transmissivity change up to a factor of 30 (Hökmark et al., 2006).

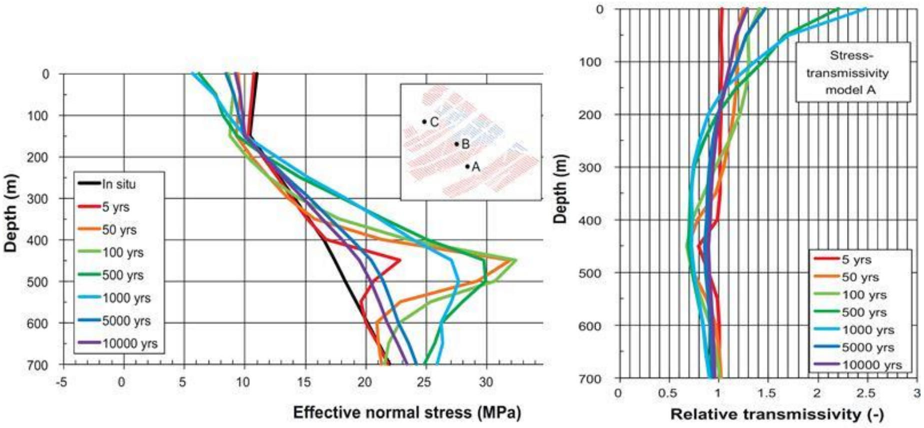

Figure 13. Effective normal stress as a function of depth along scanline B in the direction of the present-day minimum horizontal stress (left) and the relative transmissivity of vertical fractures striking perpendicularly to the present-day minimum horizontal stress (right) (Hökmark et al., 2010).

3.1.2. Transmissivity changes due to shear stress

There is no quantitative assessment of transmissivity change due to shearing in the SKB's investigation for different phases of the repository development with time. The only results presented by SKB is the quantification of the shear displacement along fractures of different size, which is indirectly estimated by means of Eq. (2.5) and based on calculation of shear stress from 3DEC modelling.

The Mohr Circle representation of the thermal stress change showed that the shear failure along the fractures can occur (Figure 14, left). Shear displacement with fracture half-lengths of 150 m was calculated to be 27.8 mm at 450 m depth on scanline A between two deposition panels (Figure 13 shows the location; Figure 14 right). As shear displacement is assumed proportional to the size of the fractures, the magnitude of displacement of smaller fractures can be readily scaled. For example, a fracture with 30 m diameter will undergo a shear displacement larger than 5 mm. Although dilation angles of 3.2° (based on normal stress 20 MPa; SKB, 2010, p. 38) or 10° (Fälth and Hökmark, 2006, p. 45) were used for the numerical simulation, it is not clear how this value was actually incorporated into the results. Importantly, this analysis shows that the shear displacement would recover to its initial value after 10,000 years indicating that SKB's model shows nearly elastic response of the fractures (see Figure 14).

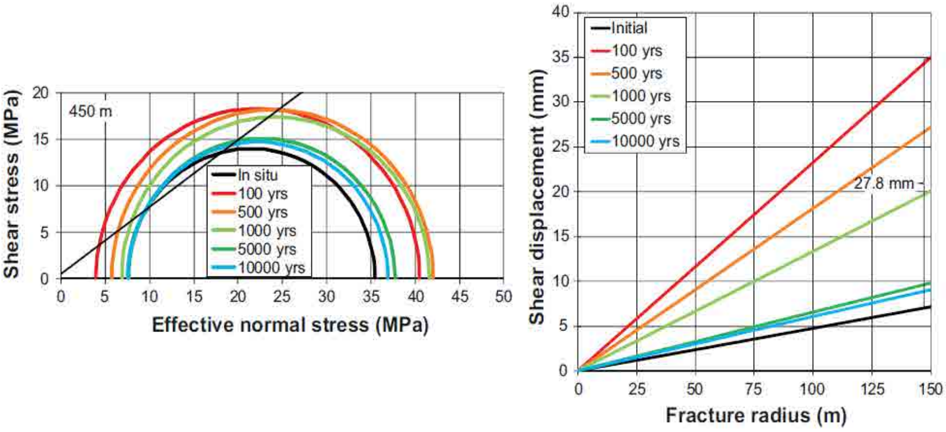

Figure 14. Stresses on modeled factures plotted on Mohr-Coulomb circles (left) and shear displacements as a function of the fracture radius (right) around a deposition tunnel at different times after closure of the repository (Hökmark et al., 2010).

3.1.3. Spatial extent of transmissivity changes

The regional extent of transmissivity change investigated by SKB is summarized in Figure 15. Hökmark et al. (2006) estimated that within a distance of 2 m from a depositions tunnel, the relative transmissivity may increase by up to two orders of magnitude. No changes were predicted elsewhere. This observation is applicable to the thermal phase of the repository. The changes of transmissivity in the near-field were mainly due to normal stress relaxation close to the tunnel opening, and the contribution of shear dilation was only qualitatively considered by Hökmark et al. (2010). Therefore, the spatial extent of transmissivity at larger scale has been totally overlooked by SKB in the region outside a distance of 2 m from the tunnel opening. It is also noted that the size of analyzed fractures was a few tens of meters and their orientation did not have bearing on fracture observations at the Forsmark site (Hökmark et al., 2010).

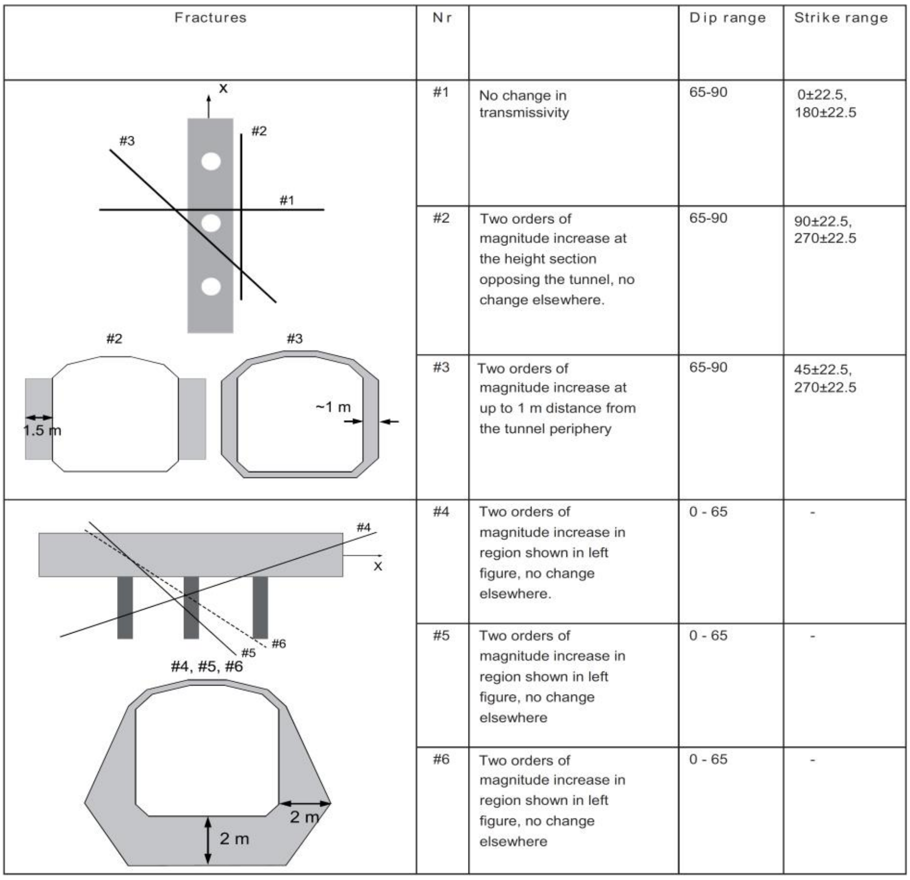

Fractures	Nr		Dip range	Strike range
	#1	No change in transmissivity	65-90	0±22.5, 180±22.5
	#2	Two orders of magnitude increase at the height section opposing the tunnel, no change elsewhere.	65-90	90±22.5, 270±22.5
	#3	Two orders of magnitude increase at up to 1 m distance from the tunnel periphery	65-90	45±22.5, 270±22.5
	#4	Two orders of magnitude increase in region shown in left figure, no change elsewhere.	0 - 65	-
	#5	Two orders of magnitude increase in region shown in left figure, no change elsewhere	0 - 65	-
	#6	Two orders of magnitude increase in region shown in left figure, no change elsewhere	0 - 65	-

Figure 15. Summary of the transmissivity changes calculated by SKB for the near-field of the repository. The shaded areas around the tunnel represent the spatial extent of volume with increased transmissivity (Hökmark et al., 2006; Hökmark et al., 2010).

3.2. Motivation of the assessment on the evolution of fracture transmissivity during the thermal phase based on independent TM modelling

For this review assignment, independent modelling of the behavior of the fracture network and the evolution of the fracture transmissivity during the thermal, glacial and earthquake loading was carried out by the Authors. Table 2 lists the conducted modelling in this study.

3.2.1. Data and geometry for the independent TM modelling

Data and geometry for modelling were taken from SKB’s repository Layout D2 (SKB R-08-83, 2009). The spacing between deposition tunnels is 40 m and the spacing between deposition holes in each tunnel is 6 m. The most likely values and orientations of in situ stress are based on the SKB’s data report (SKB TR-10-52, 2010). Therefore, it is assumed that the deposition tunnel axis is parallel to the orientation of maximum horizontal stress, which is 145° with respect to North as shown in Figure 16 a. The orientation of the minimum horizontal stress, which is shown as a green dot in Figure 16a, is 55° with respect to North. A true 3D-DFN model was cut through three sections. Firstly, the NE section in Figure 16b is the 2D section whose normal line is parallel to the maximum horizontal stress direction and to the direction of a deposition tunnel axis. Therefore, in the Authors' modelling, the NE section is subjected to the minimum horizontal stress and vertical stress. Similarly, the NW section is the plane subjected to maximum horizontal stress and vertical stress. Lastly, HZ section is subject to the maximum horizontal stress and minimum horizontal stress. These sections are indicated in Figure 16c. The magnitude of each of the in situ stresses used for the modelling is listed in Table 3 together with their stress gradients with depth. The initial temperatures at a depths of 400 m, 500 m and 600 m were 10.5 °C, 11.6 °C and 12.8 °C, respectively. The mechanical and thermal properties of rock mass and fractures around the deposition hole are summarized in Table 4 and Table 5.

Table 2. List of modelling cases for thermal, glacial and earthquake scenarios.

Scenario	2D section	DFN	Results
Thermal	Vertical (NE)	T_NE02	Section 3.2.5.1
		T_elNE02	Section 3.2.5.1
	Vertical (NW)	T_NW02	Section 3.2.5.2
	Horizontal	T_HZ02	Section 3.2.5.3
	Far-field	Deformation zone	Section 3.2.7
Glacial	Vertical (NE)	TG_NE02	Section 4.2.4.1
	Vertical (NW)	TG_NW02	Section 4.2.4.2
Earthquake	Vertical (NE)	TGEQ_NE02	Section 5.2.4.1
	Vertical (NW)	TGEQ_NW02	Section 5.2.4.2

Table 3. In-situ stress distributions at Forsmark used for independent TM modelling (from Hökmark et al., 2010). *z* is the depth.

For depth > 400m	**Unit**	**Stress**
Maximum horizontal stress (σ_H)	[MPa]	-29.5 - 0.023 · z
Minimum horizontal stress (σ_h)	[MPa]	-9.2 - 0.028 · z
Vertical stress (σ_v)	[MPa]	-0.0265 · z

Table 4. Thermal, thermo-mechanical and mechanical properties of the rock mass used for the independent TM modelling in this study (from Hökmark et al., 2010).

Material property	**Unit**	**Value**
Heat capacity	[MJ/(m^3·K)]	2.06
Mean thermal conductivity	[W/(m·K)]	3.57
Dimensioning thermal conductivity	[W/(m·K)]	2.9
Density	[kg/m^3]	2,700
Young's modulus	[GPa]	70
Poisson's ratio	[-]	0.24
Heat expansion coefficient	[1/K]	7.7 × 10^{-6}
Specific heat	[J/kg/°C]	762.96

Table 5. Mechanical properties of the rock fractures from domain FFM01 at Forsmark used for the independent TM modelling in this study (from Hökmark et al., 2010).

Material property	Unit	Value	Comment
Shear stiffness	[GPa/m]	34	
Normal stiffness	[GPa/m]	656	
Friction angle	[°]	35.8	
Dilation angle	[°]	3.2	
Cohesion	[MPa]	0.5	
Tensile strength	[MPa]	0	
Z-dilation	[m]	3×10^{-3}	Critical shear displacement when dilation stops
Residual aperture	[m]	2×10^{-5}	
Zero aperture	[m]	3×10^{-5}	

It is noted here that each 2D section can greatly reduce the true connectivity of the discrete fracture network (DFN). On the other hand, however, it is also noted that 2D DFN can overestimate the shear displacement compared to 3D models with DFN because 2D DFN sections implicitly assume infinitely long planar fractures in the direction perpendicular to the model plane.

Considering the symmetry of the deposition tunnel arrays, the width of the NE and NW model was chosen to be 40 m and its height to be 100 m, which provides a reasonable geometrical approximation for the temperature boundary conditions (Figure 17). In order to represent an array of deposition holes in a deposition tunnel in 2D NE section, one target deposition hole with a heat source, was located in the center of the model. In NW section, five deposition holes were presented along the tunnel direction. In NW section, heat sources were also adjusted due to the effect of two-dimensional analysis. Furthermore, in HZ section, the length of square is chosen as 70 m to reduce the effect of fixed temperature at boundaries. Five canisters within deposition holes were modeled as heat sources as shown in Figure 17c.

It is noted that explicit mechanical excavation was modeled only for the deposition tunnel in NE section. The excavation of deposition hole was not modeled in order to avoid complexity in the interpretation of results. This approach is justified given that the regional extent of stress concentration around the deposition hole is expected to be small in the order of less than 1 m. Furthermore, deposition tunnel in NW section cannot be modeled because deposition tunnel is through-going along the NW section. Therefore, the results obtained from thermomechanical analysis is affected mainly by thermal loading except for the region close to deposition tunnel in NE sections.

The transmissivity is calculated from the mechanical aperture based on Eq. (2.2) and its relationship is plotted in Figure 7a. It is noted that, for simplicity, no distinction has been made in this study between hydraulic and mechanical aperture. The analyses of all models were conducted using the two-dimensional discrete element code, UDEC (Itasca, 2009).

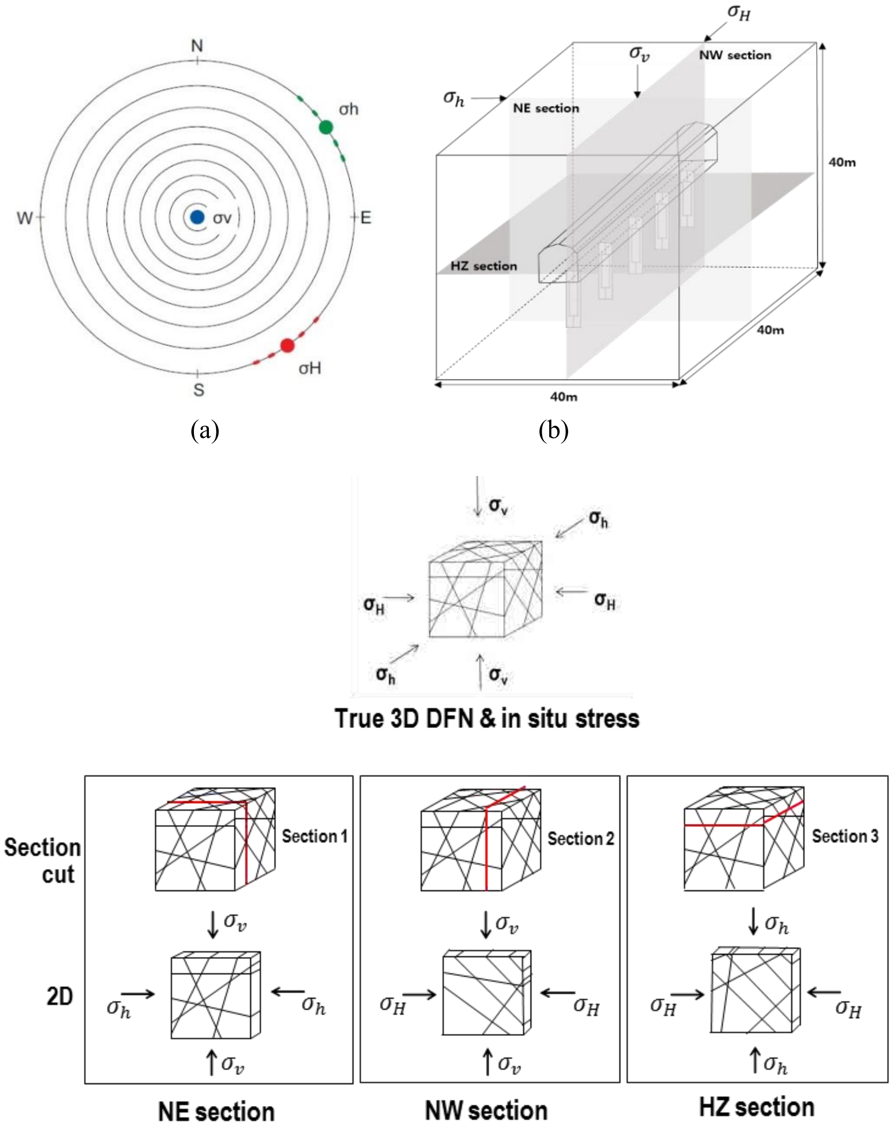

(a) (b)

(c)

Figure 16. In-situ stress orientation and the 3D DFN for the independent TM modelling. (a) mean value orientations (poles) and ranges of uncertainty (dashed lines) of the principal in situ stress components (from Hökmark et al., 2010); (b) scheme to cuts of the 3D DFN-model according to the principal stress planes NE, NW and HZ. (c) DFN sections of the 3D DFN and boundary in situ stresses.

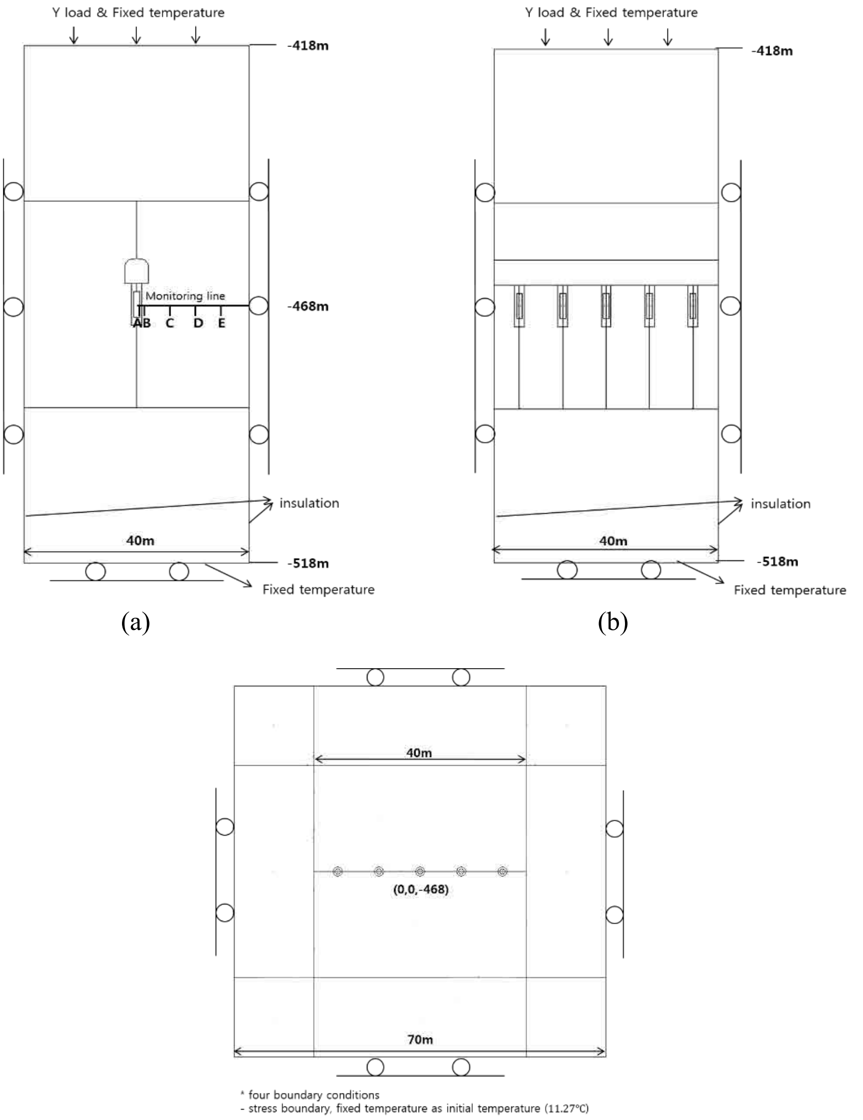

(a) (b)

(c)

Figure 17. Model geometry for TM modelling in this study. (a) the tunnel geometry and boundary conditions in the NE section. Five monitoring points A to E are placed on a horizontal line departing from the center of the canister at distances of 0.5251 m, 0.8751 m, 5.91 m, 10.35 m and 14.91 m, respectively; (b) tunnel geometry and boundary conditions in the NW section; (c) geometry of five deposition holes and boundary conditions in the HZ section. The size of the vertical section models is 40 m × 100 m (width × height). The size of the HZ section models is 70 m × 70 m (width × height).

3.2.2. Thermal loading

The stress distribution and the temperature of the rock mass will change due to heat released from the canisters with the spent fuel. The deposition holes are located at 468 m depth, and are represented as rectangular elements in the two-dimensional DEM model with UDEC. The heat generation by the canister power is a time-dependent function with given decay rate from an initial value $P(0)$. The decay of the canister power is applied as heat source using Eq. (3.1) and the coefficients t_i and a_i are listed in Table 6:

$$P(t) = P(0)\left\{\sum_{i=1}^{7} a_i \exp\left(\frac{-t}{t_i}\right)\right\} \qquad \text{Eq. (3.1)}$$

The function $P(0)$ and Eq. (3.1) are adapted in order to provide input data to the UDEC modells for a time period of 100,000 years. Figure 18 shows the resulting power function $P(t)$ used for the thermo-mechanical modelling. Heat generation starts with an initial value $P(0)$ of 1700 W for the first year, and decays nearly to zero after 10,000 years.

Coupled thermo-mechanical analysis was conducted with in situ stress and initial temperature distribution in accordance with data from the Forsmark site. TM analysis provided the evolution of temperature distribution and thermal stress. Figure 19 describes the temperature variation due to heat generation of the canister for 100,000 years. The variation of measured temperatures at five points A to E

Table 6. Canister power decay coefficients for Eq. (3.1) for SKB’s reference fuel (Hökmark et al. 2010).

Time interval *i*	***t_i* [years]**	***a_i* [-]**
1	20	0.060147
2	50	0.705024
3	200	-0.054753
4	500	0.249767
5	2000	0.025408
6	5000	-0.009227
7	20000	0.023877

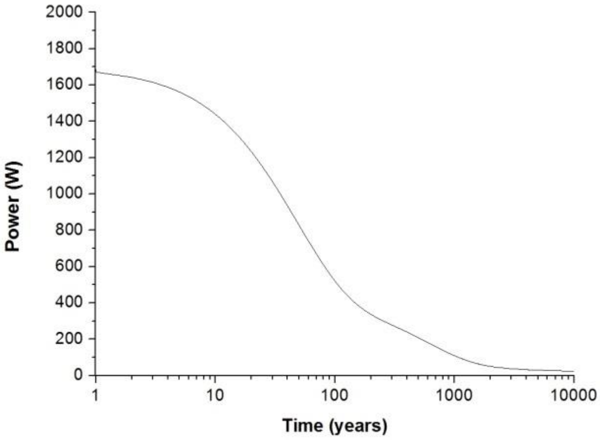

Figure 18. Decay of the generated heat power by one canister with time to be used for the UDEC modelling.

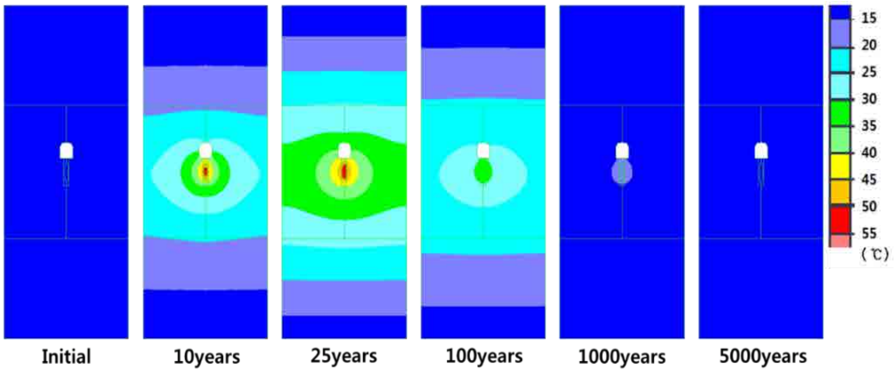

(a)

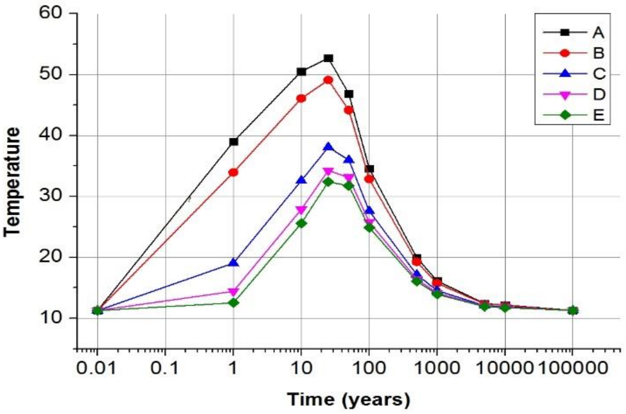

(b)

Figure 19. (a) temperature evolution in the various locations of the repository; (b) temperature versus time along the horizontal monitoring line at point A to E at a depth of 468 m across the repository.

along the horizontal line at 468 m depth is shown in Figure 17. The maximum temperature at each point occurs after 25 years and is presented in Figure 19b. As expected, the temperature increases most for monitoring points close to the canister. The horizontal and vertical stress distribution and displacement with time are provided in Figure A3-1 in Appendix 3. The results show that the elevated stress and displacement in the rock recover to their initial value after 5,000 years.

Further, the stresses at each monitoring point has its maximum magnitude at around 25 years after start of deposition, and returns to their initial in situ stress value after around 1,000 years. Especially the horizontal stress at the vicinity of the canister wall increases from around 22 MPa to around 50 MPa as shown in Figure 20a. The vertical stress shows different tendencies depending on the location as shown in Figure 20b. At point A, which is at the center of the deposition hole, the vertical stress increase was modest and about 10 MPa. However, most of the locations around the repository do not show notable increases in vertical stress because the overburden is free to move upwards, unlike the case for horizontal stress. In general, vertical stress does not vary much except below the deposition tunnel.

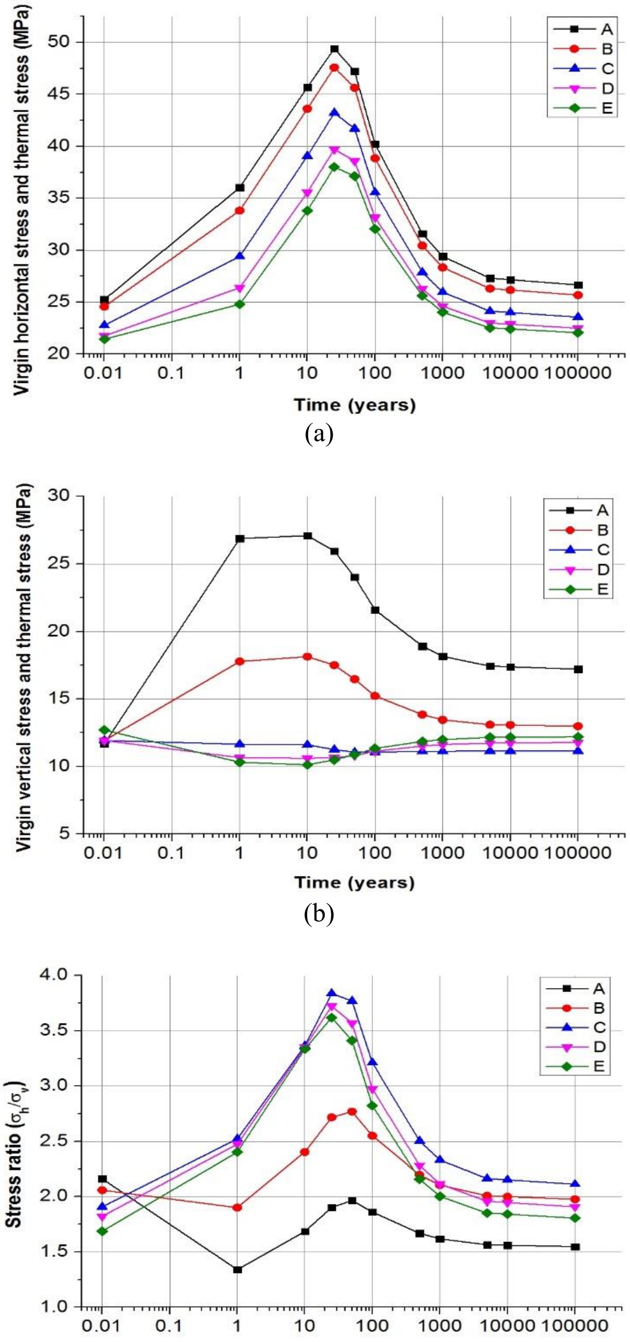

(a)

(b)

(c)

Figure 20. Thermal stress evolution at control point A to E of the NE section at a depth of 468 m in Forsmark. (a) minimum horizontal stress, (b) vertical stress, (c) stress ratio.

The ratio of the horizontal stress to vertical stress can be also studied with time. As shown in Figure 20c, the stress ratio becomes greater than 2.5, which is a critical value that triggers shear slip on fractures in all monitoring points (except for the location inside the deposition hole). From these results, it is noted that the stress ratio can be high enough to produce shear slip on fractures at points about 15 m away from the canister. This observation provides a good indicator for evaluating the spatial extent of fracture transmissivity change induced by shear slip on rock fractures.

3.2.3. Conceptual model of fracture transmissivity evolution during the thermal phase

Before conducting the DFN-DEM analysis with DFN data from Forsmark, conceptual models with a single fracture were used to gain an insight into shear behavior during the thermal loading phase. A conceptual model was studied with a rock block of size 40 m × 40 m containing a single fracture as shown in Figure 21a.

According to Pollard and Segall (1987), the relative shear displacement (Δu) within a fracture is calculated using the following equation:

$$\Delta u = \left(\tau_r - \tau_c\right)\frac{2\left(1-\nu\right)}{G}\sqrt{a^2 - x^2} \qquad \text{Eq. (3.2)}$$

where τ_r is the remote shear stress, τ_c is the shear stress on the crack, ν is the Poisson’s ratio and G is shear modulus of the rock, a is half fracture length, and x is the distance from the center of the fracture. Note that this equation is a 2D version of Eq. (2.5). $(\tau_r - \tau_c)$ is 5 MPa in this model, and the friction angle and cohesion of the fracture are assumed to be zero.

Comparison between the UDEC and analytical result from Eq. (3.2) as presented in Figure 21b that shows there is a good match between the two. The redistributed directions of the principal stresses at the vicinity of the fracture are shown in Figure 22.

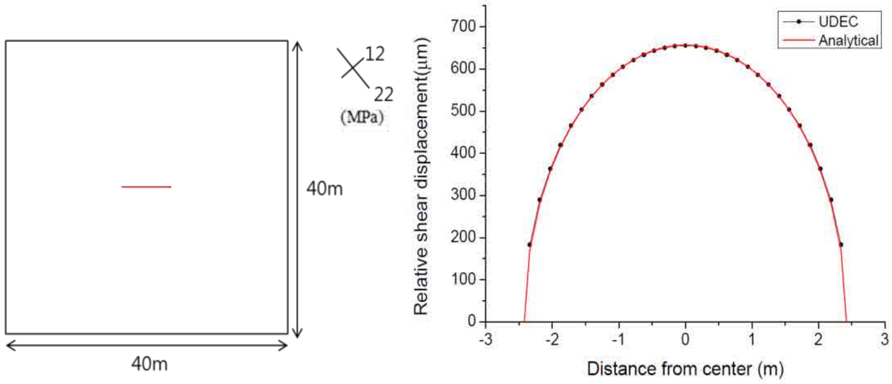

(a) (b)

Figure 21. (a) generic model in the size of 40 m x 40 m containing a single fracture with half-length of 4.84 m. The boundary stress condition is indicated in the top right corner; (b) relative shear displacement versus distance from center of the fracture.

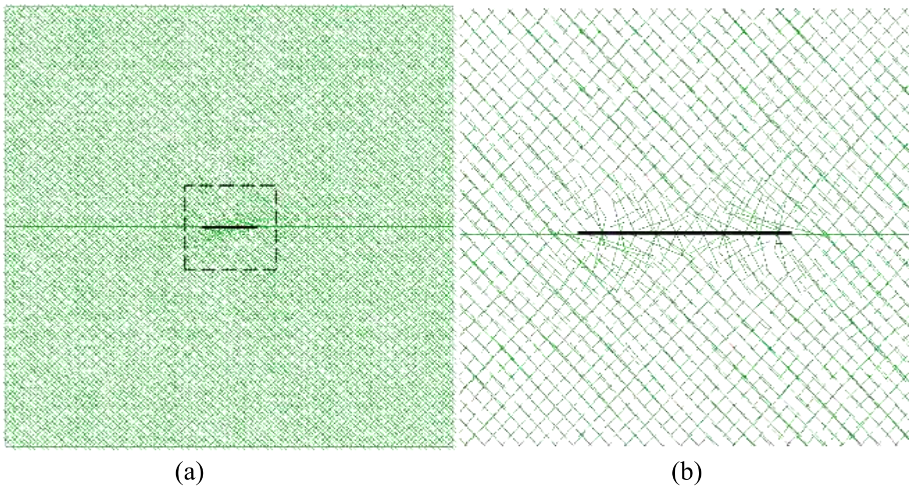

Figure 22. (a) Principal stress distribution in the generic model and (b) close-up of the stress distribution around to the fracture.

Conceptual models for thermo-mechanical analysis are conducted with different fracture sizes and orientations as shown in Figure 23 and Figure 24.The distance between the fracture and center of the heat sources is 5m to avoid intersection with the heat source block.

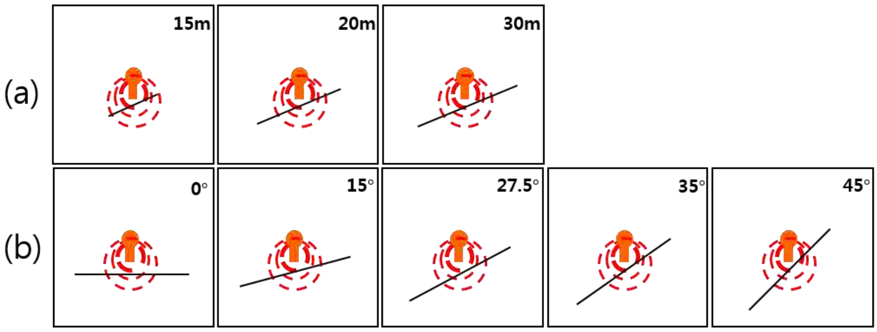

Figure 23. Illustration of the conceptual models of a single fracture the below the deposition hole modelled with UDEC for different (a) fracture lengths and (b) fracture orientations.

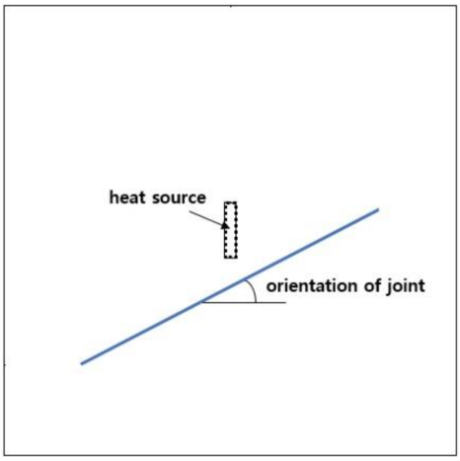

Figure 24. Geometry of conceptual model of a single fracture below a deposition hole with the heat source. Heat is generated at the center of model (0, -468m) and the center of the single fracture is at (0,-473m).

Figure 25 shows maximum shear and normal displacements of the single fracture for different fracture lengths. The friction angle of the fracture is assigned as 35.8°. As expected from Eq. (2.5), longer fractures show larger displacements for the same applied stress. The increase of fracture transmissivity is around one order of magnitude for the case of a 30 m long fracture. Figure 25c shows the increased transmissivity calculated using the change of mechanical aperture. An important observation from the modelling is that the increased transmissivity due to dilation does not return to its initial state after removing the load. As shown in Figure 25d, and unlike the SKB's estimation presented in Figure 13, the relative transmissivity remains after the heating cycle.

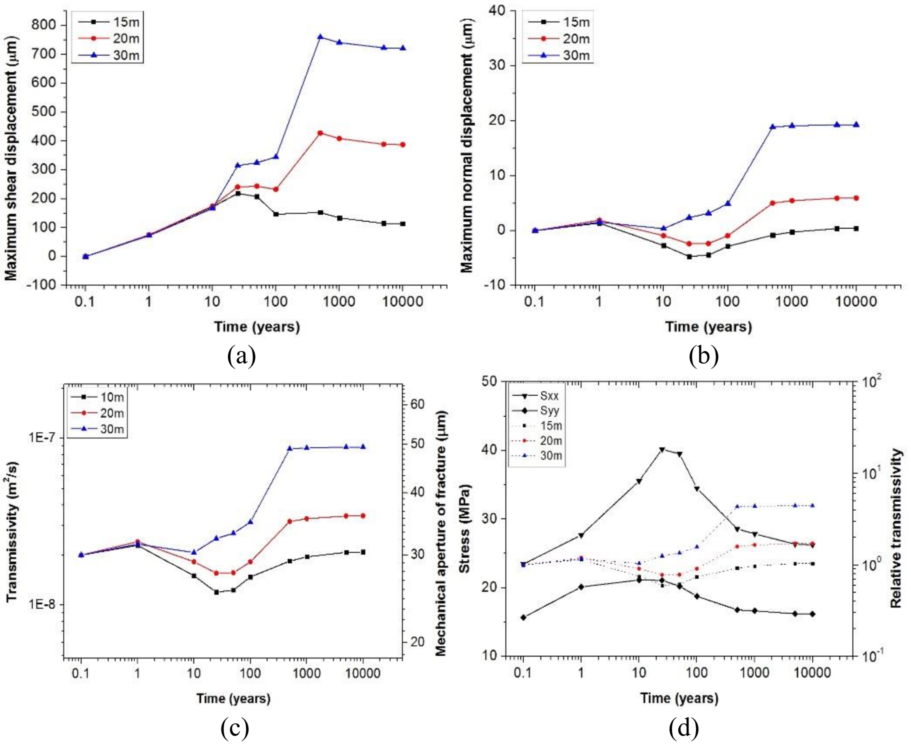

Figure 25. Fracture displacement and aperture evolution for various fracture lengths below a heat source during a time period of 10,000 years. (a) shear displacement, (b) normal displacement, (c) transmissivity and mechanical aperture, and (d) stress and relative transmissivity. The friction angle of the fracture is 35.8°.

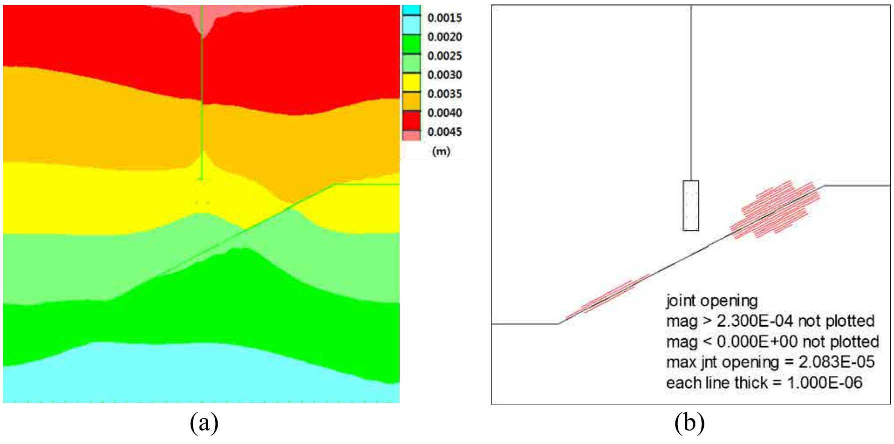

Figure 26. (a) magnitude of the displacement in the rock and (b) normal displacement of a fracture with length 30 m. Thermal stresses at centre of model make the fracture to displace and open (joint opening). The friction angle of the fracture is 35.8°.

Figure 26 represents the magnitude of the displacement in the rock and joint normal displacement fracture of 30 m length inclined 27.5° and at 500 years after start of the heating. That greater increase of the normal displacement at the right side of fracture is because of the vicinity to the heat source location.

The influence of fracture orientations on transmissivity was studied with fracture inclinations of 0°, 15°, 27.5°, 35°and 45°. Among the TM analyses, the one with the fracture dipping 45° shows the largest shear displacement for the assigned stress variation because it has the closest distance between fracture and heat source (Figure 27). In addition, the location of the maximum shear displacement is at the right side of the fracture because that side is closer to the heat source. The fracture with orientation 0° showed the least displacement among all the studied fracture orientations. All the different fracture orientations simulated except the 0° orintation show a remaining dilation and relative transmissivity following the cooling of the repository after 10,000 years.

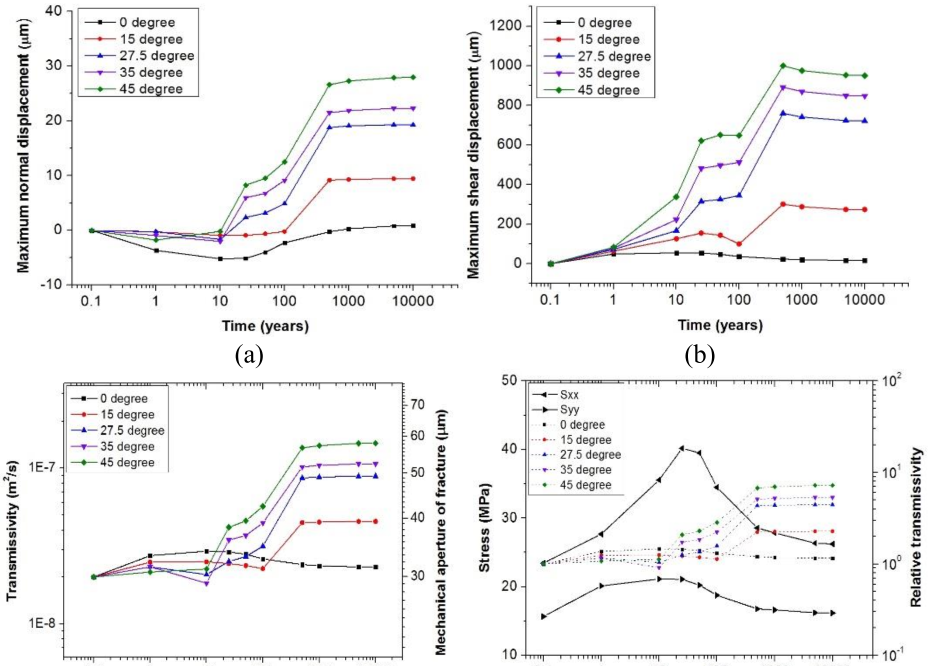

(a) (b)

(b) (d)

Figure 27. Fracture displacement, aperture and transmissivity evolution of a 30 m long fracture with different orientation located below a heat source during of a period of 10,000 years. (a) shear displacement, (b) normal displacement, (c) mechanical aperture and transmissivity and (d) relative transmissivity and stress.

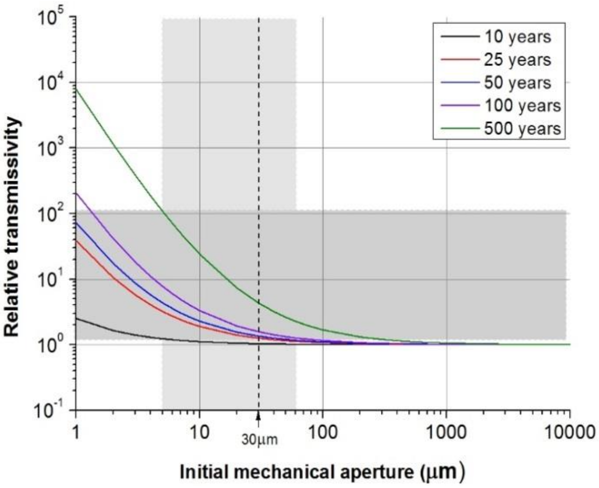

Figure 28. Possible ranges of relative transmissivity with respect to initial mechanical aperture. The gray area is the possible ranges of fracture transmissivity when initial mechanical aperture varies from 5 µm to 50 µm. The relative transmissivity changes by zero to two orders of magnitude for the specified aperture change. Investigation is made on a 30 m long fracture with 27.5° dip angle located below a heat source.

The shaded areas in Figure 28 show the possible range of relative transmissivity with respect to initial mechanical aperture. The modelling results show that relative transmissivity is greatly dependent on the initial mechanical aperture. The relative transmissivity increases by one order of magnitude for an initial aperture of 30 µm. For fractures with initial aperture of 5 µm, the relative transmissivity can increase by two orders of magnitude. The relative transmissivity change is a function of initial aperture since initial aperture is placed in the denominator in Eq. (2.3) for calculating the relative transmissivity. For initial apertures of around 100 µm and larger, the relative transmissivity change is less than one order of magnitude throughout the entire time period of 10,000 years.

3.2.4. Discrete Fracture Networks (DFN) for the independent TM modelling

Fracture data used for this study are based on rock domain FFM01 at Forsmark. Ten DFN realizations for each section were generated on behalf of SSM according to the fracture density and orientation data from Forsmark (Fox at al., 2007) as shown in Figure 29 to 24. The DFNs were initially constructed in 3D, and later cut into 2D sections at a depth of 468 m. 2D sections were extracted according to Figure 16. Full descriptions of DFN used for this study is provided in Appendix 2.

As it can be seen in Figure 29 to 24, the DFN realizations have generally poor connectivity. Only one realization (DFN02) out of ten DFN realizations ensures some level of connectivity for further investigation. Therefore, the Authors chose DFN02 which showed the greatest connectivity for further analysis. For the chosen DFN, three sections (NE, NW and HZ sections) are used for thermo-mechanical analysis. The DFN section NE02 (vertical section which the strike direction is N55E) is subjected to the minimum horizontal and vertical stress, and therefore minimize the possibility of fracture shear slip. On the other hand, DFN section NW02 is subject to maximum horizontal stress and vertical stress, which is likely to ensure higher possibility of fracture shear slip, although this will also depend on the selected DFN geometry. It is noted that it is not a straightforward matter to consider the 2D section along the deposition tunnel mainly due to the geometry of the excavation. As the effect of excavation is not the main theme of the study, we only considered the thermal loading from five heat sources along the same deposition tunnel.

The HZ section is where the maximum horizontal stress and minimum horizontal stress act. Actually, this section is the plane that cuts through the centers of canister at 468m depth. Similarly to the model with the NW02 section, the excavation was not considered to be the focus of the study due to geometrical reasons.

To consider the variability and uncertainty of the fracture density, the fracture density P_{32} was increased by 20% and DFN realizations were generated with this elevated P_{32} for NE section. The choice of 20% increase of $P_{32}$was somewhat arbitrary, but this value corresponds to around 60th percentile of the gamma distribution of fracture density for each fracture set. This is explained in greater detail in Appendix 2.

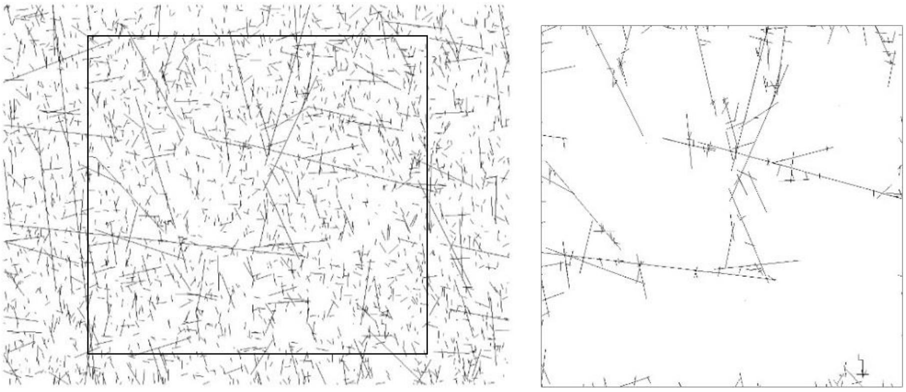
(a) (b)

Figure 29. Comparison of one original DFN and connected DFN for UDEC modelling for the NE section. (a) NE02 including all potential fractures (b) NE02 with only connected fractures for the UDEC model. In UDEC models, fractures not intersecting the boundary or other fractures are removed.

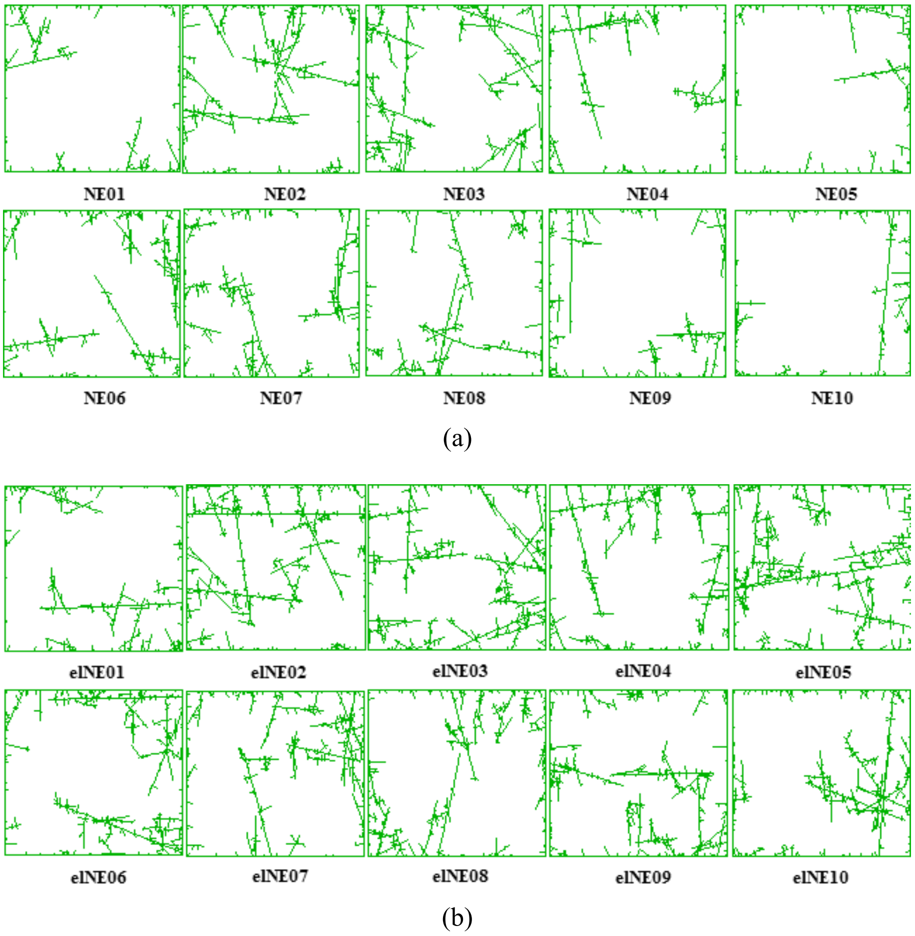

Figure 30. (a) ten NE sections generated from DFN realizations based on DFN data from Forsmark and (b) same sections from DFN realizations with elevated $\boldsymbol{P_{32}}$. In UDEC models, fractures not intersecting the boundary or other fractures are removed.

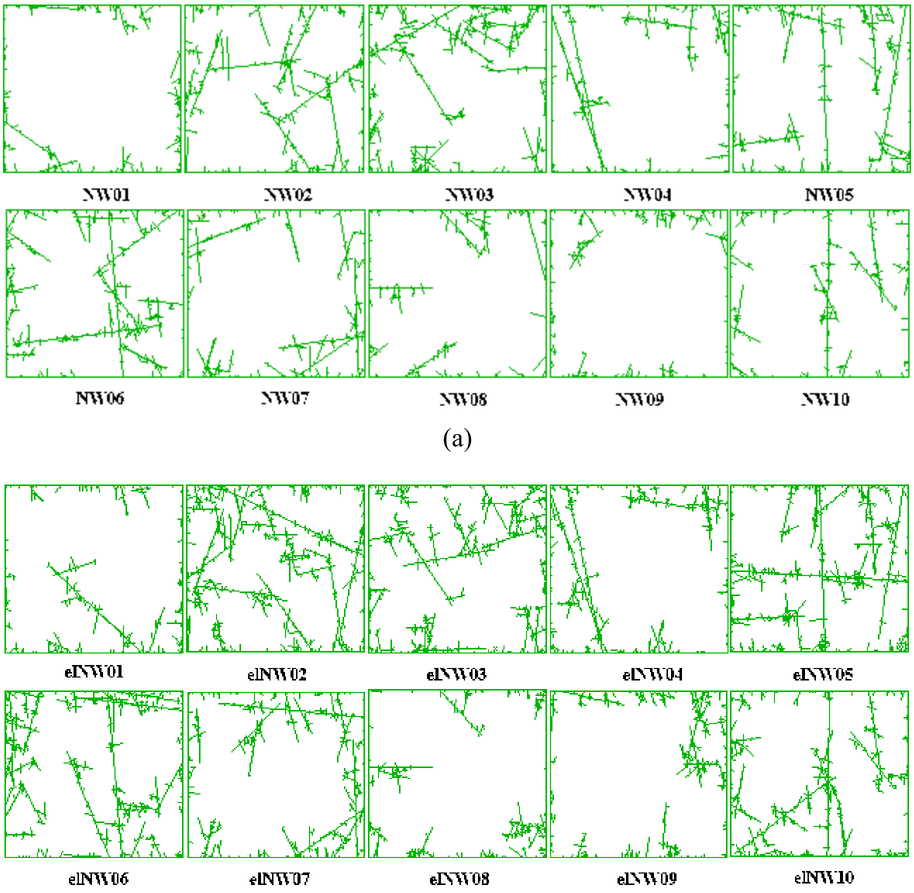

(a)

(b)

Figure 31. (a) ten NW sections generated from DFN realizations based on DFN data from Forsmark and (b) same sections from DFN realizations with elevated $\boldsymbol{P}_{32}$. In UDEC, fractures not intersecting the boundary or other fractures are removed.

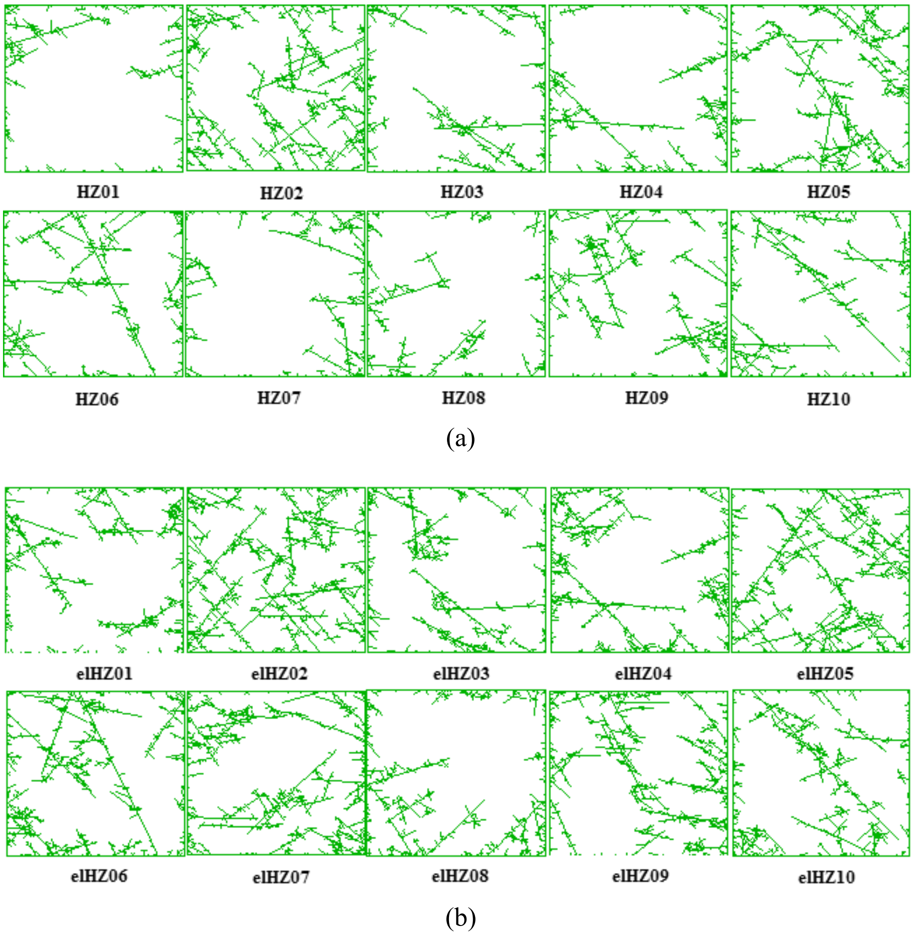

Figure 32. (a) ten HZ sections generated from DFN realizations based on DFN data from Forsmark and (b) same sections from DFN realizations with elevated $\boldsymbol{P_{32}}$. In UDEC, fractures not intersecting the boundary or other fractures are removed.

3.2.5. Independent TM modelling of the near-field with DFN for fracture transmissivity evolution during the thermal phase

Among the near-field DFN models, four (NE02, elNE02, NW02 and HZ02) are used for the UDEC TM analysis.

3.2.5.1. NE section

The NE02 model contains fracture plane traces on the N55E section. An additional model elNE02 has elevated value of P_{32} for the section. As shown in the right hand side of Figure 33, isolated fractures that do not isolate a block are not considered in the UDEC model.

TM analyses with NE section such as NE02 and elNE02 models give similar temperature evolution compared with the results of thermo-mechanical analysis without fractures as presented in section 3.2.2 .Temperature at the center of the model increases up to 55°C, 25 years after deposition of the canisters.

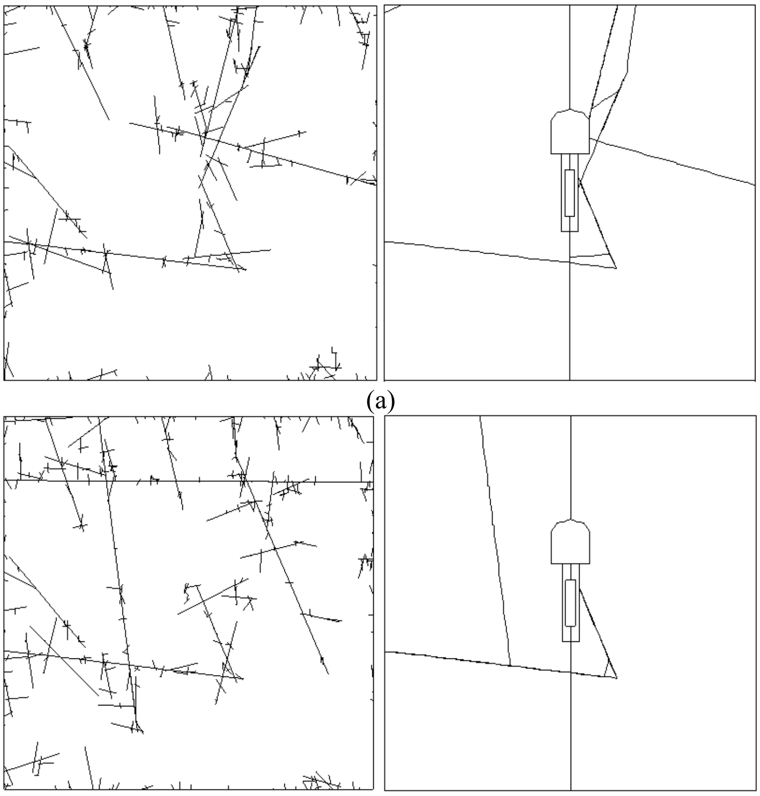

Figure 33. DFN models used for the near-field modelling of a tunnel and deposition hole. (a) DFN realization of model T_NE02, (b) the fractures and tunnel geometry considered in UDEC for model T_elNE02 with elevated P_{32}.

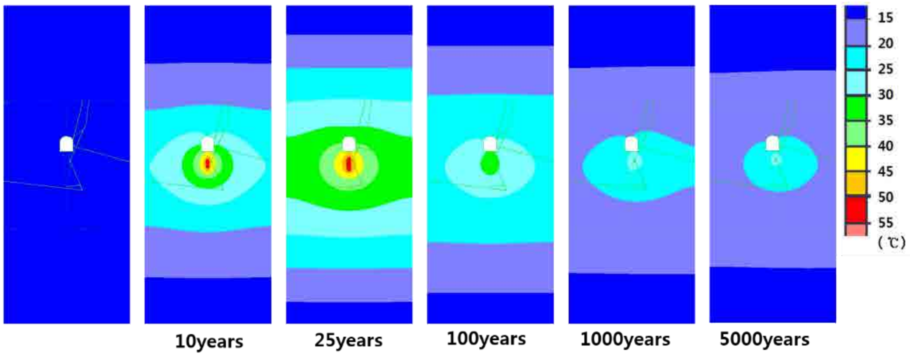

Figure 34. Temperature distribution in the T_NE02 model at different times from the start of canister deposition.

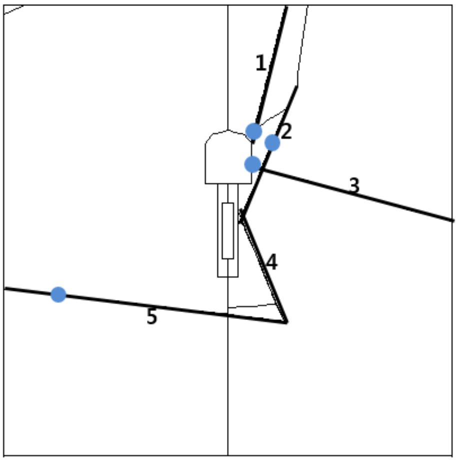

Figure 35. Illustration of fractures with large normal displacements in the T_NE02 model. The blue dots indicate the location of maximum normal displacement.

Figure 35 shows the DFN fractures of model NE02 and the locations of maximum normal displacement of each fracture for closer analysis. Among the presented fractures, fracture 1 and 2 are the key fractures. They show increased aperture when the thermal loading is applied. Figure A3-2 in Appendix 3 shows the evolutions of stress and displacement distribution in the entire models. The thermo-mechanical results are similar to the case of a model without fractures presented in Figure A3-1 in Appendix 3.

Figure 36 shows normal and shear displacement and stress of fracture 1 in model T_NE02. The displacement is maximum at the vicinity of the tunnel wall. It is important to note that the displacements are not reversible while the shear stress recovered to its initial state.

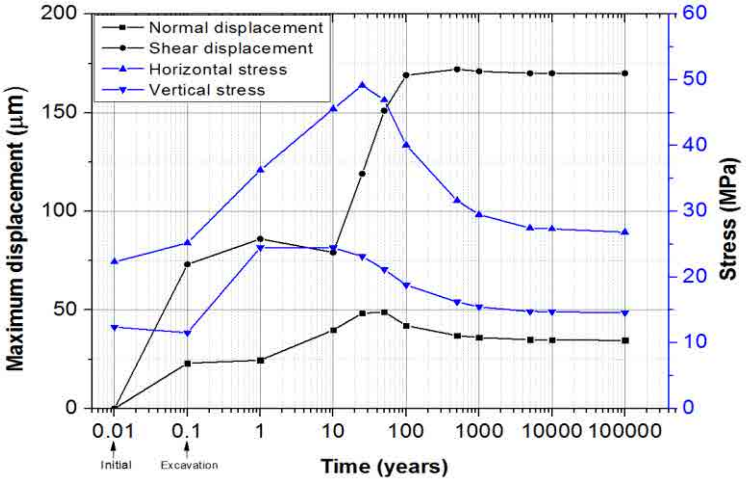

Figure 36. Evolutions of normal and shear displacement and normal and shear stress at fracture 1 for model T_ NE02 presented in Figure 35. Notice the remaining shear displacement after around 1,000 years.

Figure 37 shows the transmissivity evolution at two key fractures. Fracture 1 has the largest increase of transmissivity amounting to more than $3\times10^{-7}m^2/s$. The redistributed principal stresses are strongly dependent on the distance from the heat source. Close to the heat source location, much greater increase in stresses occurs. Also, the excavation of the tunnel can change stresses of fractures around the tunnel. The increase of transmissivity is about two orders of magnitude at the vicinity of the tunnel wall. Fracture 2 shows one order of magnitude increase in transmissivity at a point about 4 m away from the tunnel wall. This observation is contrary to the statement made by SKB which are that significant transmissivity change farther than 2 m from the tunnel wall is not likely. The Authors argue that a significant transmissivity increase is possible anywhere between the deposition tunnels because of the conspicuous stress ratio exceeding the critical stress ratio of the fracture, and the significant dilation under normal stress in the repository environment. Again this range of transmissivity increase is a function of the magnitude of the initial aperture. The relative transmissivity can increase up to three orders of magnitude for an initial aperture of 5 µm as shown in Figure 38. As explained before, the relative transmissivity is a function of the initial aperture and relative transmissivity is one to three orders of magnitude with initial aperture between 50 µm and 5 µm.

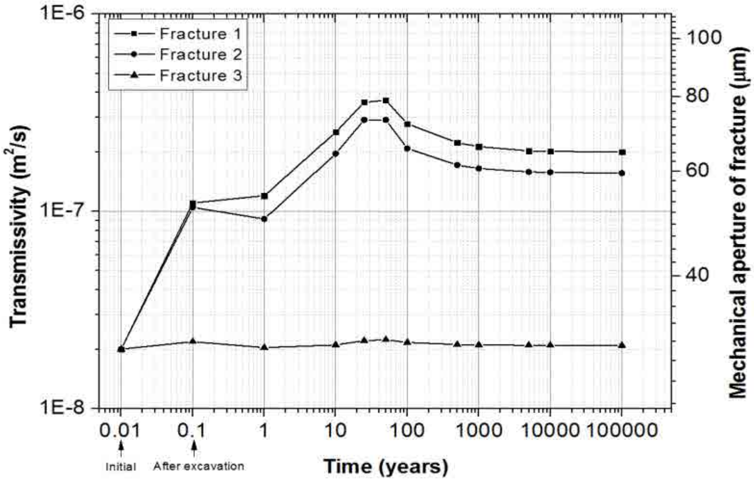

Figure 37. Evolution of the mechanical aperture and transmissivity for model T_NE02 with initial mechanical aperture of 30 µm.

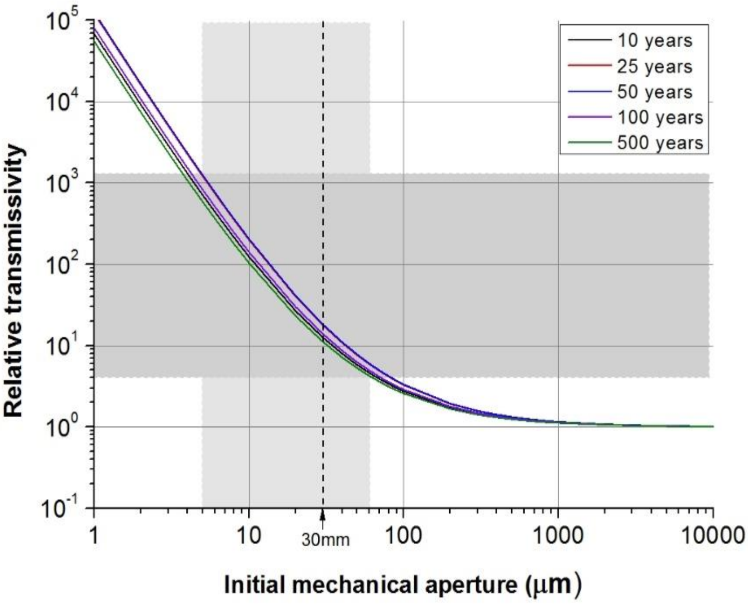

Figure 38. Initial mechanical aperture versus relative transmissivity obtained from thermo-mechanical analysis. Results are from fracture 1 in model T_NE02 (Figure 35). It is noted that the relative transmissivity is a function of the initial aperture of the fracture.

Similar observations about deformation, transmissivity and stress distribution are obtained for the elNE02 models. Figure 40 shows the shear and normal displacement and stress of fracture 1 in model T_elNE02. The maximum shear displacement is 158 µm at the tunnel boundary. Compared to the results from the NE02 model, the orientation of the fracture is less sensitive to slip and, therefore, the magnitude of shear displacements is smaller than for the NE02 model.

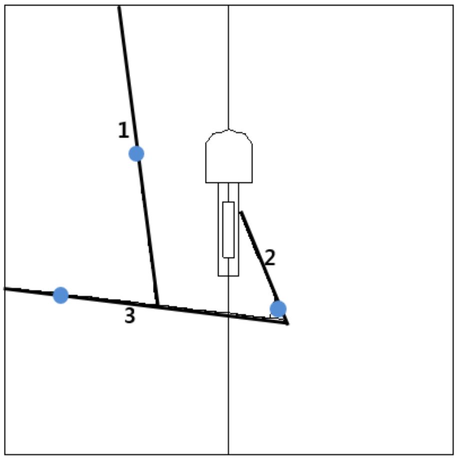

Figure 39. Illustration of fractures with large normal displacements in the T_elNE02 model. The blue dots indicate the location of maximum normal displacements. Fracture 1 has the greatest normal displacement of about 6 μm among the three fractures.

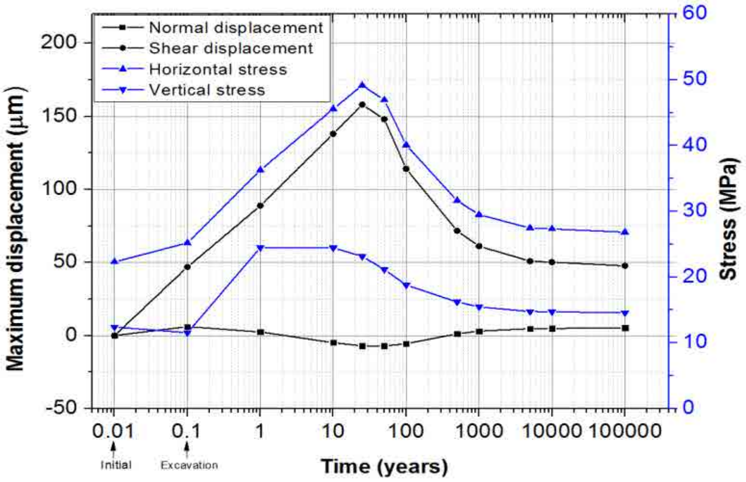

Figure 40. Evolutions of normal and shear displacement and normal and shear stress at fracture 1 in the T_elNE02 model as shown in Figure 39.

By comparing the result for the NE02 model and the elNE02 model, the shear displacement at the tunnel wall, which can be interpreted as EDZ (Excavation Damage Zone), is greatest among all the. In both cases, sheared fractures maintain the displacements even after the thermal load diminishes. Furthermore, the development of shear and normal displacement seem to be a function of various factors such as fracture density, orientation and length. Therefore, it is important to obtain precise fracture data when analyzing the possible thermo-shearing.

Key fractures and the points of largest normal displacement are indicated in Figure 39. Figure A3-3 in Appendix 3 shows the evolutions of stress and displacement distribution for the models with elevated P_{32}. These results are similar to those for the NE02 model as shown in Figure A3-2 in Appendix 3.

The transmissivity evolutions are shown in Figure 41 and Figure 42. The largest transmissivity increase, less than 1 order of magnitude, occurred at fracture 1 which is located about 8 m away from the tunnel wall. Moreover, the reduction of transmissivity change can occur when the initial aperture is 5 μm.

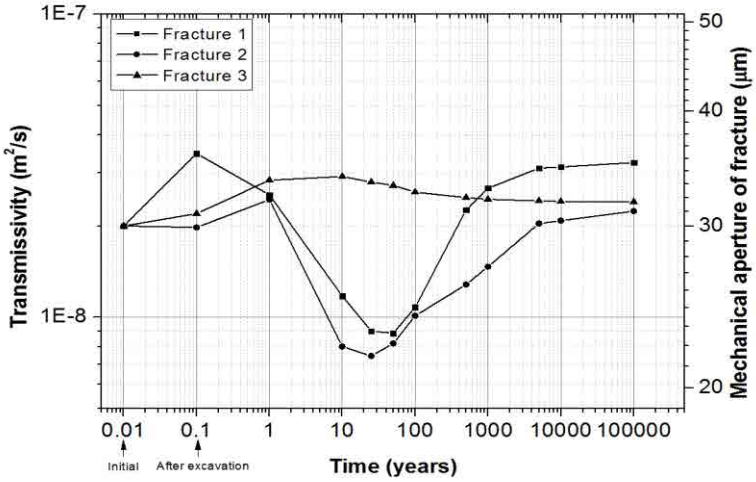

Figure 41. Mechanical aperture and transmissivity evolution if an initial mechanical aperture of 30 μm is assumed for the T_elNE02 model.

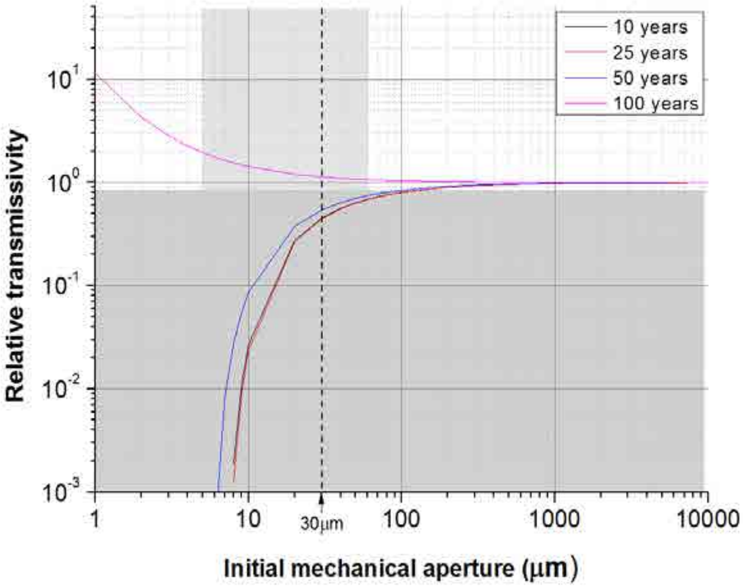

Figure 42. Initial mechanical aperture versus relative transmissivity from the thermo-mechanical analysis. The results are from fracture 1 in model T_elNE02 as shown in Figure 39. The maximum normal displacement occurs after 50 years as shown in Figure 40. When the initial mechanical aperture ranges from 5 μm to 50 μm, the relative transmissivity increase is less than one order of magnitude and there is a reduction of transmissivity in earlier times.

3.2.5.2. NW section

Modelling transmissivity in the near-field was carried out with the NW section, which was cut across North-East direction in the 3D DFN model as shown in Figure 16 and Figure 17. The NW section is subjected to maximum horizontal and vertical stresses. Figure A3-4 in Appendix 3 presents the evolution of stresses and displacements in the entire models. The results of analysis on NW section show largely similar trend in terms of stress and displacement as for the NE section.

The fracture network NW02 was chosen for the NW section analysis. The fractures that don't intersect the model block or excavation boundary are removed as shown in Figure 43.The NW section crosses many deposition holes, and therefore the mechanical excavation of deposition tunnels and holes was not explicitly modeled for verisimilitude of the two dimensional sections. The analyses are entirely with focus on the thermal loading of fractures due to heat decay.

For the NW section model, the power of heat source at the canister is adjusted considering the tunnel spacing and canister geometry. Because the two-dimensional UDEC code assumes the heat source extends out of the model plane, the power needs to be divided by the distance between each deposition tunnel. As a result, the temperature at the center of canister (Figure 44) becomes similar to the temperature evolution in the models of NE section.

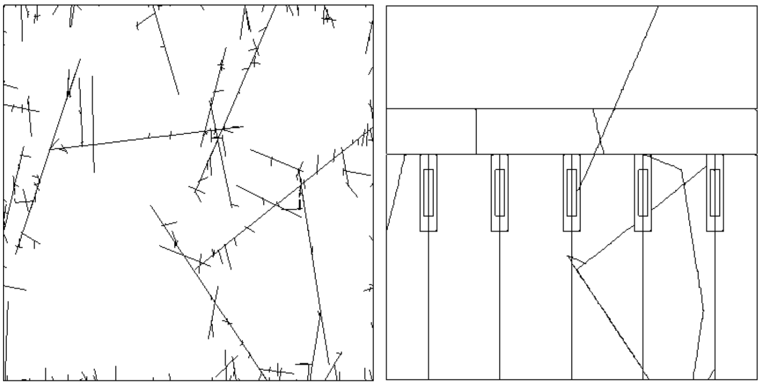

Figure 43. Fracture network NW02 is used for the NW section analysis in this study (left). Fractures which are intersecting with deposition tunnel and hole geometry are shown in the right figure.

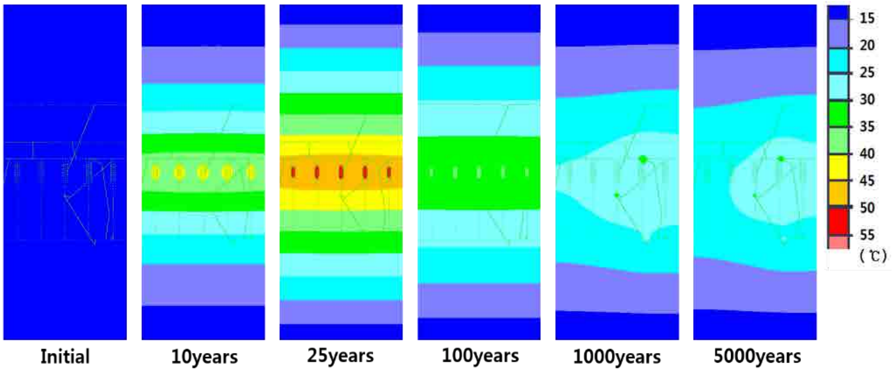

Figure 44. Temperature distribution in the T_NW02 model with time from the canister deposition.

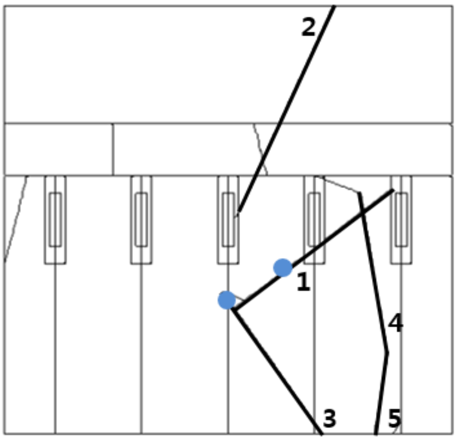

Figure 45. Illustration of the fractures with large normal displacements in the T_NW02 model.

Figure 45 shows the key fractures in the NW section analysis. Fracture 1 has the largest normal and shear displacement throughout the thermal loading time. The maximum normal displacement is 75 µm, 25 years after thermal loading has started. The increase of transmissivity is around one orders of magnitude as shown in Figure 47. The magnitude of the change in transmissivity and displacement are greater than for the NE section and the irreversibility of fracture displacement is similar. The fracture relative transmissivity is a function of the magnitude of the initial aperture and this is shown in Figure 48. If the initial aperture is 5 µm, the transmissivity becomes more than 3 orders of magnitude.

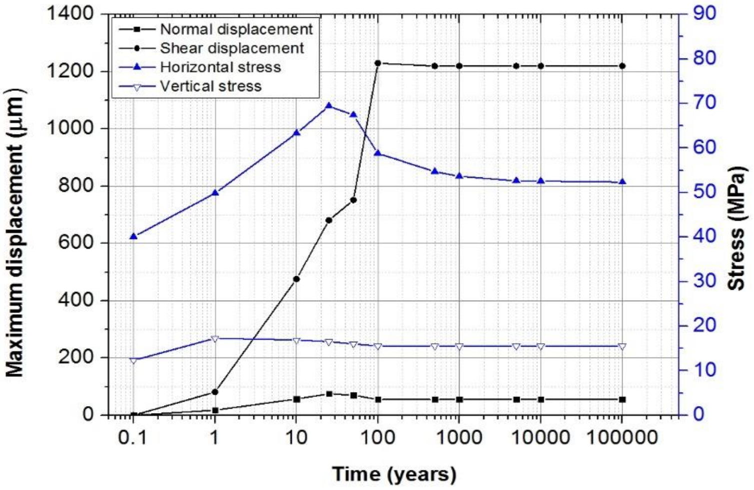

Figure 46. Evolution of normal and shear displacement, and normal and shear stress at fracture 1 in the model T_NW02 presented in Figure 45. Notice the remaining shear displacement after around 100 years.

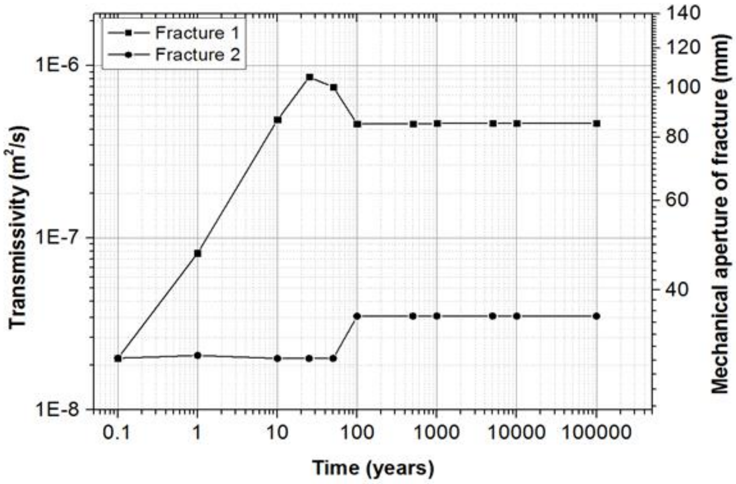

Figure 47. Evolution of the mechanical aperture and transmissivity for model the T_NW02 with initial mechanical aperture of 30 μm.

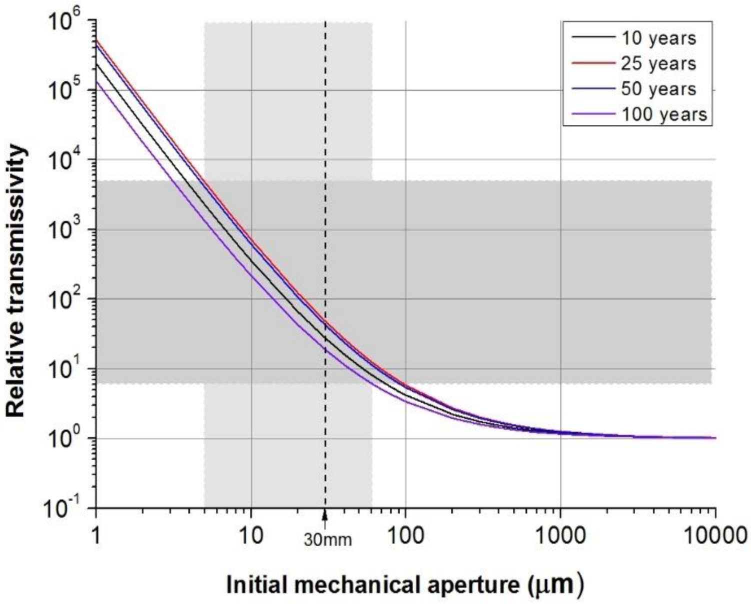

Figure 48. Initial mechanical aperture versus relative transmissivity using TM results for fracture 1 in model T_NW02 in Figure 45.

3.2.5.3. HZ section

The horizontal section cases HZ were executed with different stress regimes and geometry. The DFN realization HZ02 was cut horizontally through at 468 m depth. Therefore, the stress regime consists of the maximum horizontal and minimum horizontal stress. The canisters and deposition holes are represented with circles as they are cut through at the mid-canister height as shown in Figure 49. The power of heat source applied to these five circles is adjusted by dividing the original heat source with the length from the top to the bottom of the canister. This is because UDEC assumes that the 2-dimensional model has one meter out-of-plane dimension in the z-direction. Figure A3-5 in Appendix 3 presents the evolution of the stresses and displacements in the models. The results of the HZ section modelling shows similar trends as those for the NE and NW sections in terms of development of stresses and displacements. The temperature evolution is shown in Figure 50, and its maximum temperature is around 55°C.

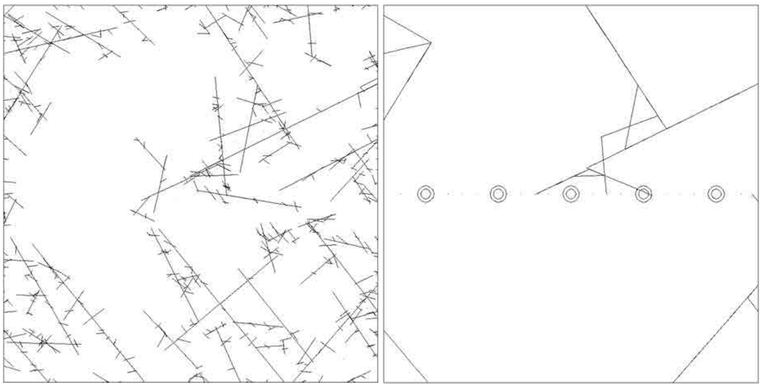

Figure 49. The fracture network T_HZ02 used for the HZ section analysis (left). Fractures intersecting five deposition holes are shown (right).

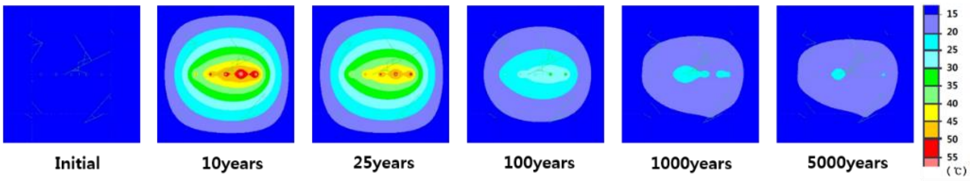

Initial 10years 25years 100years 1000years 5000years

Figure 50. Temperature distribution around the deposition holes for the model T_HZ02 with time.

Figure 51 presents three key fractures that show the greatest shear displacement during thermal loading. Figure 52 shows the stress and displacement in both normal and shear directions. The transmissivity and aperture evolutions for fracture 1 and 2 are presented in Figure 53. In general, normal and shear displacement are very small compared with NE and NW section results. Figure 54 shows the relative transmissivity change with respect to various initial apertures. The maximum normal displacement is 2.7 μm on fracture 1 at 100,000 years. Relative transmissivity is increased by up to a factor of three even when initial aperture is as small as 5 μm. Therefore, thermal loading in the HZ section has very little effect on transmissivity change. This can be explained by means of the lower ratio of maximum horizontal stress to minimum horizontal stress compared to the case with the NE or NW sections.

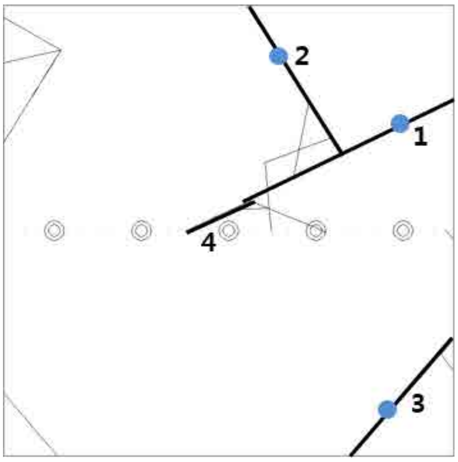

Figure 51. Illustration of fractures with large normal displacements in the T_HZ02 model. Fracture 1 has the largest normal displacement of 2.739 µm among three fractures marked with a blue dot.

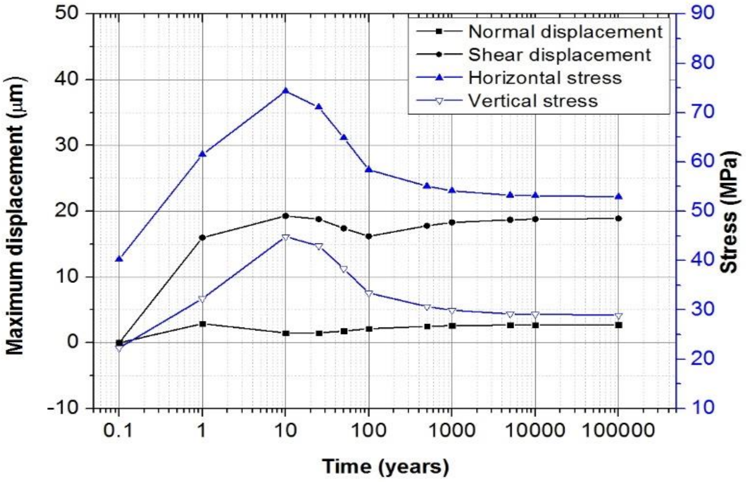

Figure 52. Evolution of normal and shear displacement and normal and shear stress for fracture 1 of model T_HZ02 as presented in Figure 51. Notice the remaining shear and normal displacement after around 1,000 years of deposition.

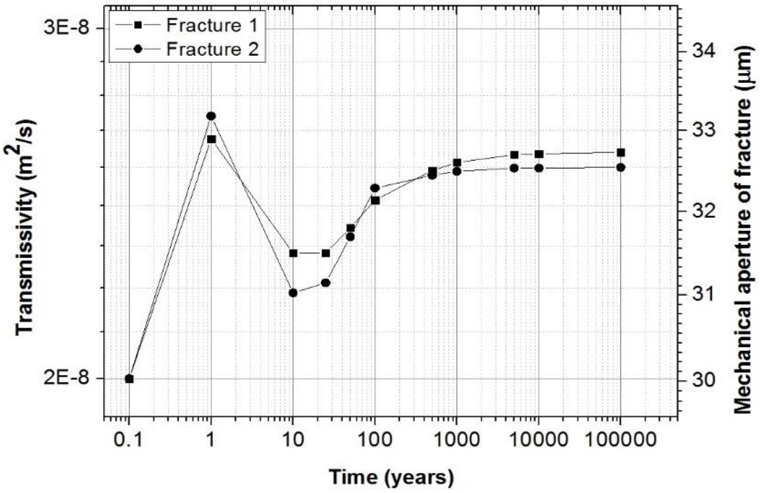

Figure 53. Evolution of the mechanical aperture and transmissivity for fracture 1 and 2 in model T_HZ02 with initial mechanical aperture of 30 µm.

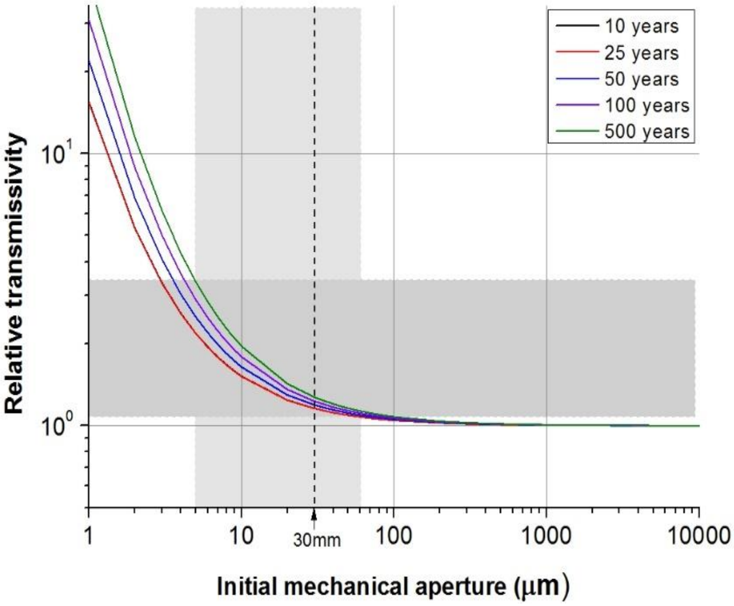

Figure 54. Initial mechanical aperture versus relative transmissivity using TM results of fracture 1 in model T_HZ02 presented in Figure 51. The relative transmissivity is a function of initial aperture of fracture.

3.2.6. Irreversibility of shear dilation in the independent TM modelling

Due to the elasto-plastic behavior of the rock fractures, most of the induced shear displacements occur after shear failure and cannot be recovered just by removing of the effect of thermal stress with cooling of the repository. The conceptual model and the independent TM modelling of DFN models consistently show that the fracture dilation, shear displacement and transmissivity undergo irreversible shear deformation and do not return to their original state when the applied stresses returns to its original state (see e.g., Figure 27, Figure 36, Figure 40, Figure 46 and Figure 52). Similar observations were also presented in Min et al. (2013). The Authors argue again here that the irreversible nature of transmissivity change is important because any significant shear-induced transmissivity change is permanent. Furthermore, the total transmissivity can even further increase because of normal openings when the normal thermal stress reduces.

In addition to the irreversibility, important parameters for the evaluation of the range of transmissivity change are dilation angle, friction angle and critical shear displacement. The critical shear displacement is defined as the shear displacement beyond which dilation no longer occurs. The dilation angle chosen for the analyses was 3.2° based on laboratory experiment at normal stress of 20 MPa. The critical shear displacement was chosen as 3 mm above which no more dilation occurs. This value is considered to be conservative given that the transmissivity increased for shear displacements up to 10 mm during tests on fractures of Ävrö granite (Olsson, 1998). SKB's dilation angles were determined from shear displacement of up to 2.1 mm for normal stress of 20 MPa. The choice of normal and shear stiffness has less influence because the high normal stiffness of 656 GPa/m determined in Forsmark does not allow for much normal deformation at the applied in situ and thermal stresses. In conclusion, given all uncertainties associated with the choice of fracture parameters, the magnitude of the transmissivity change may become larger when larger dilation angles are used.

3.2.7. Independent analysis of the far-field for fracture shear slip evolution during the thermal phase

Deformation zones are analyzed to investigate the possibility of shear slip due to thermal loading from the repository that can affect transmissivity. For this analysis, the Authors imposed the thermal stress history data from the three-dimensional thermo-mechanical analysis (Min et al., 2013) onto the far-field model. Then, the possibility of thermo-shearing was investigated (Figure 55).

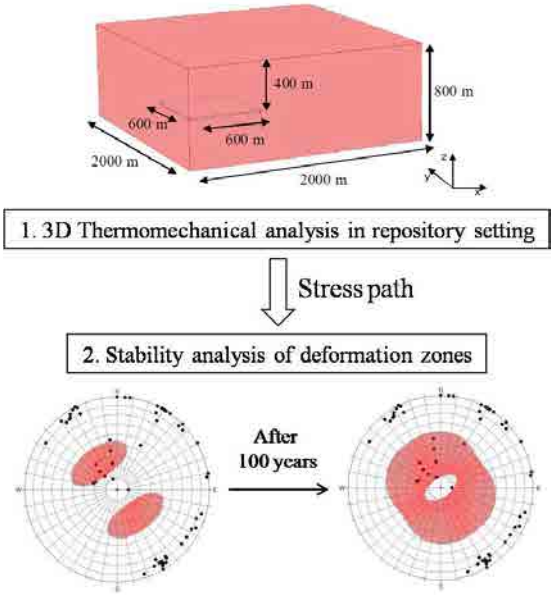

Figure 55. A schematic view of the far field shear slip analysis during the thermal phase of the repository.

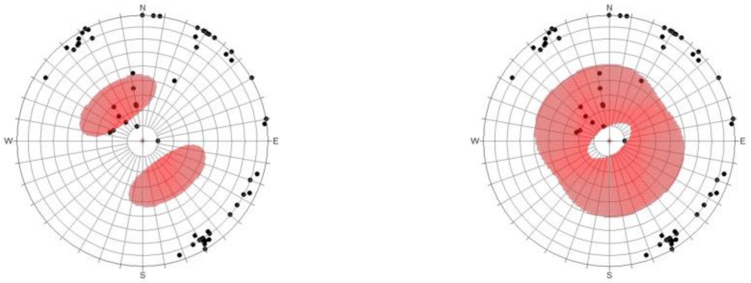

Initial After 100 years

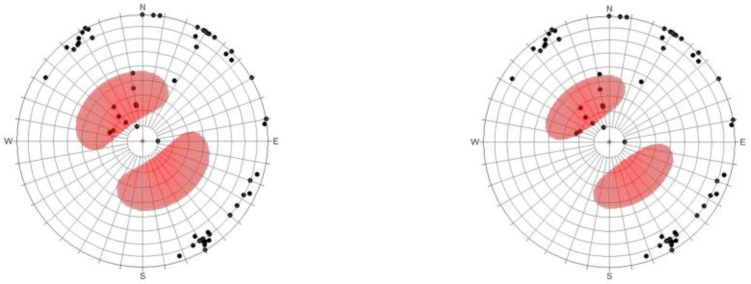

After 1,000 years After 10,000 years

Figure 56. The range of shear slip (red areas) for the deformation zones (poles) at the Forsmark site. Thermal stress data are obtained at the center of the repository at a depth of about 400 m.

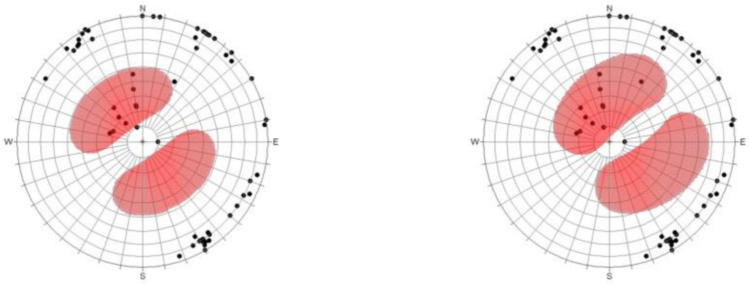

Initial After 100 years

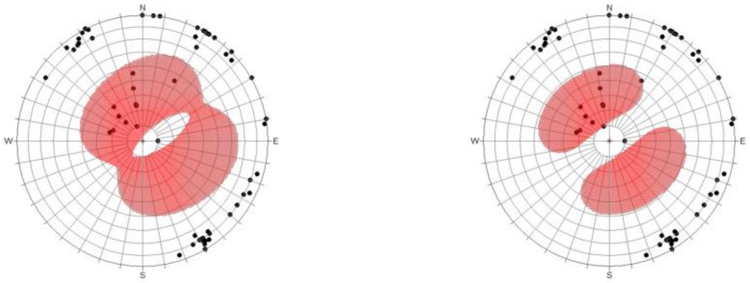

After 1,000 years After 10,000 years

Figure 57. The range of shear slip (red areas) for the deformation zones (poles) at the Forsmark site. The thermal stress data are from a location 200 m away from the periphery of the repository at a depth of 200 m.

Given the orientation of a fracture and the stress field, normal and shear stress acting on the fracture plane can be calculated from Cauchy's formula (Lee et al., 2013). In order to evaluate the stability of the deformation zones, we used the Mohr-Coulomb failure criterion assuming zero cohesion. The data set for the deformation zones was taken from Table 5-2 in Stephens et al. (2007). The friction coefficient used for this study was 0.6, which is the lower bound of typical values for large faults (Byerlee, 1978).

In order to investigate the stability of the deformation zones during the thermal phase, we plotted the actual orientation of deformation zone together with the possible range of orientations that could allow for shear slip (pole plots on the lower hemisphere in Figure 56 and Figure 57). The red-shaded area is the distribution of fracture poles for which shear slip can occur. The evolution of the size of the shaded shear slip area shows that the size reaches a maximum at 1,000 years, and the temperature then returns almost to its initial state after 10,000 years.

As shown in Figure 56 and Figure 57, the number of deformation zones that are overlapping the shear slip area is less than 10 and the area with fractures most prone to shearing and dilation is for predominantly in sub-horizontal features. At Forsmark, most of the deformation zones are sub-vertical and the majority of the zones are less vulnerable to shear slip compared with a random orientation of the deformation zones, even with a substantially increased thermal stress larger than 20 MPa.

A notable difference occurs at the point 600 m horizontally away and vertically 200 m above the center of repository. This shows a slight tilting of the shaded slip zone at 100 and 1,000 years, which can be explained by the thermally-induced rotation of principal stress at mid-depth around the repository (Figure 57).

In the far-field model, only the possibility of shear slip was evaluated without actual calculation of transmissivity change. In order to gain a more quantitative estimation of transmissivity change, the mechanical properties of large scale deformation zones need to be determined, which are presumably different from single short fractures.

3.3. The Consultants’ assessment on the evolution of fracture transmissivity during the thermal phase based on independent TM modelling

The authors’ findings from the review of rock fracture transmissivity and from the results of the independent modelling can be summarized as follows:

- The magnitude of transmissivity change induced by shearing was considered negligible in SKB’s license application. In fact, SKB did not conduct quantitative estimation of transmissivity change due to shear dilation. The current review shows that transmissivity increase from shearing can be up to 2 orders of magnitude for fractures with an initial aperture of 30 µm. Transmissivity increase can reach 3 and 4 orders of magnitude with initial aperture of 10 µm and 5 µm, respectively.
- SKB claims that the region that is vulnerable to transmissivity change is within 2 m from the tunnel periphery. However, the current review and modelling show that large transmissivity change (up to 2 orders of magnitude) can occur around 4m from the deposition tunnel and hole for a KBS-3V disposal concept. We argue that a significant transmissivity increase is possible anywhere between adjacent deposition tunnels and deposition holes because of the significant stress ratio exceeding the critical stress ratio for initiation of shear-slip, and significant dilation behavior under reduced normal stress in the repository environment.
- The modelling results show that the increased transmissivity induced by shear dilation did not recover to its initial state after cooling of the repository and, therefore, the process of thermo-shearing is irreversible. SKB’s modelling showed the recovery of transmissivity after 10,000 years and SKB’s investigation failed to capture this important phenomenon of transmissivity irreversibility. It is emphasized that a permanent change of transmissivity can impact the buffer resaturation time, radionuclide transport and buffer erosion which are critical factors for long-term safety of repository.
- The connectivity of the bedrock in Forsmark area is very poor and only one out of ten DFN realizations of the rock mass showed sufficiently high connectivity around the deposition hole. It is noted that only a small fraction of the fractures are responsible for the overall fluid flow in the rock mass and a low connectivity model still resulted in considerable increase of transmissivity in fractures due to thermoshearing.
- In the study of far-field modelling, sub-horizontal deformation zones were found to be most prone to shear dilation induced by thermal loading. Only the shear slip was investigated in this study without determination of possible range of transmissivity. Improving the far-field modelling of shear-slip and transmissivity change will require substantial data about mechanical and hydraulic properties of deformation zones.

The findings listed above are applicable to the thermal phase of the repository lifetime and the following aspects have to be considered in evaluating the significance of the current review and modelling, and for further studies.

- The current study was conducted based on two-dimensional DFN cuts from three-dimensional DFN from Forsmark. This process of cutting greatly reduces the connectivity of fractures in the rock mass. It is also noted that 2-D DFN can overestimate the shear displacement compared to 3-D DFN because 2-D DFN implies infinitely long planar fractures in the direction perpendicular to the model plane Therefore, the transmissivity change presented in this study would become more realistic if a hydro-mechanical analysis on 3-D DFN realizations was conducted. More quantitative study about the significance of 2-D simplification is recommended.
- Characterizing the hydraulic and mechanical behavior of rock fractures and deformation zones is a longstanding difficulty in rock mechanics and hydrogeology. For example, it is not straight-forward to distinguish between mechanical and hydraulic apertures. There is no consensus in the scientific community with respect to how to scale measured dilation behavior in centimeter scale in the laboratory and to upscale to hundreds of meter in the field. Given all these reservations and problems, one has to take a conservative approach when evaluating the possible range of magnitude and spatial extent of transmissivity change for a repository site.

4. Modelling of the evolution of fracture transmissivity during the glacial phase of the repository

4.1. SKB's presentation

SKB has estimated the transmissivity change due to normal and shear stress during glacial phase of the repository as shown in Figure 58 (Hökmark et al., 2010). Temporal evolution of the glacially induced stresses in Forsmark are used at all depths from the surface to 1,000 m depth and added to the in situ stresses. Two different pressure models were used for pore pressure estimation as shown in Figure 59. The first pore pressure model used excess pore pressure as 98% of glacially induced vertical load at all times and at all depths. The second pressure model considered additional residual and permafrost-induced excess pore pressures.

No coupled THM or HM analyses were performed by SKB to simulate the glacial phase of the repository. Further, no rock fractures were simulated explicitly in SKB's modelling approach. Instead, stress-induced transmissivity changes were estimated for hypothetical fracture planes.

Hökmark et al. (2006) also estimated the transmissivity change during the glacial phase, in which an increase by a factor of 7 was observed just below the frozen ground due to elevated pore pressure, and hence, with decreased effective normal stress. At the repository depth, an increase of transmissivity by a factor of 3 was found.

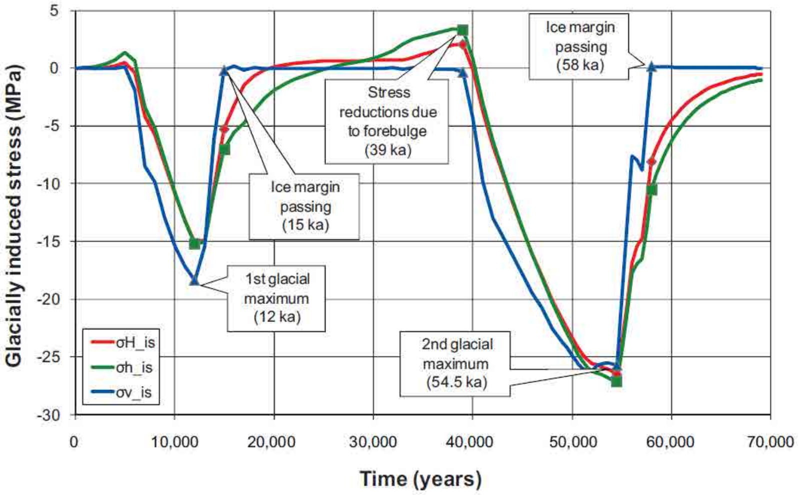

Figure 58. Glacially induced stress increments to be superimposed to in situ stresses. The orientation of the stress increments are assumed to be the same as for the present-day in situ stresses (Hökmark et al., 2010).

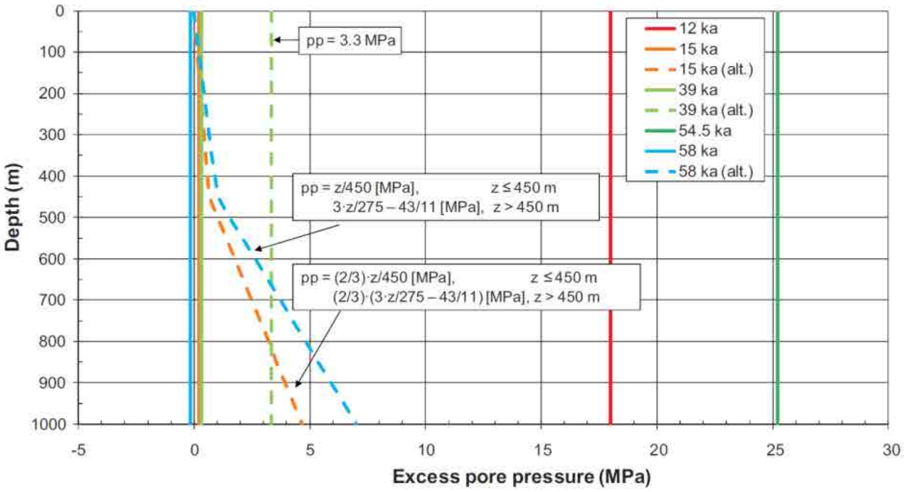

Figure 59. Glacially induced pore pressure model for Forsmark (Hökmark et al., 2010). The solid lines represent the excess pore pressure induced by glacial load. This case does not consider remaining pore pressure. Comparing to this, the dotted lines reflect the remaining pore pressure after glacial load removal.

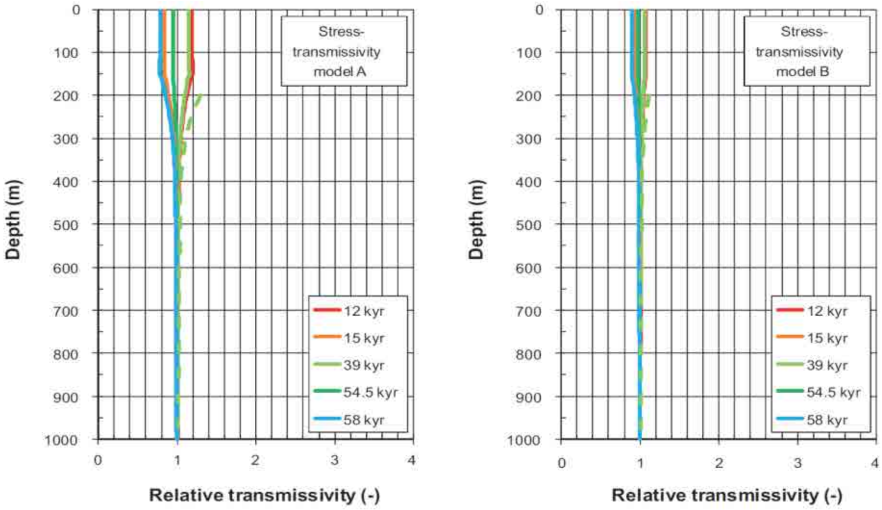

Figure 60. Relative transmissivity of vertical fractures striking perpendicularly to the present-day maximum horizontal stress. Dashed lines indicate that the relative transmissivity is affected by residual pore pressures (Hökmark et al., 2010).

4.1.1. Transmissivity change due to normal stress

Two stress-transmissivity models (Model A and B) were selected by SKB to estimate changes in relative transmissivity due to normal stress variations. Model A can be considered a “worst case” option based on lower bound fracture normal stiffness, and Model B uses average fracture normal stiffness and it is therefore less sensitive to normal stress. The relative transmissivity of fractures is evaluated at two depths: 250 m and 460 m. The largest increase in relative transmissivity at 460 m was found to be a factor of 2 to 2.5 that can be slightly increased to 2.5 to 3 when thermo-mechanical effects due to permafrost are included. The increases of relative transmissivity at shallower depth of 250 m were generally larger.

4.1.2. Transmissivity change due to shear stress

SKB’s estimates of the maximum shear displacement are made for fractures striking perpendicularly to the major horizontal in situ stress and dipping 27.1°, which is estimated from the Mohr-Coulomb failure criterion and the virgin state of stress. Furthermore, effective normal stress and corresponding shear displacement of fractures of all orientations are presented by using lower hemisphere stereonet. Figure 61 presents the estimate of the maximum slip at the center of a fracture dipping 27.1° in the plane of NE section. For a fracture with radius 100 m, the induced maximum slip at all depths is about 5 to 5.5 mm during the first ice retreat, and 8 mm during the second retreat. At all other depths, the total slip magnitude is lower than the slip due to the in situ stress as shown in Figure 61. SKB’s modeling in medium scale also showed that there are notable shear displacements between 2 to 7 mm after glacial loading, which apparently indicate the irreversible nature of shear displacement (Hökmark et al., 2010). The important omission in SKB’s work is the significant underestimation and lack of discussion about the transmissivity change due to dilation of the fractures resulting from their shear slip. A shear displacement of 5 mm might correspond to a normal dilation of 300 µm and 1000 µm, for dilation angles of 3.2°and 10°, respectively, as shown in Figure 7. Therefore, transmissivity change induced by shear displacement at moderate normal stress cannot be ignored.

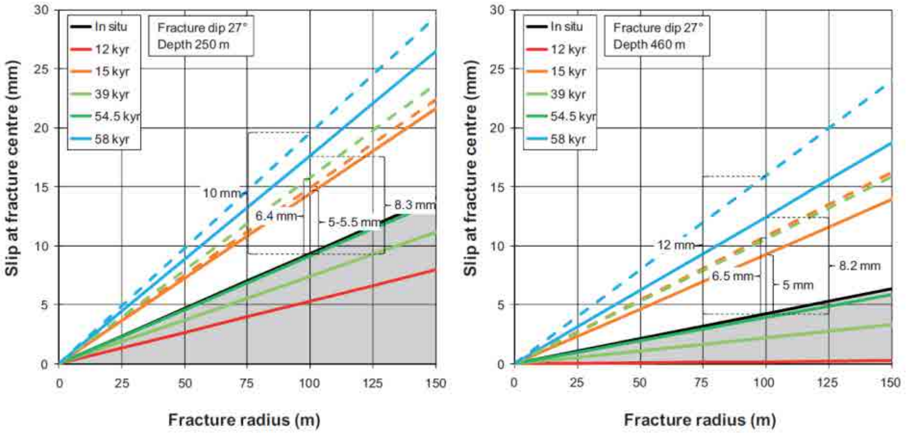

Figure 61. Shear slip magnitude estimates at 250 m (left) and 460 m (right) depth assuming the excess pore pressure to be 98% of the glacially induced vertical load (solid lines) or residual and permafrost induced excess pore pressures (dashed lines), respectively. Curves drawn in the gray shaded area represent points in time when the conditions are more stable than for in situ initial conditions (Hökmark et al., 2010).

4.2. Motivation of the assessment on the evolution of transmissivity during the glacial phase based on independent modelling

Glacially induced stress will be superimposed to the in situ state of stress in the repository (Rosengren and Stephansson, 1993). Confinement in the horizontal direction and added vertical stress from the ice load will increase the horizontal stress. In the current analysis, induced stress from glaciation are added as boundary condition to the existing thermo-mechanical discontinuum model with decaying heat generation. The analysis lasts for 100,000 years, which includes loading from a glacial cycle with two ice peaks as shown in Figure 58. The effect of the pore pressure is considered in the current study. The pore pressure change with depth has the same gradient as the change in vertical rock stress. Therefore, the cycle of pore pressure changes follow the cycle of glacially induced vertical stress. In summary, glacial loading that includes in situ rock stress, thermal loading, glacially induced stresses and pore pressure are modelled by means of thermo-mechanical analysis.

4.2.1. Data and geometry for the glacial loading phase

The repository geometry and heat source data are identical as for the modelling of the thermal loading scenario. In this glacial loading model, DFN fracture network NE02 and NW02 models are used, and boundary stresses induced by glacial load are superimposed on in situ and thermal stresses as shown in Figure 62.

Glacial loading is added to the vertical virgin state of stress as a boundary stress 5,000 years after deposition of canisters. Also, the boundary stresses increase each 1,000 year time-step, and they decrease to initial stress state after 80,000 years. The basic assumption of UDEC modelling is that the block is impermeable, and the fluid flow only occurs through the joints of the model. Therefore, pore pressure is applied to joints in two of the DFN models meaning that the effective stress in the joints will decrease. This procedure can make the joints to slip easily which is best illustrated by moving the Mohr's circle closer to the failure envelope.

4.2.2. Glacial loading

We used the same glacial model as in Hökmark et al. (2010), which contains two peaks of ice load affecting the Forsmark area as illustrated in Figure 63. Vertical stress reaches its maximum at around 12,000 years and 55,000 years, respectively. Maximum horizontal stress and minimum horizontal stress show similar trends as the vertical stress. This can be interpreted as the compressive vertical stress from the weight of the ice sheet increases, horizontal stress due to the confinement arises. At the time of 38,000 years, denoted as T3, the glacial stress decreases a little before the start of the second ice peak. The state at the time of 55,000 years, when the maximum vertical stress occurs, is named T4. Finally, the state when the ice has retreated and the state of stress is returning to its initial state at 58,000 years, is named T5. In this study, the effects of glacial loading and unloading will be analyzed at these specific times T3, T4 and T5.

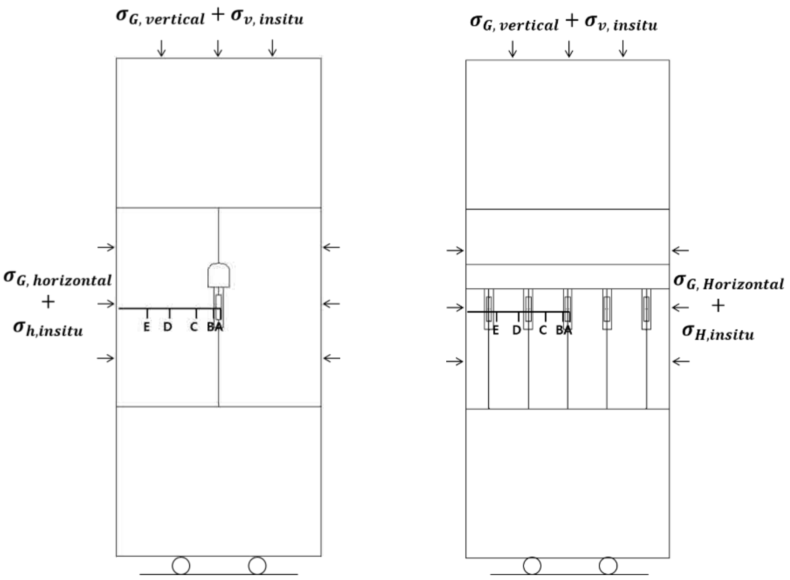

(a) (b)

Figure 62. Model geometry and boundary conditions for simulation of the glacial loading scenario. (a) NE section and (b) NW section. The tunnel geometry and in situ stress are the same as for thermo-mechanical analysis. Five monitoring points from A to E are placed on a horizontal line departing from the center of the canister at distances of 0 m, 0.92 m, 5.2 m, 10.1 m and 15 m, respectively.

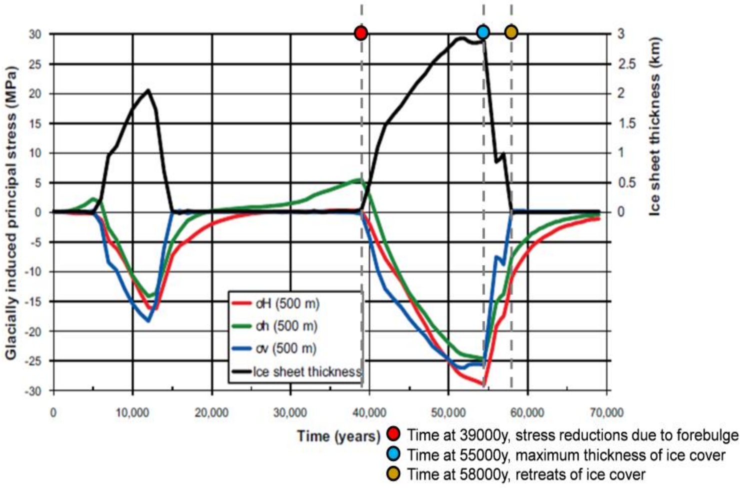

Figure 63. Glacially induced stress components in a future glacial cycle at 500 m depth in Forsmark (Hökmark et al. 2010). Three points in time are selected for the analysis: 38,000, 55,000 and 58,000 years after deposition.

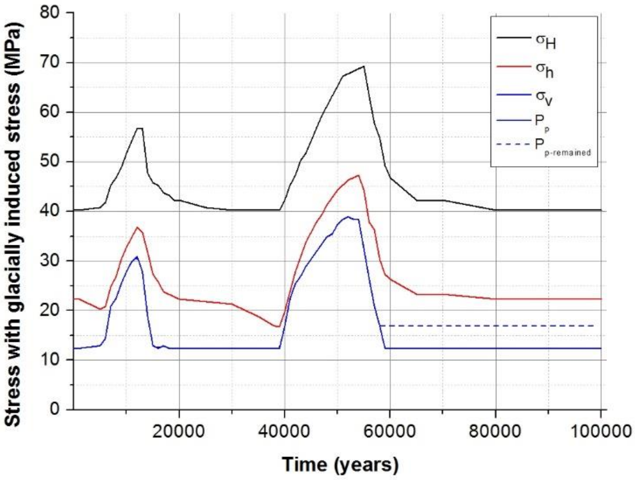

Figure 64. Total stress evolution during 100,000 years for a repository at 468 m depth. Vertical stress and pore pressure overlap.

Discrete stress increments for the three principal stresses as depicted in Figure 63 were superimposed on thermo-mechanical model in Chapter 3. The model was analyzed for the duration of 100,000 years. Reproduced glacial load evolutions considering in situ stresses and pore pressure are presented in Figure 64. Two pore pressure scenarios are considered: one with pore pressure equal to the vertical loading from the glacier; the other with remaining pore pressure after the glacially induced vertical stress is completely relaxed.

4.2.3. Conceptual model of fracture transmissivity evolution during the glacial phase

The first 10,000 years of the glacial phase are also analysed by means of a conceptual model to investigate the effect of pore pressure on the fractures with different orientation. The model geometry and mechanical properties of rock mass and fractures are identical to those used for the thermo-mechanical conceptual models as shown in Figure 23 and Figure 24.

Conceptual models are also conducted to investigate the effect of pore pressure on single fractures with different orientation. The model geometry and mechanical properties of the rock mass and fractures are identical to those shown in Figure 23 and Figure 24. The only difference between is that pore pressure is assigned to the fractures. The magnitude of pore pressure is 5 MPa and the water density is 1,000 kg/m^3. The boundaries of the model are assumed to be impermeable. There is no simulation of fluid flow, therefore, the pore pressure applied to the fractures only affects the calculation of the effective stress.

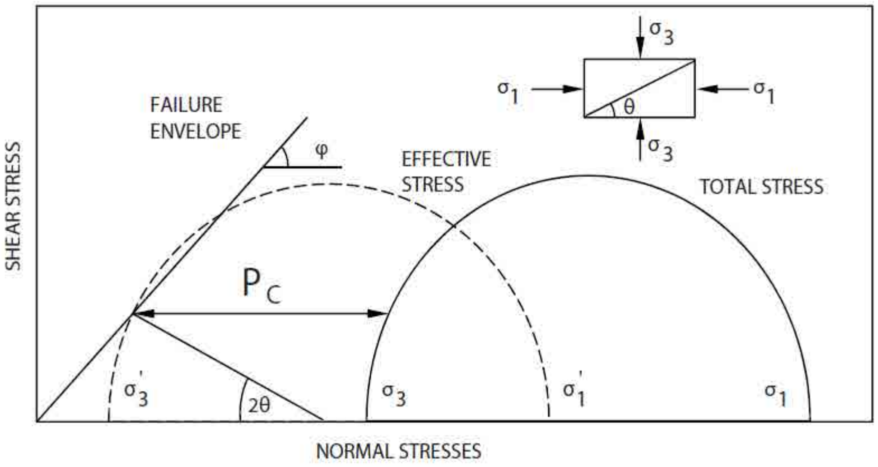

Figure 65. Mohr-Coulomb's diagram showing the influence of fluid pressure P_c on the condition for shear failure along failure envelope (Hökmark et al. 2010).

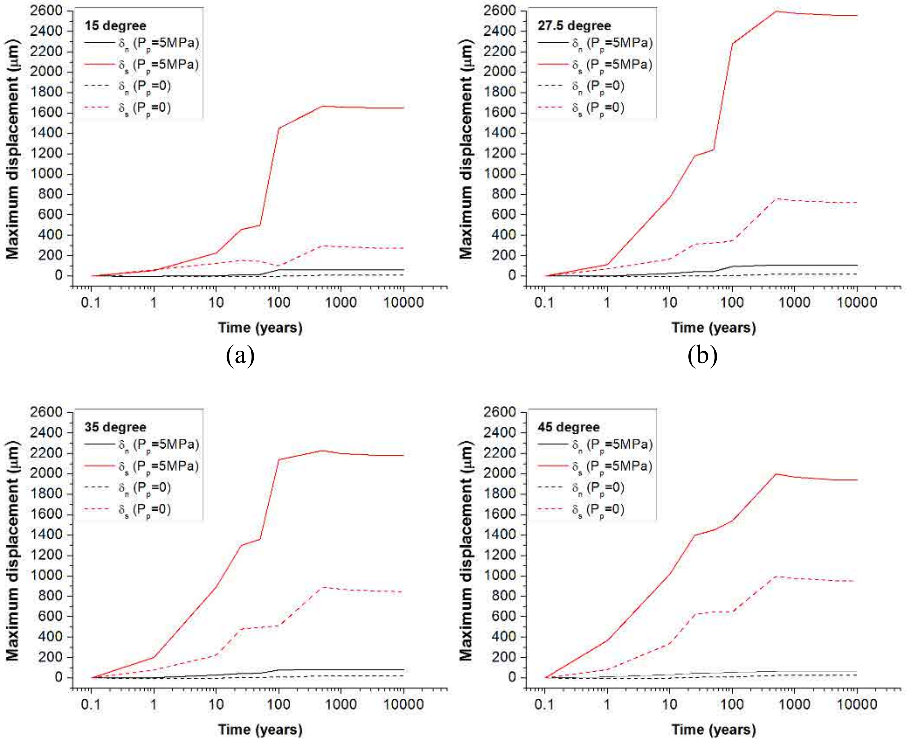

(a) (b)

(c) (d)

Figure 66. Fracture displacement for various orientation of a fracture below a canister in a repository during a period of 10,000 years that includes stress and pore pressure development due to the glacial phase. Each graph shows the effect of pore pressure in inclined fractures. Inclinations with respect to the direction of the maximum principal are: (a) 15°, (b) 27.5°, (c) 35° and (d) 45°. $\boldsymbol{\delta_n}$ and $\boldsymbol{\delta_s}$ in each legend means the normal displacement and shear displacement, respectively. Solid lines represent displacements of fractures with pore pressure; dotted lines represent fractures with zero pore pressure. For the geometry of the models, see Figure 24.

Figure 66 shows the results of conceptual modelling of a single fracture with different dip located below a canister with the spent nuclear fuel. A pore pressure of 5 MPa makes the fracture slip much easier compared to the case where zero pore pressure is assumed.The pore pressure makes the effective stress smaller and the the Mohr-Coulomb cicle in Figure 64 is moving towards the failure envilope. This results applies only to a specific fracure in a favourable condition for slip.

4.2.4. Independent modelling of the near-field with DFN for fracture transmissivity evolution during the glacial phase

DFN models with fracture data from NE02 and NW02 realizations are imported in the UDEC model for determining the transmissivity evolution during glacial phase. The input parameters are identical to those for the thermo-mechanical analysis except for the additional glacial stress and pore pressure (Table 3, 4 and 5). In this section, two glacial models named TG_NE02 and TG_NW02 are analyzed.

4.2.4.1. NE section

As a result of the thermo-mechanical and glacial loading analysis, the total stress variation during 100,000 years for the monitoring points presented in Figure 62 is obtained. For example, the minimum horizontal stresses at the monitoring points at 468 m depth are presented in Figure 67. The minimum horizontal stress is obtained by superimposing initial stress, thermal stress (first 10,000 years), glacially induced stress and pore pressure using the DFN model TG_NE02 of the NE section. Minimum horizontal stress evolutions up to 5,000 years are nearly the same as the thermo-mechanical analysis without influence of glacial loading and pore pressure. Vertical stress evolution shown in Figure 68 is also similar to the results presented in Figure 20 until the time 5,000 years. When the induced stresses by the glacial load are added from the time 5,000 years, the vertical stresses increase up to around 30 MPa at the first ice peak, and 40 MPa at the second ice peak. Figure 69 presents the stress ratio of minimum horizontal stress to vertical stress at various locations. As noted in the thermo-mechanical analysis in Chapter 3, the stress ratio increase to more than 3.5 during thermal loading. However, this high stress ratio is never achieved during the glaciation cycle. This is because the magnitude of glacial load is the same in both horizontal and vertical direction, which actually decreases the stress ratio. The largest stress ratio during the glaciation cycles is around 2.8, which is barely above the critical stress ratio for unfavorably oriented fractures. This implies that the glacial loading does not increase the potential of shear slip on fractures.

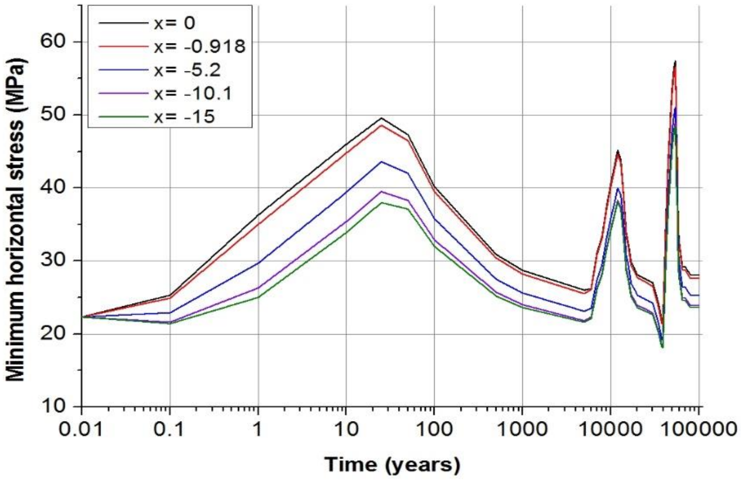

Figure 67. Minimum horizontal stress in the model TG_NE02 of the NE section loaded by initial stress, thermal stress and glacially induced stress at 468 m depth during 100,000 years. Five lines indicate stress variation at the different monitoring points at a horizontal distance *x* from the center of the canister (see Figure 62a).

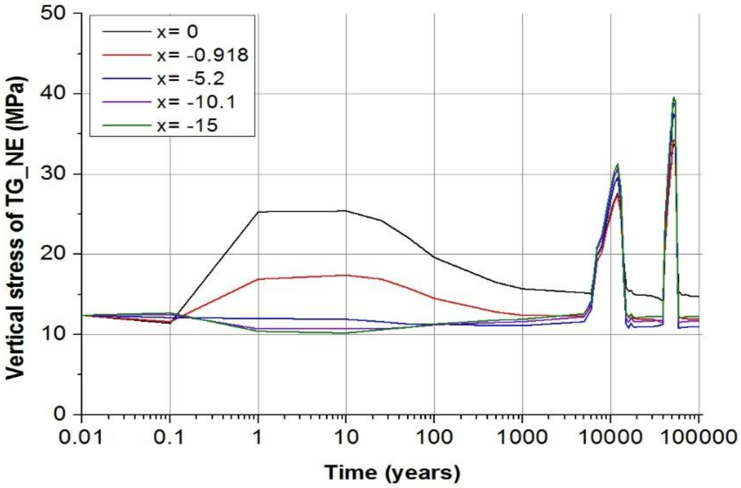

Figure 68. Vertical stress of model TG_NE02 superimposed on initial stress, thermal stress and glacially induced stress during 100,000 years at 468 m depth. Five lines indicate stress variation at the horizontal distance *x* from the center of the canister (see Figure 62a).

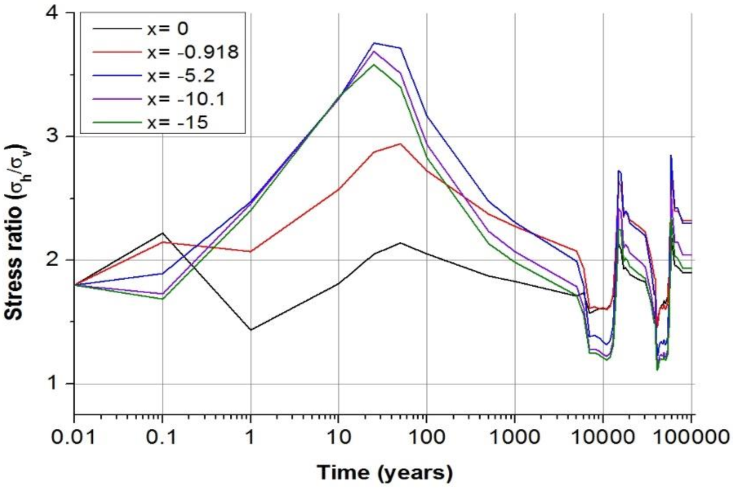

Figure 69. Stress ratio between the minimum horizontal and vertical stress at five monitoring points at 468 m depth of model TG_NE02 during 100,000 years. Five lines indicate stress variation at the horizontal distance *x* from the center of the canister (see Figure 62a).

There are two modelling cases in this section: a case without residual pore pressure after glacial loading and another case with a residual pore pressure after the retreat of ice sheet. The magnitude of the pore pressure is the same as the glacially induced vertical load. It is also expected that some fraction of the pore pressure would be maintained in rock mass after the ice sheet has melted as illustrated in Figure 64. Key fractures with respect to deformation in the TG_NE02 model are shown in Figure 70. Cumulative maximum normal and shear displacement of fracture 1 are 48.45 µm and 174 µm after 50 years and 52,000 years, respectively. Also, it is noted that normal and shear displacement that occurred during thermal loading did not return to original aperture when the horizontal and vertical stresses dropped to the initial stress value. However, the effect of glaciation is relatively minor compared to the thermal phase as shown in Figure 71, and displacements during this phase appear to be reversible.

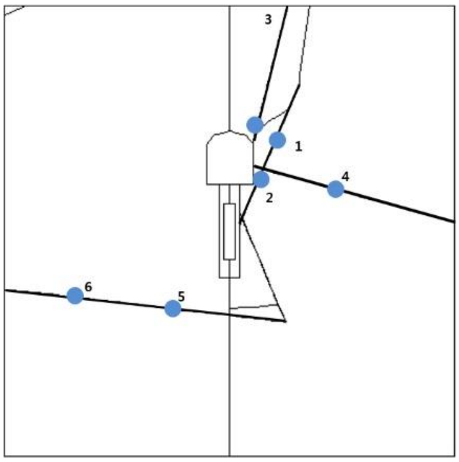

Figure 70. Illustration of fractures with large normal displacements in the TG_NE02 model. The blue dots indicate the location of maximum normal displacement.

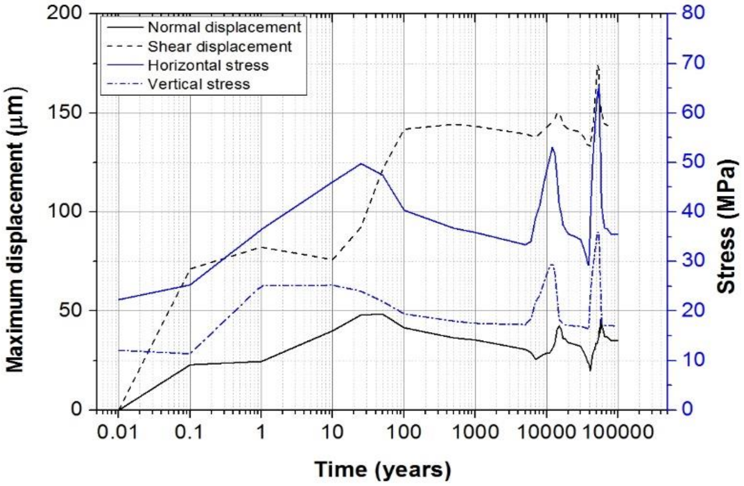

Figure 71. Evolution of the normal and shear displacement versus the normal and shear stress for fracture 1 in model TG_NE02 without residual pore pressure at the end of the glacial cycle.

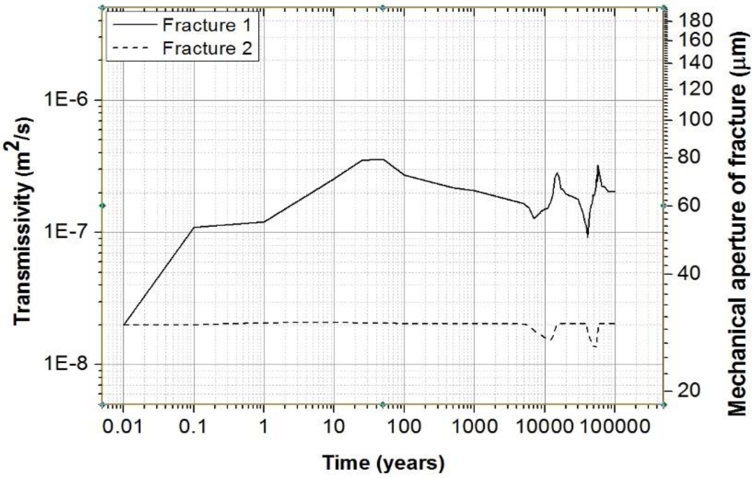

Figure 72. Mechanical aperture evolution and transmissivity versus time for model TG_NE02 with initial mechanical aperture of 30 μm.

It turned out that most the fractures experience closure during the ice peaks in the glaciation cycle as shown in Figure 72. However, transmissivity of fracture 1 increases from 2×10^{-8} m^2/s to 3.6×10^{-7} m^2/s during the thermal phase (e.g. 50 years), which is around one orders of magnitude increase for a fracture with initial aperture of 30 μm in the vicinity of the tunnel wall. This value (about 2×10^{-8} m^2/s) is then kept with secondary changes till the end of the glacial cycle. Figure 73 shows the relative transmissivity as a function of initial aperture of fracture using the results of fracture 1. When the magnitude of the initial aperture is 5 μm, the fracture transmissivity changes more than 3 orders of magnitude. However, most part of the changes occur during the thermal phase while the changes during the glacial phase mainly recovered after unloading.

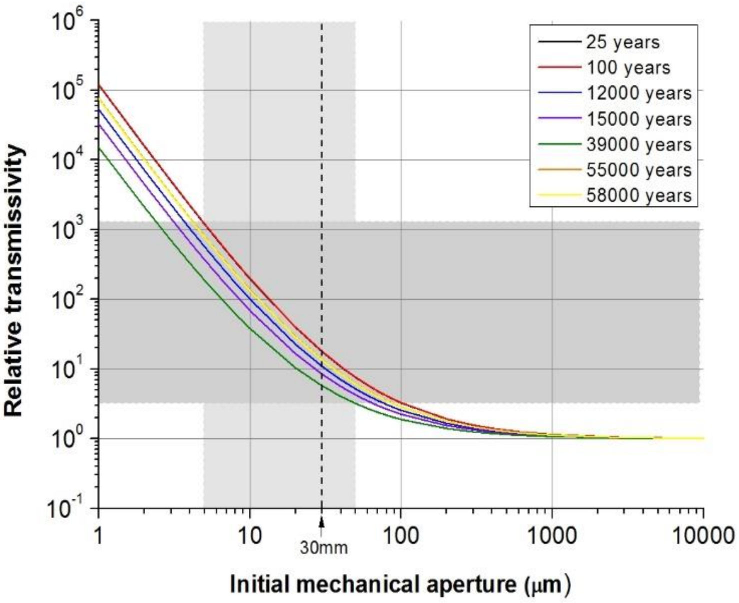

Figure 73. Relative transmissivity versus initial mechanical aperture using TM results of fracture 1 in model TG_NE02. Note that the transmissivity change is cumulative resulting from both thermal and glacial loading. Relative transmissivity change is largely governed by thermal loading.

The results of the TG_NE02 model with residual pore pressure shows very similar trends in transmissivity change as for the case without residual pore pressure. Therefore, the results are not presented here.

4.2.4.2. NW section

The same methodology as for the NE section was applied to the analysis on NW sections based on the NW02 DFN realization. The maximum horizontal stresses and vertical stresses at monitoring points along the horizontal level at 468 m depth are shown in Figure 74 and Figure 75. The maximum horizontal stress is obtained by superimposing virgin maximum horizontal initial stress, thermal stress at the canister, glacially induced stress and pore pressure. Similarly to the case TG_NE02, the case TG_NW02 includes two pore pressure with and without residual pore pressure after the retreat of ice sheet. Like for the NE model, the failure envelope could not be reached even considering the effect of fracture pore pressure due to absence of unfavorably oriented fractures.

The evolution of the maximum horizontal stress up to 5,000 years after initiation of loading for model TG_NW02 is nearly the same as for model TG_NE02, but it shows a more uniform stress distribution compared to NE section. This is obtained because there are five heat sources along the x direction which produce a uniform increase in thermal stress in that direction. The vertical stress evolution shown in Figure 75 is also similar to the results presented in Figure 20 until 5,000 years. When the ice load starts to develop at about 5,000 years, the vertical stresses increase up to around 36 MPa at first glacial peak and 44 MPa at second glacial peak. Figure 76 presents the stress ratio of maximum horizontal stress to vertical stress at various locations in the model. High stress ratios were achieved during thermal and glacial cycle in model with the NW section, and the stress ratio decreased when the glacially induced stress increased. This is because the same magnitude of glacial load is applied to horizontal and vertical direction. Also, the largest stress ratio during glaciation cycles was about 6.8, which is above the critical stress ratio for unfavorably oriented fractures. Unlike the analysis of NE section, this result implies that uniform heat source and glacial loading makes the ratio of maximum horizontal stress and vertical stress much larger.

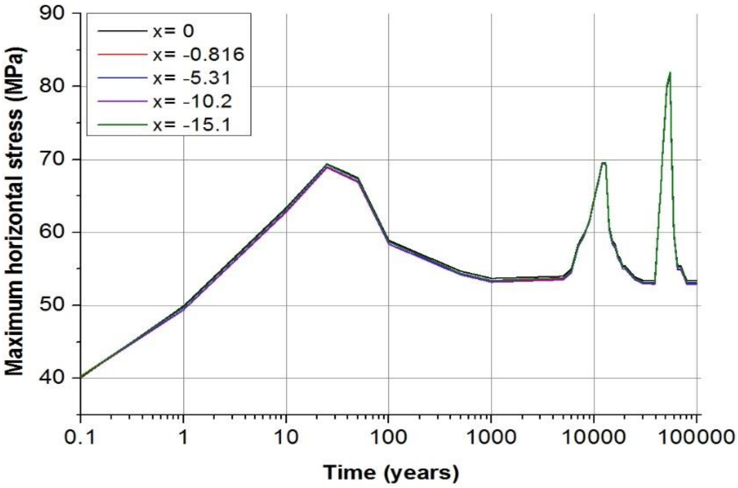

Figure 74. Maximum horizontal stress in the model TG_NW02 from superposition of initial stress, thermal stress and glacially induced stress during 100,000 years at monitoring points at 468 m depth. Five lines indicate stress variation at the horizontal distance *x* from the center of the canister (see Figure 62b).

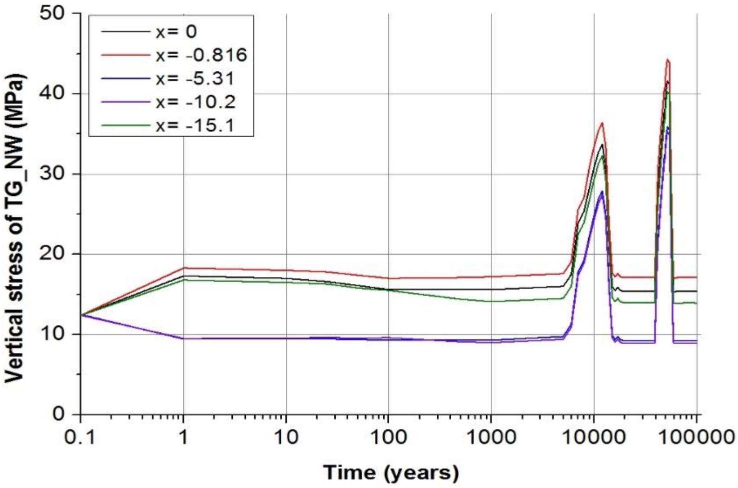

Figure 75. Vertical stress of model TG_NW02 from superposition of initial stress, thermal stress and glacially induced stress during 100,000 years at monitoring points at 468 m depth. Five lines indicate stress at the horizontal distance *x* from the center of the canister (see Figure 62b).

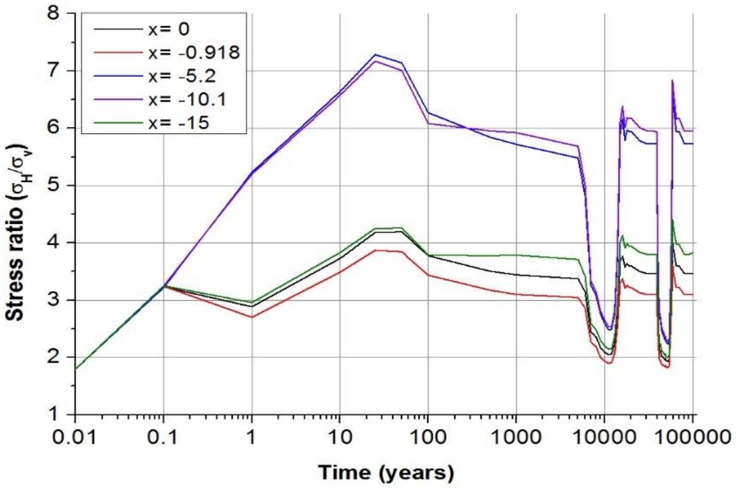

Figure 76. Stress ratios evolution for model TG_NW02 during 100,000 years at monitoring points at 468 m depth. Five lines indicate stress at the horizontal distance *x* from the center of the canister (see Figure 62b).

The location of large normal and shear displacement on fractures are indicated in Figure 77. The evolution of normal and shear displacement and normal and shear stress are shown in Figure 78. The results from model TG_NW02 are similar to those of the NE02 models. Cumulative shear displacement in fracture 1 is 75.13 µm after 25 years, and 1,063 µm after 58,000 years after deposition. However, the portion of shear displacement induced by glacial loading recovered after retreat of ice, which indicates that the shear displacement is elastic without causing significant and permanent dilation.

Also, the transmissivity of fracture 1 increases by more than one order of magnitude and then maintains the high value after the ice melting. The role of glacial loading is very small compared to that of thermal loading, and the generated displacements are recovered to their state before glacial loading. It also shows that the fractures are gradually closing as indicated by negative normal displacement when glacial loading is applied. It means that the glacial loading increases the frictional strength of fractures and rock mass.

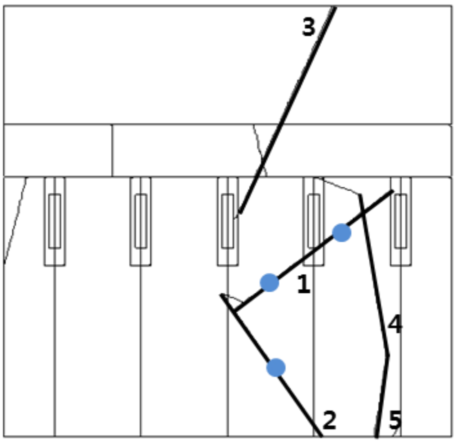

Figure 77. Illustration of fractures with large normal displacements in the TG_NW02 model. The blue dots indicate the location of maximum normal displacement.

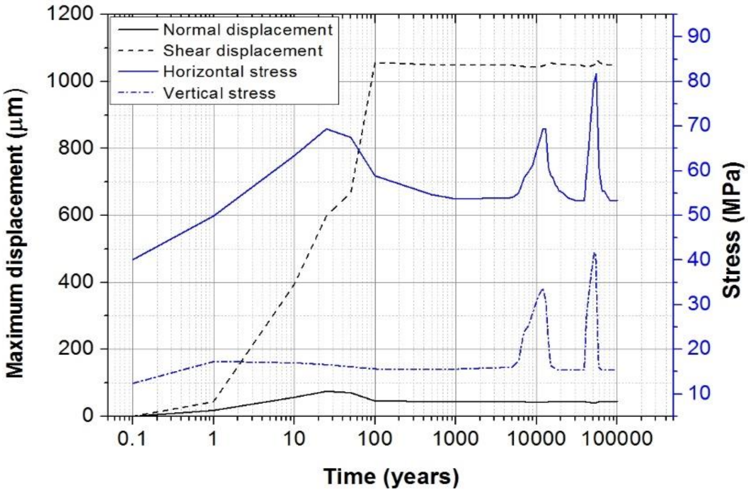

Figure 78. Evolutions of normal and shear displacement and normal and shear stress at fracture 1 for model TG_NW02 as shown in Figure 77. Notice the remaining shear displacement after around 100 years.

The transmissivity of fracture 1 at the vicinity of the heat source increases from 2×10^{-8} m^2/s to 8.61×10^{-7} m^2/s (Figure 79), which is an increase of more than one orders of magnitude. Also, the relative transmissivity which is a function of initial aperture of fracture can be obtained using the displacement of fracture 1. The transmissivity of this fracture changes by more than 3 orders of magnitude when the magnitude of the initial aperture is 5 μm. However, it is also noted that the change of transmissivity is mainly due to the thermal phase, and the effect of the glaciation is minor. A slight decrease of transmissivity in relation to the ice peaks as shown in Figure 79 indicates that fracture normal closure is a dominant mechanism for this particular case.

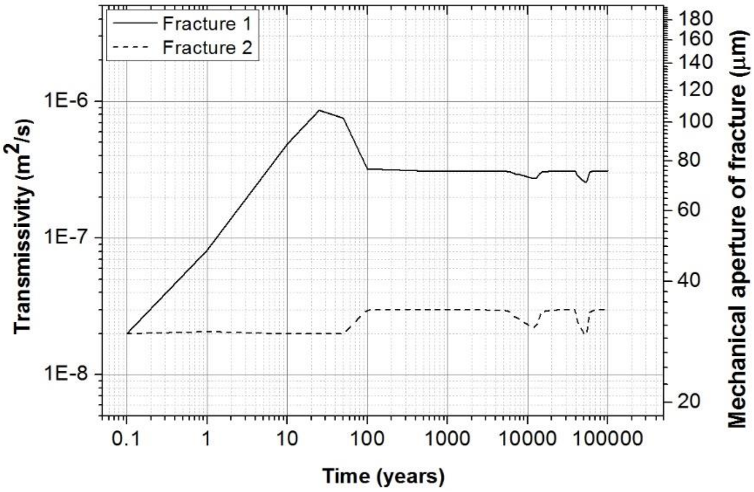

Figure 79. Mechanical aperture and transmissivity evolution versus time for model TG_NW02 with initial mechanical aperture of 30 μm.

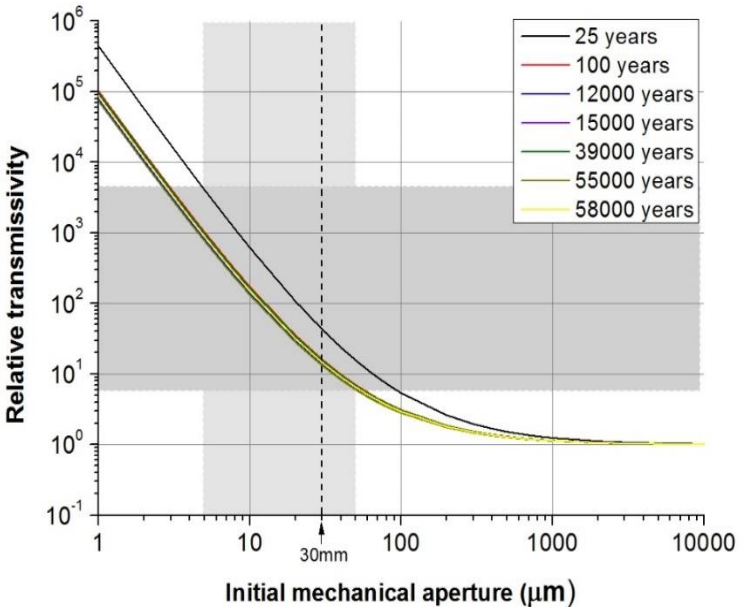

Figure 80. Initial mechanical aperture versus Relative transmissivity versus initial mechanical aperture using TM results of fracture 1 in model TG_NW02 in Figure 77. Note that the transmissivity change is cumulative resulting from both thermal and glacial loading. Relative transmissivity change is largely governed by thermal loading.

4.3. The Consultants' assessment on the evolution of transmissivity during the glacial phase based on independent TM modelling

The Authors' findings from the review and independent modelling on fracture transmissivity evolution during the glacial phase can be summarized as follows:

- Although SKB conducted relatively robust glaciation modelling considering two different pore pressure models, it still require more systematic analysis in terms of following aspect: 1) the role of shear dilation induced by up to 8 mm shear slip for fractures 100 m long; 2) the role of considering explicit fracture geometries based on realistic DFN realizations that alter the stress distribution around the deposition tunnels and holes.
- Independent analysis and modelling were conducted with explicit consideration of fractures from realistic fracture networks. The generated shear dilation due to glaciation is negligible because of the nearly isotropic increase of the glacially induced stresses. Furthermore, the changes of transmissivity due to glacial loading recover to their initial value indicating that the fracture deformation is elastic.

5. Modelling of the evolution of fracture transmissivity during an earthquake close to the repository

Earthquakes essentially shake the ground and can, in principle, induce large shear displacements. Large shear displacements might produce dilation of the fractures, which in turn means the fracture transmissivity might increase. The significance of the fracture transmissivity change during an earthquake will, among other factors, depend upon the magnitude of the earthquake. With a given earthquake, the extent of fracture transmissivity change will be also a function of the size, orientation, connectivity and hydro-mechanical properties of fractures. Well-connected and unfavorably oriented large fractures with low friction angle will undergo larger fracture transmissivity change in analogy with what was shown in previous thermo-mechanical analysis of the conceptual model. Similarly to the thermo-shearing mechanism, transmissivity changes are likely to be permanent and irreversible when plastic fracture deformation occurs. Therefore, the effect of an earthquake has to be investigated in terms of consequences on the hydro-mechanical behavior of the fractures.

5.1. SKB's presentation

5.1.1. SKB's analysis of effect of an earthquake on transmissivity change

SKB has tackled the effect of earthquake on the repository performance mainly in terms of repository layout and design (Fälth et al., 2010). The main variable in such analysis is the shear displacement of the target fractures that may affect the canister integrity. Although SKB did recognize the potential effect of earthquake on the hydro-mechanical changes due to shearing and dilation, they concluded that it is neither meaningful nor necessary to describe or quantify the bulk hydraulic changes in the host rock occurring as a response to earthquake (Hökmark el al., 2010, p. 11). This conclusion was only qualitatively supported by claiming that the net result of the impact of an earthquake close to the repository is judged to be a reorganization of the flow pattern rather than a systematic increase or decrease of the transport capacity of the repository bed rock (Hökmark el al., 2010). We emphasize that a more quantitative analysis is necessary to support the SKB's argument that the effect of earthquake on hydraulic change is negligible.

SKB conducted a comprehensive analysis of the effect of large earthquake on a KBS-3 repository (Bödvarsson et al., 2006; Fälth et al., 2010). In this analysis, SKB retained the view that the seismic impact on the transport properties in general is not an issue for the safety assessment and the change of the hydraulic system will occur only when the fracture shear slip is large enough to cause a mechanical damage to the canisters, which will then result in the short-circuit between the rock fractures and the biosphere. However, we emphasize here that significant fracture transmissivity can occur even without the damage of canister.

5.1.2. Effect of earthquake on fracture shear slip

SKB conducted a novel and extensive analysis on the effect of earthquake on fracture shear slip displacement. This analysis has been conducted in order to calculate the amount of fracture shear slip that can affect the canister integrity. Numerical modelling was conducted by dynamic analysis through release of the fracture cohesive strength of the earthquake generating or primary fault during a specific period of time defined as ‘reduction time’. Geometric outlines of SKB’s earthquake modelling are shown in Figure 81a. The target fractures, on which the effects of the earthquake are quantified, are horizontal and dipping 45°. Figure 81b shows induced fracture shear displacement at distances 200 m, 600 m and 1000 m from the primary fault. Based on the threshold of 5 mm shear displacement for the integrity of the canister, critical radii of the fractures were calculated and recommended. Critical radii vary depending on the distance to the primary fault, the fault’s surface trace length and the target fracture dip angle. When surface trace length of the fault was larger than 5 km, the critical radius of the target fracture within distance range 100 m to 200 m was recommended to be 62.5 m. Although extensive analysis has been conducted for fracture shear displacement, the fracture transmissivity change due to the dilation of target fractures was not investigated systematically mainly due to the notion that large normal stress can suppress the dilation of the fracture (Fälth et al., 2010).

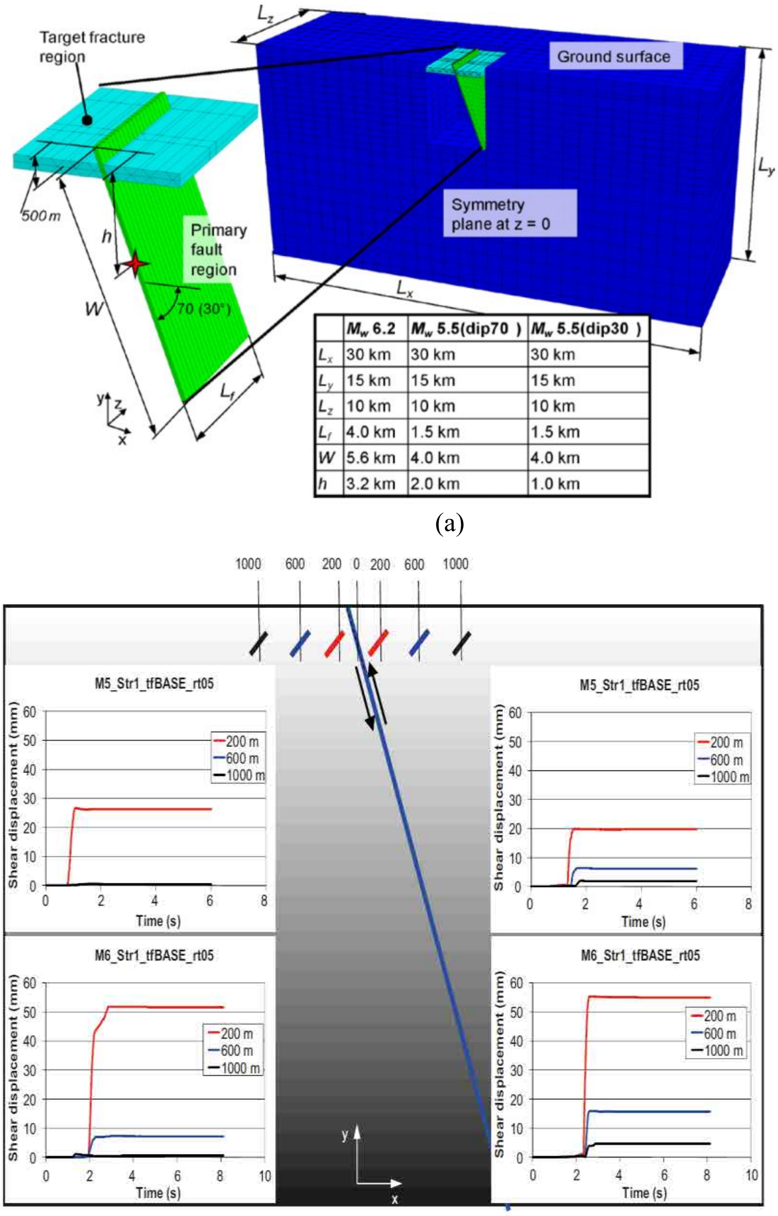

	M_w 6.2	M_w 5.5(dip70)	M_w 5.5(dip30)
L_x	30 km	30 km	30 km
L_y	15 km	15 km	15 km
L_z	10 km	10 km	10 km
L_f	4.0 km	1.5 km	1.5 km
W	5.6 km	4.0 km	4.0 km
h	3.2 km	2.0 km	1.0 km

(a)

(b)

Figure 81. (a) geometric outlines of SKB's earthquake model, and (b) shear displacement of target fractures. Target fractures were located up to 1500 m apart with 150 m radii in size (Fälth et al., 2010).

5.2. Motivation of the assessment on evolution of transmissivity by independent modelling of an earthquake

Earthquake loading (SKI, 1992; SSM, 2011) is applied in addition to thermo-mechanical and glacial loading in order to investigate the possible transmissivity change of target fractures in the repository. The earthquake loading is simulated by the UDEC code, which is suited for dynamic analysis of rock masses (Itasca, 2014; Pal et al., 2012).

5.2.1. Data and geometry for earthquake loading phase

Data and geometry are the same as for near-field TM analysis presented in Section 3.2.1, except for the dynamic loading and boundary conditions during earthquake. To implement dynamic analysis in this small-scale model, viscous boundary (all boundaries) and free field boundary (only the vertical boundaries) are assigned to the model block. Viscous boundary conditions help block model to behave as an infinite rock mass which means that there is no reflection of wave. Also, no distortion along the vertical boundary occurs at the vertical boundary. These special techniques can make the seismic input applied to the bottom boundary propagate upward properly through the entire model. In addition, mechanical Rayleigh damping is applied to the time domain analysis to make an energy loss as a results of internal friction and slippage along joints. However, there has not been a specific method to determine the magnitude of damping ratio yet. Therefore, by following the practical ratio of damping for underground modelling, 5% of Rayleigh mass damping is applied when the dynamic stress is applied in this study.

In this section, NE02 and NW02 DFN models are used for earthquake modelling. Modelling geometries for earthquake loading are shown in Figure 83, and the excavation of the tunnel is simulated only in NE02 model. Special boundary conditions of free field boundary and viscous boundary were used for this analysis as also illustrated in the figure. The free field boundary makes modelling block behave as an infinite rock mass by reducing large strain at the vertical boundary and prohibiting reflection of wave propagation.

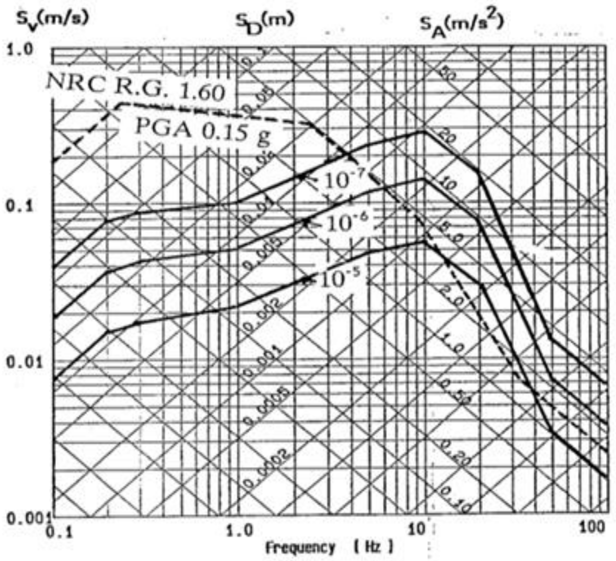

Figure 82. The original Swedish design response spectrum based on NRC R.G. 1.60 and scaled to Peak Ground Acceleration PGA = 0.15 g for horizontal acceleration, compared with suggested Envelope Ground Response Spectra for 10^{-5}, 10^{-6} and 10^{-7} annual events per site (SKI, 1992).

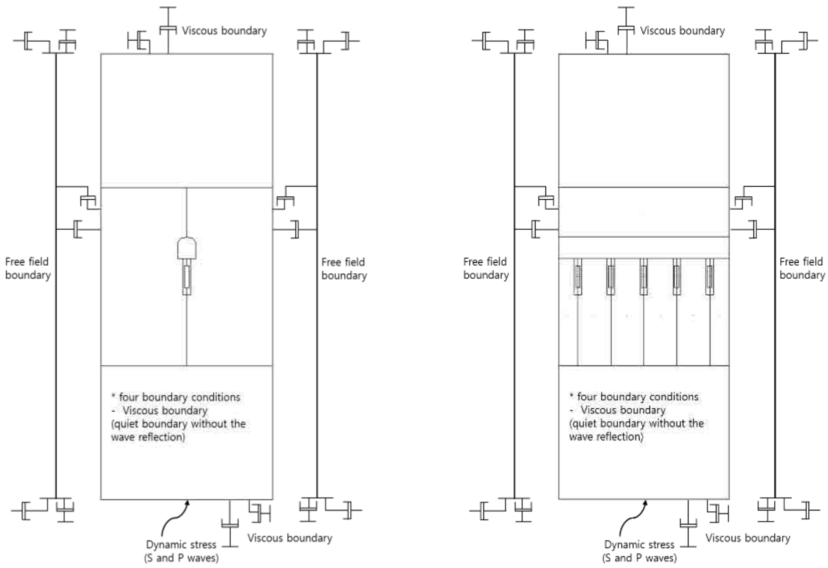

(a) (b)

Figure 83. Boundary condition for earthquake loading. (a) TGEQ_NE02 model, (b) TGEQ_NW02 model. Four boundaries have viscous damping which prevents wave reflection. This is required because the model is inside an infinite rock mass. Dynamic loading is applied at the bottom of the model for a given duration of time.

5.2.2. Earthquake loading

In order to calculate the applied dynamic loading, the following equations are applied (Itasca, 2011):

$$\sigma_n = 2(\rho C_p)\,\mathrm{v}_n$$ Eq. (5.1)

$$\sigma_s = 2(\rho C_s)\,\mathrm{v}_s$$ Eq. (5.2)

$$C_p = \sqrt{\frac{K + 4G/3}{\rho}}$$ Eq. (5.3)

$$C_s = \sqrt{\frac{G}{\rho}}$$ Eq. (5.4)

where σ_n is an applied normal stress, σ_s is applied shear stress, ρ is mass density, C_p is speed of p-wave propagation through medium, C_s is the speed of s-wave propagation through medium, v_n is input normal particle velocity, and v_s is input shear particle velocity. These equations can be applied to plane-wave conditions. Also, the factor of two in Eq. (5.1) and (5.2) is needed because the applied stress must be doubled to overcome the effect of the viscous boundary (Itasca, 2011; Itasca, 2014; Damjanac, 1999). Using these relationships, the magnitude of applied stress is obtained from the velocity models that are taken from synthetic ground motion time-histories for a typical hard rock site in Sweden (SKI, 1992).

Characterization of seismic ground motion is based on the probabilistic analysis of nuclear facilities in Sweden (SKI, 1992). As shown in Figure 84, the horizontal and vertical envelope spectra that had been calculated in SKI.

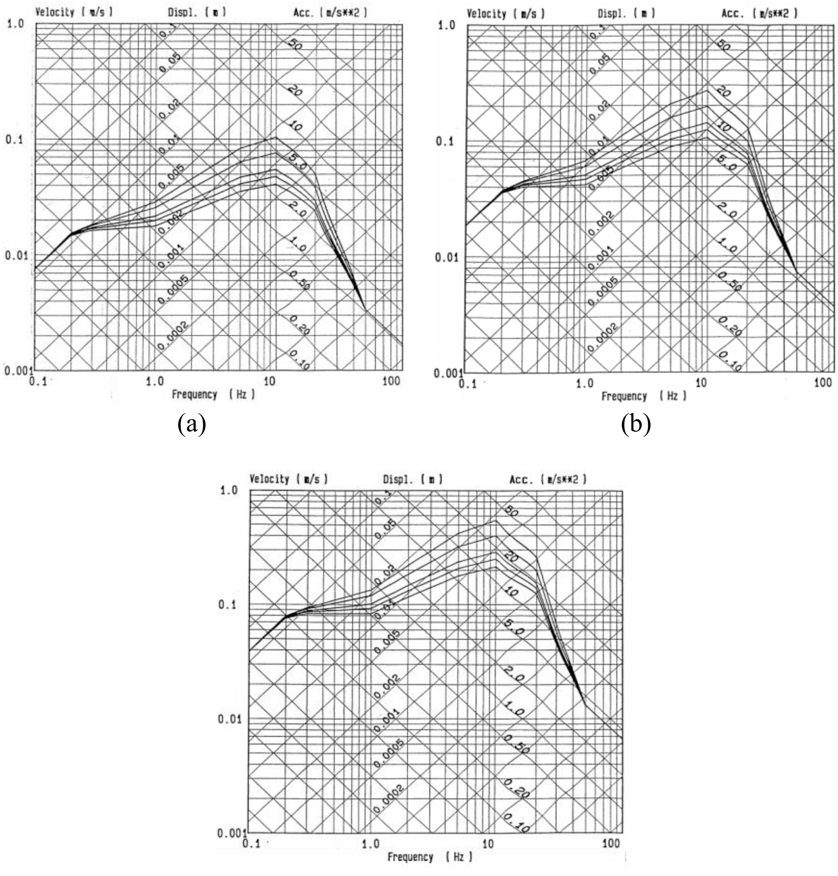

(a) (b)

(c)

Figure 84. Horizontal envelope spectra (a) 10^{-5} yearly probability level (b) 10^{-6} yearly probability level, and (c) 10^{-7} yearly probability level. Each line is calculated with different damping ratio. From the upper line to the bottom line, each damping ratio is 0.005, 0.02, 0.05, 0.07, 0.10, respectively (SKI, 1992).

Synthetic ground motion time-histories for each envelope spectrum exceedance for 10^{-5}, 10^{-6} and 10^{-7} annual events per site were produced as shown in Figure 85. Velocity histories are converted into shear and normal stress histories based on Eq. (5.1) to Eq. (5.4).

Using these data sets, earthquake loading is applied to the TG_NW02 modelling during 10.5 seconds. There are four specific times during a glacial cycle when the dynamic loading is applied. T1, T3, T4 and T5 are chosen as shown in Figure 86, because these points are the time of maximum vertical loading (T1 and T4) and zero vertical loading (T3 and T5).

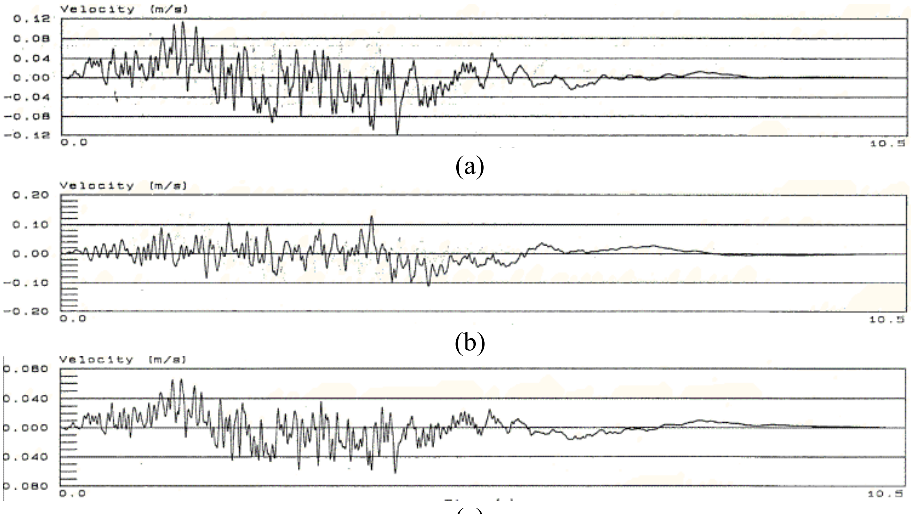

(a)

(b)

(c)

Figure 85. Time history based on envelope spectra with envelope spectrum yearly exceedance frequency 10^{-7}. Ground motion velocities are: (a) horizontal 1, (b) horizontal 2, and (c) vertical direction (SKI, 1992).

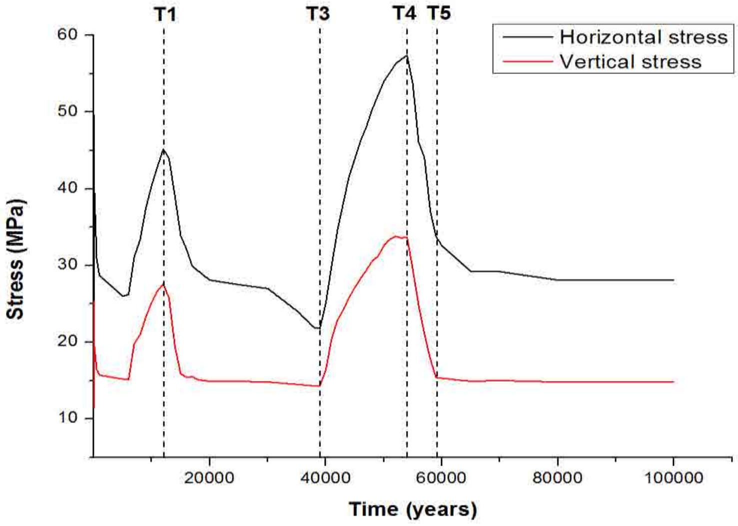

Figure 86. Time for dynamic loading specified at distinct locations during a glacial cycle. Shear stress from earthquake loading will be applied at four specific times of the SKB glaciation scenario: 12,000 years (T1), 38,000 years (T3), 55,000 years (T4) and 58,000 years (T5).

5.2.3. Conceptual model of shear displacement evolution during an earthquake

Similarly to thermo-mechanical and glacial loading analyses as discussed in Chapter 3 and 4, the relative shear displacement within a fracture is calculated by Eq. (3.2) according to Pollard and Segall (1987). Using this relationship between shear stress and shear displacement, the effects of dynamic shear stress are verified for the conceptual model containing a single fracture.

A conceptual square block model was initially loaded with 22 MPa and 12 MPa of principal stress with the orientation indicated in Figure 87. Considering the direction of the fracture, normal and shear stress on the fracture plane is calculated to be 17 MPa and 5 MPa, respectively. Mechanical properties of block and fracture are presented in Table 7.The length of fracture is 4.84 m, and the approximate of shear displacement as a result of dynamic loading can be calculated using Eq. (3.2). Because of this static loading and low friction angle of the fracture, the shear displacement occurs along the fracture as shown in Figure 87. The trend is largely similar to Figure 21b for static analysis. Maximum shear displacement was 467.3 µm when the friction angle is 5° as shown in Figure 88. This response is a function of the friction angle of the fracture, no meaningful shear displacement is observed when the friction angle is 35.8°.

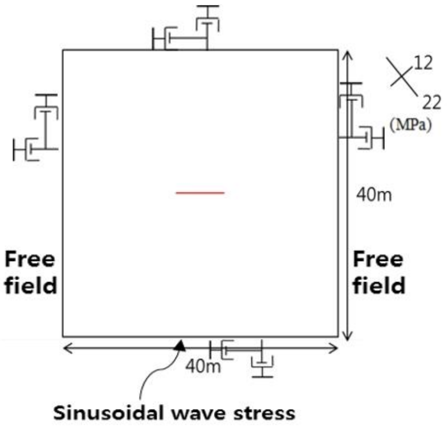

Figure 87. Geometry of conceptual model of a single fracture subjected to dynamic stress. Thermal source is not simulated in this model.

Table 7. Mechanical properties of rock block and fracture.

For depth > 400m	Unit	value
Density	[kg/m^3]	2,700
Shear modulus	[GPa]	32
Poisson's ratio	[-]	0.24
Tensile strength	[MPa]	0
Friction angle	[°]	5
Dilation angle	[°]	10
half-length of crack	[m]	2.42

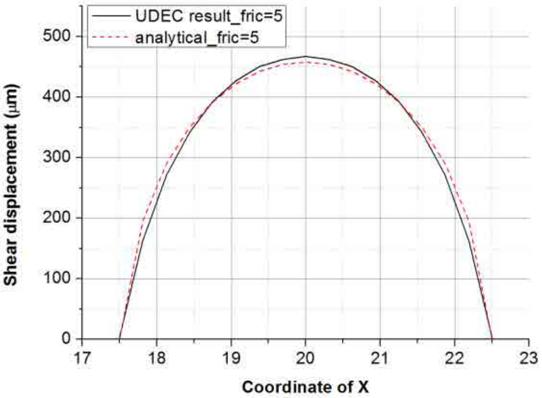

Figure 88. Comparison between shear displacement of UDEC model and analytical solution for shear displacement when friction angle of fracture is 5°. It shows that the static and dynamic equilibrium results match quite well.

After static equilibrium is reached in the model, dynamic shear stress is applied at the bottom boundary of the model and the given sinusoidal stress propagates through the entire model during the duration of dynamic loading. In the conceptual model a simplified sinusoidal wave is used first with frequency of 0.5 Hz and amplitude of 1 MPa. The sinusoidal shear stress was applied in the bottom of the model with the duration of 2 seconds, and the response was monitored for 2.5 seconds. Therefore, one period of sinusoidal seismic wave is able to transmit through the single fracture model. In order to simulate the infinite nature of surrounding rock mass, a viscous boundary is assigned to each boundary. Figure 89 shows the applied shear stress and measured x-velocity at the center of bottom boundary. According to Eq. (5.2), applied x-velocity can be exactly converted from applied shear stress, which proves that the dynamic model used in this study properly model the dynamic loading and associated response. Considering the relatively small size of the conceptual model, it is noted that the damping is not considered in the current analysis.

Figure 90 shows the displacement vectors at the vicinity of the 4.84 m long fracture and fracture opening due to the earthquake loading. Figure 90b is the magnitude of normal displacement only due to earthquake shear stress (normal displacement that occurred in static state is subtracted).

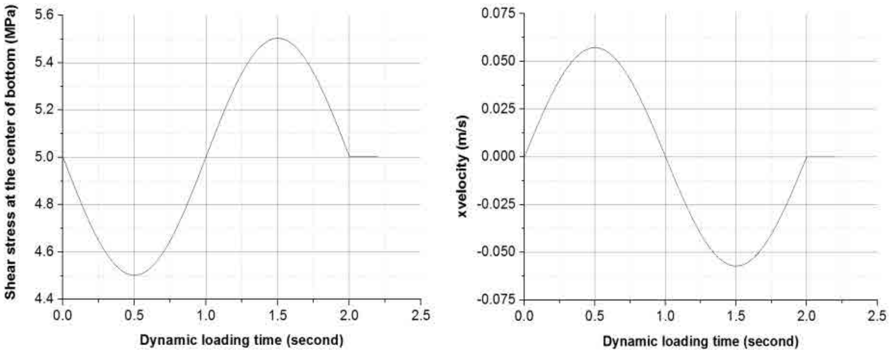

(a) (b)

Figure 89. (a) input seismic wave and (b) monitored *x*-velocity at the centre of bottom boundary. The relationship between applied shear stress and monitored *x*-velocity matched with Eq. (5.2). Phases of shear stress wave and *x*-velocity are following sign convention of UDEC code. Note the sign convention of negative shear stress which directs toward positive *x*-direction in the bottom of the model.

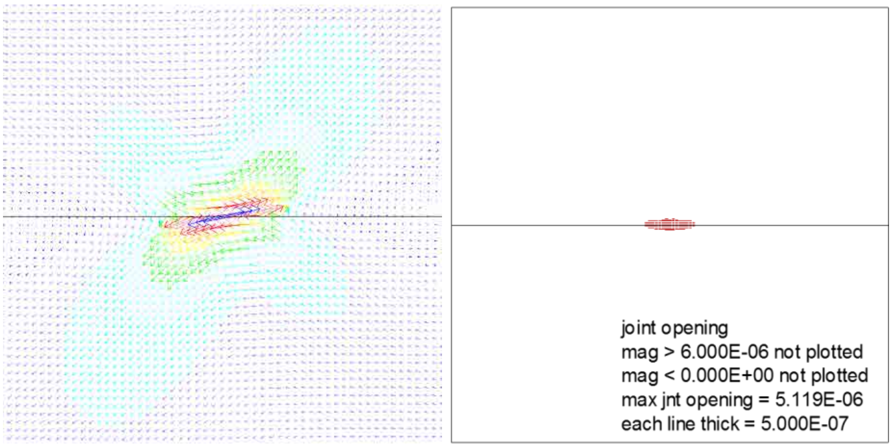

(a) (b)

Figure 90. Effects of earthquake loading. Shear stress applied to the bottom boundary of conceptual model makes shear displacement and joint opening. (a) directions of displacement at the vicinity of the 4.84 m length fracture, and (b) fracture opening magnitude.

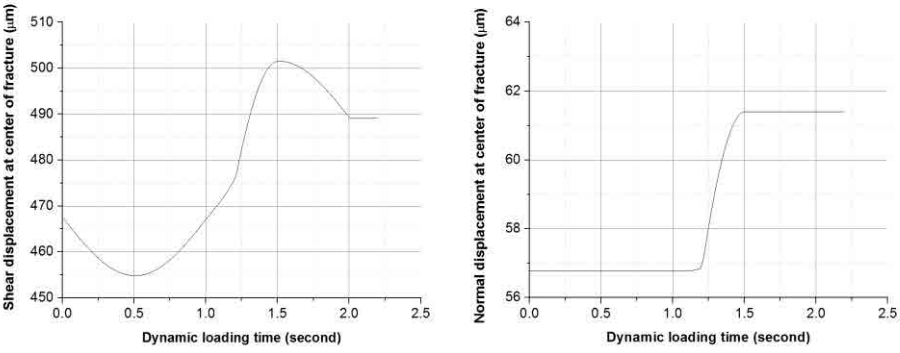

(a) (b)

Figure 91. Results of dynamic loading of conceptual model: (a) shear displacement and (b) normal displacement at the centre of the single fracture. The magnitude of maximum dynamic residual shear displacement is in agreement with predicted displacement by static analytical solution in Eq. (3.2).

Figure 91 shows that shear and normal displacement at the center joint. The residual value of maximum shear displacement is similar to the one estimated by the analytical solution Eq. (3.2). Shear displacement is increased from 467 μm to 489 μm. Normal displacement occurred due to the dilation after the plastic shear displacement and the magnitude of dilation (from 57 μm to 61 μm) matched well with the following relationship between normal dilation and shear displacement:

$$\delta_n = \tan(\varphi) \cdot \delta_s \qquad \text{Eq. (5.5)}$$

where δ_n is a normal displacement, δ_s is a shear displacement, and φ is a dilation angle. It is noted that shear displacement induced by sinusoidal shear stress did not recover to the initial state because the fracture frictional strength was acceded causing irreversible deformations. Normal dilation of the fracture in the magnitude of more than 6 μm was also observed and the dilated fracture did not recover to its initial state as predicted. This result for a simple conceptual model demonstrates well that the earthquake loading can trigger the plastic shear displacement and fracture dilation, which are both irreversible and permanent.

The shear and normal displacements of the fracture in the conceptual model increase with the increase of applied shear stress as shown in Figure 92. Applied shear stresses are 1 MPa, 2 MPa and 5 MPa and resulting residual displacements are shown in the figure. The shear and normal displacements also increase with the increase of the size of fracture as shown in Figure 93. Sinusoidal shear stress with amplitude of 1 MPa is applied for 2 seconds in the bottom of the model with joint length of 10 m and 15 m.

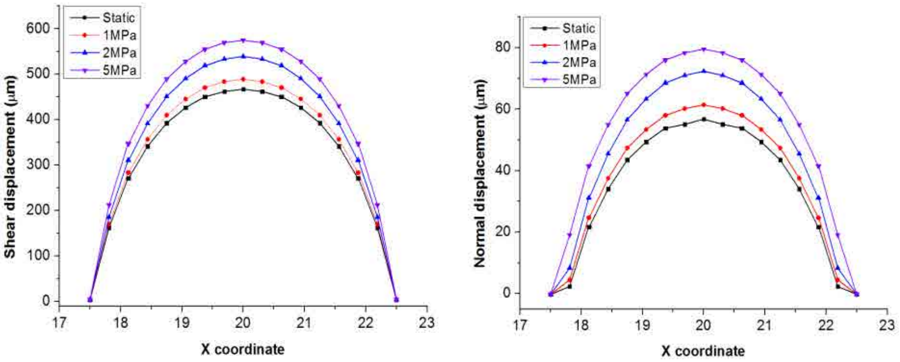

(a) (b)

Figure 92. Shear and normal displacement of the fracture in terms of different amplitude of shear stress wave. Permanent displacements after dynamic loading are lower than the magnitudes of maximum displacement during dynamic loading.

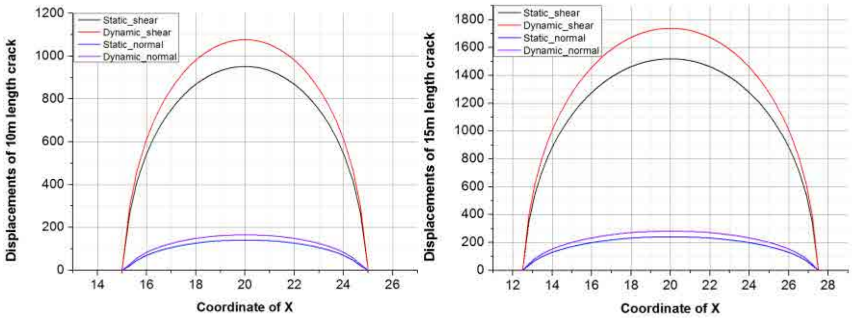

(a) (b)

Figure 93. Shear displacement and normal displacement in terms of different wave length of shear stress wave: (a) 10 m long fracture and (b) 15 m long fracture. Dynamic loading makes both shear and normal displacement increase compared to the results of static loading.

After confirmation on the response of dynamic shear loading, a more realistic synthetic ground response time history was applied as a boundary condition. Velocity time histories with the maximum amplitude extracted from information on Figure 85a and c are applied to the bottom boundary of the single fracture model of Figure 87. Horizontal velocity with yearly exceedance frequency 10^{-7} is converted to shear stress, and this wave propagates in form of S-wave through the model in positive *y*-direction. Similarly, the vertical velocity is converted to normal stress, and this wave propagates in form of P-wave. It also propagates through the model in positive *y*-direction.

Figure 94 shows the input shear stress time histories and measured *x*-velocity at the bottom of the model, in which the initial shear stress is 5 MPa. Applied shear stress fluctuation occurred around this initial shear stress of 5 MPa. Measured *x*-velocity at the bottom of the model shows that it is matched very well with the input horizontal velocity in Figure 85a. From the diagrams in SKI (1992, Figure 5), an excedance frequency of 10^{-7} per year would correspond to a seismic moment M_0 of about 2×10^{15} Nm, which would correspond to a moment magnitude of about 4.2. Variations of the shear stress of about 2 MPa were obtained by Backers et al. (2014)

in relation to an earthquake of moment magnitude 6 in the vicinity of the repository. Their models considered large scale earthquakes on a regional model scale for Forsmark and calculated the stress increments due to an earthquake at the depth of the repository.

Figure 95 presents the results of dynamic loading using synthetic ground motion time history. The duration of dynamic loading is 10.5 seconds and analysis continued until 11.5 seconds. The maximum increment in shear stress is 1.03 MPa. Both shear and normal displacement at the end of dynamic loading did not recover to their initial state showing a reversible process.

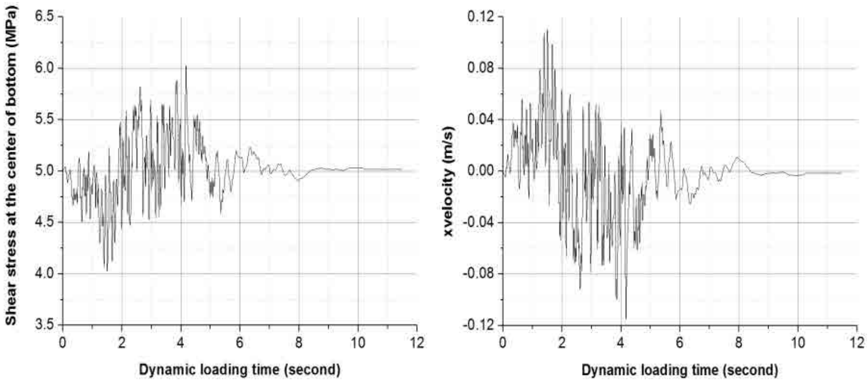

(a) (b)

Figure 94. Input shear stress and measured *x*-velocity in the bottom of the single fracture model. (a) Shear stress wave using synthetic ground motion time history, (b) *x*-velocity at the centre of bottom boundary.

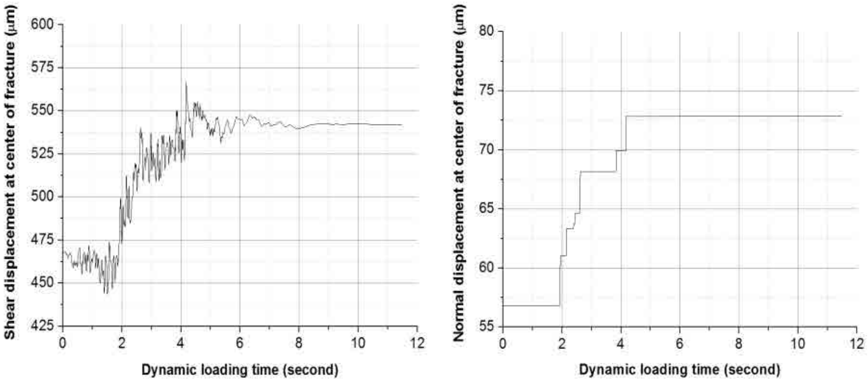

(a) (b)

Figure 95. Shear displacement (a) and normal displacement of single fracture when S-wave is applied.

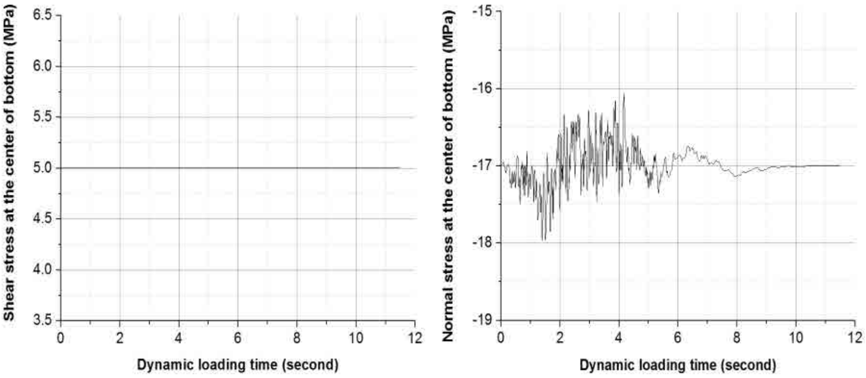

(a) (b)

Figure 96. (a) measured shear and (b) normal stress wave in the single fracture model using synthetic ground motion time history. Vertical velocity of envelope spectrum yearly exceedance frequency 10^{-7} is converted to normal stress.

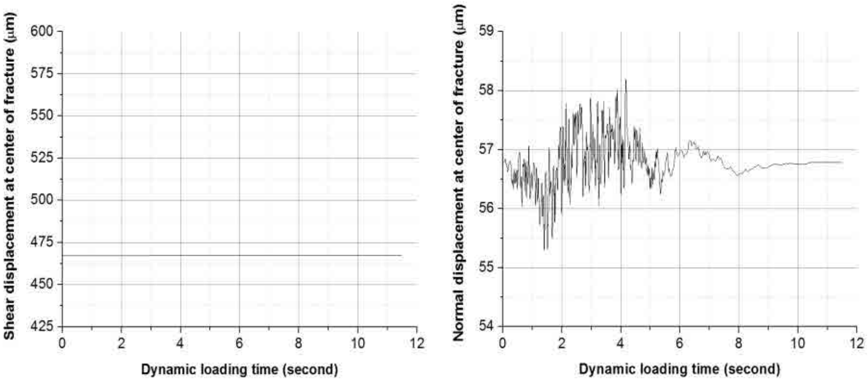

(a) (b)

Figure 97. (a) Shear displacement and (b) normal displacement of single fracture in model TG_NW02 when P-wave is applied.

A separate analysis with only vertical velocity time history is also conducted to verify the response due to normal stress time histories. Vertical synthetic ground motion histories in Figure 85c is converted to normal stress (P-wave) and then applied at the bottom of the single joint model. Figure 96 shows shear and normal stress at the center of bottom boundary. It is noted that the initial static normal and shear stress are 17 MPa and 5 MPa, respectively. It is clear from the result presented in Figure 96 that the applied normal stress hardly affects shear stress, and it only affects the normal stress responses. The fluctuation of shear displacement is very small comparing to the case by shear stress histories (S wave propagation) as shown in Figure 97a. Despite of same magnitude of maximum increment in normal stress is 1.0 MPa, normal displacement at the end of dynamic loading is nearly recovered to its initial state as shown in Figure 97b. This is comparable results with those of S-save propagation.

The final dynamic analysis was conducted with both horizontal and vertical velocity histories from synthetic ground motion (Figure 85a and c) by converting the velocity histories to shear and normal stress (S-wave and P-wave). Both shear and normal stress time histories are then applied to the bottom of the single fracture model at the same time. Figure 98 shows curves of shear and normal stress applied at the center of bottom boundary. Initial normal and shear stress are 17 MPa and 5 MPa, respectly.

Dynamic loading is applied at the bottom boundary and also the maximum increment in shear and normal stress are not over 2 MPa. Shear and normal displacement are very similar with the one with separate S- and P-wave application. Normal displacement at the end of dynamic loading with both shear and normal stress histories is nearly identical with the one with only shear stress time histories.

Based on the results presented from the conceptual models, dynamic loading can generate permanent shear slip when the applied stress regime becomes unfavourable and reach the frictional failure of the fracture. As these conceptual models have been computed with very low friction angle and large dilation angle (10°), the outcome is clearly towards dilation behaviour. As these parameters are intentionally selected to demonstrate earthquake induced permanent shear displacement followed by dilation, the response in real DFN situations may not follow these patterns due to higher friction angle and less unfavourable fracture orientations.

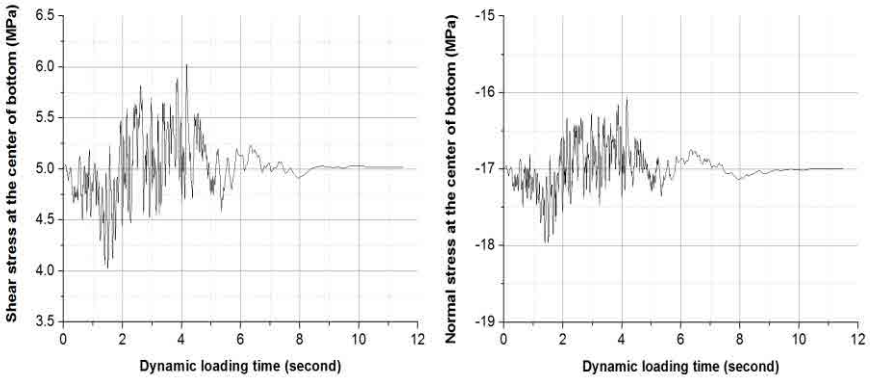

(a) (b)

Figure 98. (a) input shear stress wave and (b) normal stress wave using synthetic ground motion time history on the single fracture model. Velocities of envelope spectrum yearly exceedance frequency 10^{-7} (Figure 85a and c) are converted to shear and normal stress.

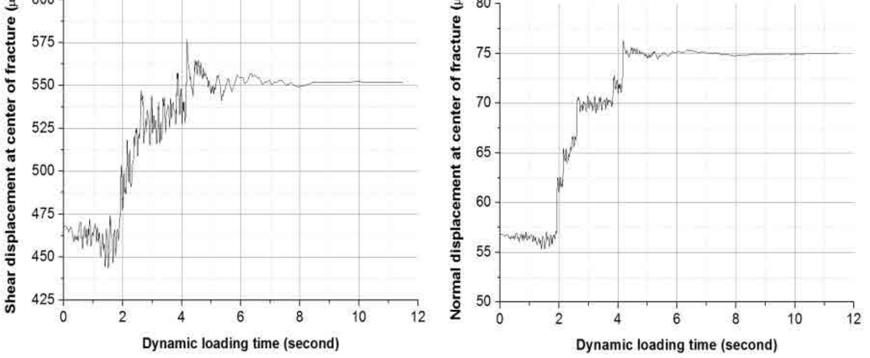

(a) (b)

Figure 99. (a) shear displacement and (b) normal displacement of single fracture when S-wave and P-wave are applied simultaneously. Compare the results presented in Figure 97 for the same model when only a P-wave is applied.

5.2.4. Independent modelling of the near-field and DFN for shear displacement and transmissivity evolution during an earthquake

In this Section, both shear and normal stress time histories are applied simultaneously to the NE02 and NW02 DFN models. Dynamic loading is applied for 11.5 seconds on the models at specific times of the thermo-mechanical and glacial loading calculation. Hence the effect of earthquake loading is superimposed on thermo-mechanical and glacial loadings. Two earthquake loading cases are computed in two vertical sections (EGEQ_NE02 and TGEQ_NW02).

5.2.4.1. NE section

Earthquake loading with both shear and normal stress time histories from synthetic ground motion (SKI, 1992) as shown in Figure 98 are applied to model TGEQ_NE02 at specific time of the thermo-mechanical and glacial analysis. Dynamic loadings are executed at five specific times (see Appendix 4): 100 years (which shows the maximum displacement), 12,000 years (T1), 38,000 years (T3), 55,000 years (T4) and 58,000 years (T5) as presented in Figure 86. These specific times are chosen because the possibility of shear failure is largest when the glacially induced vertical stress becomes maximum or zero. Fracture and intact rock properties used for this analysis are listed in Table 5.

In order to confirm that input stress waves propagate through the fractured block properly, shear and normal stresses and velocities in *x*- and *y*-direction are checked at the bottom boundary, in the center and upper boundary of the model.

Around 100 years after disposal of the canisters, the normal and shear displacement showed maximum values during thermal loading phase. For example, at a point in the model (coordinates 3.3 m,-462 m), which is located in the center of a fracture close to the excavation, the shear displacement did show a maximum value. Therefore, earthquake loading is applied to this fracture at this specific time at first. Figure 100 shows the fracture shear and normal displacement after earthquake loading. The magnitudes of the permanent shear and normal displacement fluctuations are very small with less than 1 μm displacement. For example, shear displacement at the point (3.3, -462) changes from 56.34 μm to 56.41 μm. Also, normal displacement at this point is almost same which is from 41.57 μm to 41.52 μm. These small changes indicate that shear displacement is mainly elastic and no shear failure has occurred at this specific fracture. This small change in fracture deformation is explained by the favorable fracture orientation against frictional failure, and relatively small size of the fractures. Furthermore, the selected friction angle of 35.8° is considered to be too high to induce failure with the additional dynamic shear stress in the range of about 1 MPa. Therefore, the dynamic analysis of the model with the specific DFN geometry considered shows that, the effect of earthquake on transmissivity change seems to be negligible.

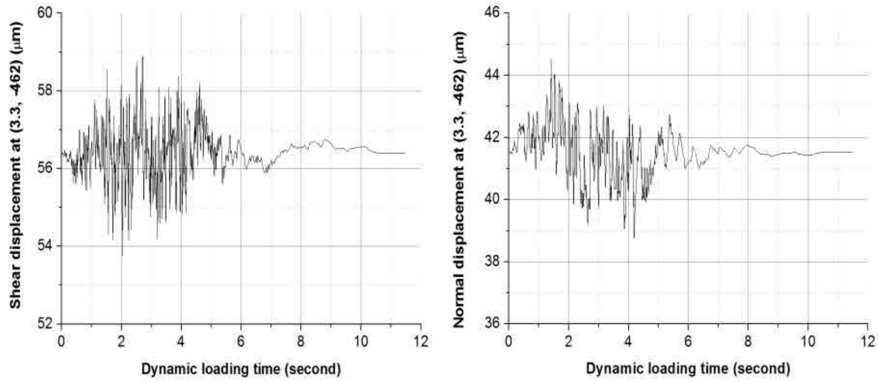

(a) (b)

Figure 100. Fracture displacement of model TGEQ_NE02 during dynamic loading at 100 years: (a) shear displacement and (b) normal displacement at point (2.53,-464).

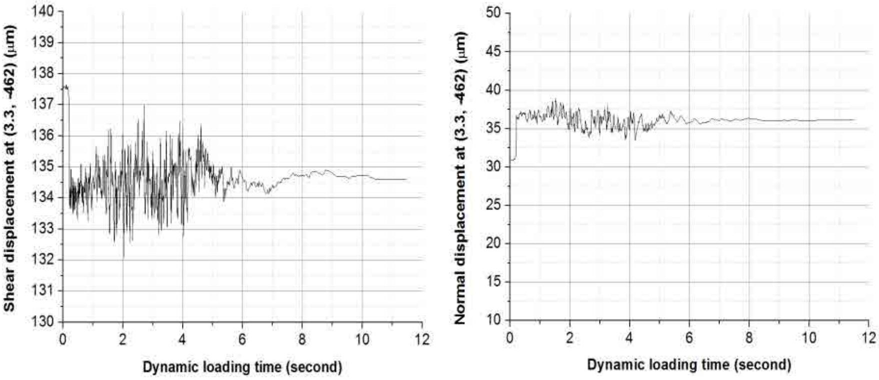

(a) (b)

Figure 101. Fracture displacement of model TGEQ_NE02 at point (3.3, -462) during dynamic loading after 12,000 years: (a) shear displacement, (b) normal displacement.

At 12,000 years after disposal of canister, the glacially induced stresses reach maximum during the first glacial cycle. The shear displacement is maximum at point (3.3,-462) close to the excavation zone as identical earthquake loading from S-, and P-waves are applied. Figure 99 represents shear and normal displacement of the fracture. Similar to the results of earthquake loading at 100 years, the displacements of the short fracture are insensitive to earthquake loading. However, the relatively larger magnitude of normal displacement comparing to previous results (loading at 100 years) indicates the stress distribution of the model is affecting the response to the earthquake loading. Shear displacement is changed from 137.5 μm to 134.6 μm, and normal displacement is increased from 30.95 μm to 36.11 μm.

5.2.4.2. NW section

A similar earthquake loading was applied to model (TGEQ_NW02) of the NW section at specific times 100 and 12,000 years after the thermo-mechanical and glacial analysis (Appendix 4). Figure 102 shows dynamic shear and normal displacements of the model. Both shear and normal displacement recover to the initial state, which means that displacement induced by earthquake is mainly elastic. The maximum shear displacement during dynamic loading is 171 μm. Figure 102 (b) shows the changes in normal displacement where initial and final displacement nearly same as from 32.17μm to 32.41 μm.

At 12,000 years after disposal of the canisters, the glacially induced stresses reach its maximum during the first glacial cycle. Compared to 100 years after start of deposition, when an earthquake loading from the S- and P-waves is applied smaller variations in displacement are obtained as shown in Figure 103. Although the range of shear displacement are around 2.5 μm, the permanent displacement was less than 1 μm, which is still negligible. For example, shear displacement of this point is changed from 649.5 μm to 649.3 μm. Additional results at specific times T3, T4, T5 for both models TGEQ_NE02 and TGEQ_NW02 are summarized in Appendix 4.

In conclusion, dynamic loading cannot reach the limit of plastic displacement because of low magnitude of dynamic stresses and unfavorable orientation of the fractures. Therefore, the effect of an earthquake on transmissivity change seems to be small. Small fracture sizes used in this study are in the range of 10 m and this

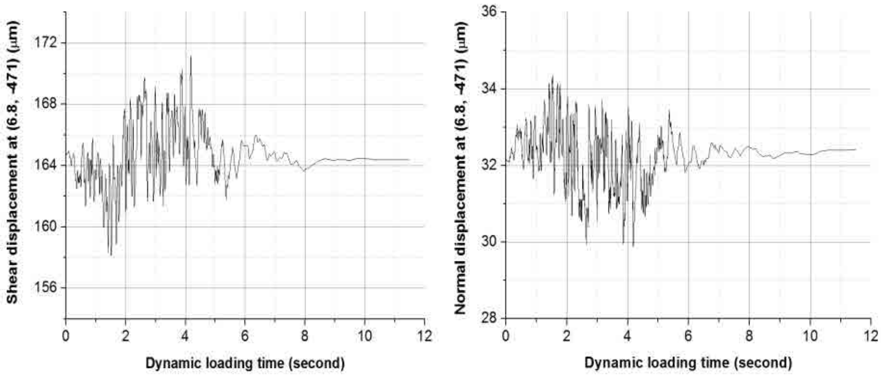

(a) (b)

Figure 102. Fracture displacement of model TGEQ_NW02 at point (6.8,-471) during dynamic loading at 100 years: (a) shear displacement and (b) normal displacement.

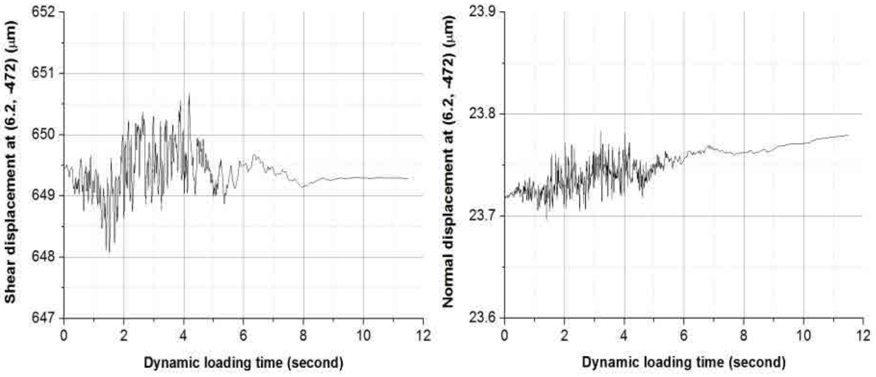

(a) (b)

Figure 103. Fracture displacement of model TGEQ_NW02 at point (6.2,-474) during dynamic loading at 12,000 years: (a) shear displacement and (b) normal displacement.

also affects the results. However, one cannot completely exclude the possibility of fracture dilation due to earthquake, especially when larger scale fractures are considered. Therefore, larger scale earthquake analysis may reveal the possibility of transmissivity change under earthquake loading. Historically, earthquake modelling has been conducted only in view of canister integrity, and more systematic analysis on the effect of earthquake on transmissivity is necessary.

5.3. The Consultants' assessment on the evolution of fracture transmissivity during an earthquake close to the repository

The Authors' findings from earthquake effects on fracture transmissivity change can be summarized as follows.

- Conceptual models containing a single fracture in the size of 5 m, 10 m and 15 m show that earthquake can induce large shear displacement followed by irreversible fracture dilation in the order of ca 20 μm based on synthetic ground motion velocity histories obtained in the literature and valid for construction of Swedish nuclear power plant (yearly probability 10^{-7}). This results show that the effect of earthquake is important not only in terms of canister integrity but also for possible effect on fracture hydraulic properties.
- Earthquake modelling on DFN models in the vicinity of tunnel and deposition hole revealed that the fracture shear and normal displacement are negligible with fracture normal displacement less than 1 μm. This would correspond to an earthquake of moment magnitude of about 4.2.

  The contrast between the results of the DFN models compared to the presented conceptual models is due to favorable fracture orientation in the DFNs, large friction angle of rocks in the Forsmark area and the small scale fractures considered in this near field study. Nonetheless, we cannot exclude the possibility that a modelling study with inclusion of large deformation zones may shed a different light on the earthquake induced transmissivity changes of large deformation zones and target fractures in the repository at Forsmark.
- A more systematic analysis with various fracture statistics and earthquake condition is necessary in order to fully investigate the effect of earthquake on fracture transmissivity change.

6. The Consultants' overall assessment on the evolution of fracture transmissivity

SKB conducted an innovative and thorough analysis of the transmissivity change of fractures around a deep geological repository at Forsmark during a time period of 100,000 years. The extensive work by SKB deserves considerable appreciation in many respects. Nonetheless, a more systematic investigation about the effect of shear dilation on transmissivity change should have been carried out. The result of the current review and modelling demonstrate the importance of considering the shear-driven transmissivity change of rock fractures. This review points out technical issues that were overlooked or underestimated by SKB. Results from our current modelling with the DEM-DFN methodology are used to support the arguments in the review of SKB's work. Table 8 compares the approaches taken by SKB and evaluates them in the light of the present review work.

The findings from this review can be summarized as follows:

- Fracture dilation angle obtained by SKB from direct shear tests was 14.6°, 7.7° and 3.2° for a normal stress of 0.5 MPa, 5 MPa and 20 MPa, respectively. These dilation angles can generate considerable shear dilation and related increase of normal displacement/mechanical aperture of the fractures. However, these data were not utilized for the safety assessment and were not discussed by SKB with respect to their implications for long-term safety of the KBS-3V repository.
- The magnitude of transmissivity change induced by shear dilation was considered negligible in SKB's studies for the license application. In fact, SKB did not conduct quantitative estimation of transmissivity change due to shear dilation. The current review shows that transmissivity increase due to shearing of the fracture during the thermal phase of the repository can be up to 2 orders of magnitude with an initial fracture aperture of 30 μm. Transmissivity increase by 3 and 4 orders of magnitude are valid for an initial aperture of 10 μm and 5 μm, respectively.
- SKB claims that the region that is vulnerable to transmissivity change was within 2 m from the periphery of deposition tunnels and holes. However, the current review and modelling show that large transmissivity changes (up to 2 orders of magnitude) can occur about 10 m from the deposition tunnel in a repository. We argue that a significant transmissivity increase is possible anywhere between adjacent deposition tunnels. This because of the significant stress ratio at Forsmark that might exceed the frictional strength of the fractures and give rise to significant dilation behavior under the thermal phase of the repository.
- The modelling results show that the increased transmissivity induced by shear dilation did not recover to its initial state after cooling of the repository and, therefore, the process of thermo-shearing is irreversible. SKB's investigation failed to capture this important phenomenon. It is emphasized that a permanent change of transmissivity can impact the long-term safety such as buffer resaturation time and radionuclide transport.

Table 8. Comparison of modelling approach taken by SKB and by authors on thermal and earthquake induced transmissivity change (ΔT).

Topic	SKB	The Authors' review	Comments
Geometry	3D with infinite through-going fractures	2D realistic DFNs on three orthogonal planes	2D DFN might underestimate connectivity
ΔT due to normal stress	• DEM (3DEC) and • indirect estimation of ΔT from stress-aperture relation	DEM (UDEC) with implemented linear stress-aperture relation	
ΔT due to shear stress	• DEM (3DEC) and • indirect estimation of shear displacement from displacement-shear vs. stress drop equation	DEM (UDEC) with implemented dilation equation and aperture change due to combined normal stress and shear stress	SKB did not calculate ΔT from shear dilation.
ΔT due to thermal loading	• Increase by a factor of 2 by normal stress during temperate phase • Shear induced change judged to be minor due to large normal stress • 2 order of magnitude increase only within 2 m from the tunnel	For a fracture size about 20 m: • 2 orders of magnitude increase with initial aperture of 30 μm • Over 4 orders of magnitude with initial aperture of 5 μm	• Dilation normal stresses between 5 MPa and 20 MPa is a critical factor • Larger fractures may have larger ΔT
	Areal extent of ΔT: Within 2 m from the tunnel. Negligible elsewhere	An order of magnitude change possible 10 m away from repository tunnels	
	Irreversible ΔT: Mostly fully reversed after 10,000 years	Shear dilation did not recover after 10,000 years	
ΔT due to dilation induced by glacial loading	Did not conduct this analysis	Explicit analysis was conducted. ΔT shown to be negligible because of isotropic glacial load	
ΔT due to dilation induced by an earthquake	Did not conduct this analysis	Explicit analysis was conducted. • Meaningful ΔT was demonstrated in conceptual model • ΔT in DFN model is negligible in near field	Modelling with larger fractures and deformation zones is needed.

- The connectivity of the bedrock below 150 m depth in Forsmark is very poor and only one out of ten DFN realizations showed sufficiently high connectivity around the deposition hole to perform block analyses with UDEC. However, it is noted that only a small fraction of the fractures are responsible for the overall fluid flow in the repository and a low connectivity models still resulted in considerable increase in transmissivity of fractures due to thermo-shearing.
- In the study of the far-field model, sub-horizontal zones were most prone to shear dilation induced by thermal loading. It is noted only the possibility of shear slip was investigated for the far-field model without estimation of possible range of transmissivity change. Improving the far-field modelling of shear-slip and transmissivity change will require substantial data about mechanical and hydraulic properties of deformation zones from Forsmark.
- Although SKB conducted relatively robust glaciation modelling considering two pore pressure models, more systematic analysis in terms of following aspect are required: 1) the role of shear dilation induced by up to 8 mm shear slip for a fracture 100 m long calculated in the SKB's own analysis; 2) the role of considering explicit fracture modelling based on realistic DFN geometry that will alter the stress distribution around the deposition tunnels and holes.
- Independent analysis and modelling were conducted for the glacial phase with explicit consideration of fractures from realistic DFN networks. The generated shear dilation in most of the glaciation phases was negligible because of the isotropic increase of glacial loading in the model. Furthermore, the change of transmissivity from glacial loading was recovered to its initial value indicating the fracture deformation is elastic.
- Conceptual models containing a single fracture in the size of 5 m, 10 m and 15 m show that earthquake can induce large shear displacement followed by irreversible fracture dilation in the order of ca 20 μm based on synthetic ground motion velocity histories obtained in the literature and valid for construction of Swedish nuclear power plant. This results show that the effect of earthquake could be important, not only in terms of canister integrity, but also for possible effect on fracture hydraulic properties.
- Earthquake modelling with the same synthetic ground motion velocity histories as valid for construction of Swedish nuclear power plant applied to DFN models in the vicinity of deposition tunnels and holes revealed that the fracture shear and normal displacement are negligible with fracture normal displacement less than 1 μm. This contrast in results as compared to the presented conceptual models is due to the more favorable fracture orientation, larger friction angle of fractures and interaction of the small scale fractures considered in this near-field study of the repository at Forsmark. Nonetheless, we cannot exclude the possibility that a modelling study with inclusion of large deformation zones may shed a different light on the earthquake induced transmissivity changes of large deformation zones and target fractures in the repository at Forsmark.
- A more systematic analysis with various fracture realizations and earthquake conditions is necessary in order to fully investigate the effect of earthquake on fracture transmissivity change.

The following aspects have to be considered in evaluating the significance of the current review and for further study:

- The current study was conducted based on 2D-DFN cuts from 3D-DFN from Forsmark. This process of cutting greatly reduced the connectivity of fractures. Therefore, the significance of transmissivity change shown in this study would probably become graver if a hydro-mechanical analysis on 3D-DFN was conducted. More quantitative study on the significance of two dimensional simplification is necessary.
- Possible variation of connectivity was investigated by increasing the fracture intensity P_{32} of the DFNs by 20%. As this increase is somewhat arbitrary, systematic sensitivity analysis can be undertaken for the complete understanding of the effect of fracture statistics including density, connectivity, orientation and lengths.
- Characterizing the hydraulic and mechanical behavior of rock fractures and deformation zones is a longstanding difficulty in Rock Mechanics and Hydrogeology. For example, it is not straight-forward to distinguish between mechanical and hydraulic apertures. There is no consensus in the scientific community with respect to how to scale measured dilation behavior at a centimeter scale in the laboratory to tens or hundreds of meter in the field. Given all these reservations and problems, one has to take a conservative approach when evaluating the possible range of magnitude and spatial extent of transmissivity change at a repository site.
- The current review and modelling of the effects of an earthquake was conducted focusing on the conceptual study with a single fracture surrounded by an elastic medium rock. A more systematic analysis considering the various effects in a dynamic analysis is yet to be conducted, e.g. effect of damping on the model, and more detailed mechanisms of fracture shear and normal deformation during cyclic dynamic loading. There seem to be a lack of supporting laboratory study in this regards.

7. Acknowledgements

Authors thank Ms Jungah Park, graduate student at Seoul National University, for her substantial contribution to the DEM analyses. We also want to extend our gratitude to Dr Joel Geier of Clearwater Hardrock Consulting, and Branko Damjanac of Itasca Consulting Group for their help in DFN construction and earthquake modelling, respectively. Finally, special thank goes to Dr Flavio Lanaro of the Swedish Radiation Safety Authority for his extensive involvement throughout the preparation of this report.

8. References

Alm P (1999). Hydro-mechanical behaviour of a pressurized single fracture: an in situ experiment. Ph.D. thesis. Chalmers University of Technology. Göteborg.

Backers T, Meier T, Gipper P, Stephansson O, 2014. Rock Mechanics - Assessing probability and extent of blind faults and fault-end growth around the KBS-3 repository at Forsmark – Main Review Phase, SSM Technical Note 2014:58, Swedish Radiation Safety Authority (SSM).

Barton N and Choubey V (1977). The shear strength of rock joints in theory and practice. Rock Mech Rock Eng, 10(1-2):1-54.

Bandis S, Lumsden A and Barton N (1981). Experimental studies of scale effects on the shear behaviour of rock joints, Int J Rock Mech Min Sci & Geomech Abst, 18(1): 1–21.

Barton N (1982). Modelling Rock Joint Behavior from In Situ Block Tests: Implications for Nuclear Waste Repository Design. Office of Nuclear Waste Isolation. Columbus, OH, 96p, ONWI-308, September 1982.

Bandis S, Lumsden A and Barton N (1983). Fundamentals of rock joint deformation, Int J Rock Mech Min Sci & Geomech Abst, 20(6):249–268.

Barton N, Bandis S and Bakhtar K (1985). Strength, deformation and conductivity coupling of rock joints, Int J Rock Mech Min Sci & Geomech Abstr, 22(3):121–140.

Barton CA, Zoback MD and Moos D (1995). Fluid-flow along potentially active faults in crystalline rock, Geology, 23(8):683-686.

Bhasin R and Kaynia A. M. (2004). Static and dynamic simulation of a 700-m high rock slope in western Norway. Engineering Geology, 71:213–226.

Byerlee J (1978). Friction of rocks. Pure Appl Geophys, 116:615-626.

Bödvarsson R, Lund B, Roberts R, Slunga R (2006). Earthquake activity in Sweden – Study in connection with a proposed nuclear waste repository in Forsmark or Oskarshamn. SKB R-06-67, Swedish Nuclear Fuel and Waste Management Co (SKB).

Cappa F, Guglielmi Y, Rutqvist J, Tsang C-F and Thorval A (2006). Hydromechanical modeling of pulse tests that measure fluid pressure and fracture normal displacement at the Coaraze Laboratory site, France, Int J Rock Mech Min Sci, 43(7):1062–1082.

Chen Z, Narayan SP, Yang Z and Rahman SS (2000). An experimental investigation of hydraulic behaviour of fractures and joints in granitic rock, Int J Rock Mech Min Sci, 37:1061–1071.

Damjanac B, Fairhusrt C, Brandshaug T (1999). Numerical simulation of the effects of heating on the permeability of a jointed rock mass, Itasca Consulting Group Incorporated, Minneapolis, USA.

Esaki T, Du S, Mitani Y, Ikusad K and Jing L (1999). Development of a shear-flow test apparatus and determination of coupled properties for a single rock joint, Int J Rock Mech Min Sci, 36:641–650.

Follin S, Levén J, Hartley L, Jackson P, Yoyce S, Roberts D and Swift B (2007). Hydrogeological characterisation and modelling of deformation zones and fracture domains, Forsmark modeling stage 2.2, SKB R-07-48, Swedish Nuclear Fuel and Waste Management Co (SKB).

Fox A, La Pointe P, Hermanson J and Öhman, J (2007). Statistical geological discrete fracture network model. Forsmark modelling stage 2.2. SKB R-07-46 Swedish Nuclear Fuel and Waste Management Co (SKB).

Fransson Å (2009). Literature survey: Relations between stress change, deformation and transmissivity for fractures and deformation zones based on *in situ* investigations. SKB R-09-13, Swedish Nuclear Fuel and Waste Management Co (SKB).

Fälth B and Hökmark H (2006). Seismically induced slip on rock fractures – Results from dynamic discrete fracture modeling, SKB TR-06-48, Swedish Nuclear Fuel and Waste Management Co (SKB).

Fälth B, Hökmark H and Munier R (2010). Effects of large earthquakes on a KBS-3 repository. Evaluation of modeling results and their implications for layout and design. SKB TR-08-11, Swedish Nuclear Fuel and Waste Management Co (SKB).

Fälth B and Hökmark H (2011). Modelling end-glacial earthquakes at Olkiluoto. Working Report 2011-13, Posiva Oy, Eurajoki, Finland.

Glamheden R, Fredriksson A, Röshoff K, Karlsson J, Hakami H and Christiansson R (2007), Rock Mechanics Forsmark. Site descriptive modelling Forsmark stage 2.2. SKB R-07-31, Swedish Nuclear Fuel and Waste Management Co (SKB).

Guglielmi Y, Cappa F, Rutqvist J, Tsang C-F and Thoraval A (2008a). Mesoscale characterization of coupled hydromechanical behavior of a fractured-porous slope in response to free water-surface movement, Int J Rock Mech Min Sci, 45(6): 862–878.

Guglielmi Y, Cappa F, Virieux J, Rutqvist J, Tsang C-F and Thoraval A (2008b). A new in situ approach for hydromechanical characterization of mesoscale fractures: the High-Pulse Poroelasticity Protocol (HPPP), 42nd US Rock Mechanics Symposium and 2nd U.S.-Canada Rock Mechanics Symposium.

Gustav H and Arbin D (2011). Renewed safety assessment of the resistance against certain events – The Stress Test, Vattenfall, FT-2011–3787.

Heuze' F.E., Walton O.R., Maddix D.M., Shaffer R.J. and Butkovich T.R. (1990). Analysis of explosion in hard rocks: the power of the discrete element modelling. In: Rossmanith, H.P. (Ed.), Mechanics of jointed and faulted rock. Proc. Int. Conf. Vienna Balkema, Rotterdam, 21–28.

Homand F, Belem T and Souley M (2001). Friction and degradation of rock joint surfaces under shear loads, Int J Numer Anal Meth Geomech, 25:973–999.

Hökmark H, Fälth B and Wallroth T (2006). T-H-M couplings in rock – overview of results of importance to the SR-Can safety assessment, SKB R-06-88, Swedish Nuclear Fuel and Waste Management Co (SKB).

Hökmark H, Lönnqvist M, Kristensson O, Sundberg J and Hellström G (2009). Strategy for thermal dimensioning of the final repository for spent nuclear fuel. SKB R-09-04, Swedish Nuclear Fuel and Waste Management Co (SKB).

Hökmark H, Lönnqvist M and Fälth B (2010). THM-issues in repository rock – Thermal, mechanical, thermo-mechanical and hydro-mechanical evolution of the rock at the Forsmark and Laxemar sites, SKB TR-10-23, Swedish Nuclear Fuel and Waste Management Co (SKB).

Huang TH, Chang CS and Chao CY (2002). Experimental and mathematical modeling for fracture of rock joint with regular asperities, Eng Fract Mech, 69: 1977–1996.

Itasca Consulting Group (2011). OPG's deep geologic repository for low & intermediate level waste, Long-term geomechanical stability analysis, NWMO DGR-TR-2011-17

Itasca Consulting Group (2014). Universal distinct element code (UDEC 6.0) manual, Minneapolis, Minnesota.

Koyama T, Fardin N, Jing L and Stephansson O (2006). Numerical simulation of shear-induced flow anisotropy and scale-dependent aperture and transmissivity evolution of rock fracture replicas, Int J Rock Mech Min Sci, 43: 89–106.

Lee HS (1999). A study for the mechanical and hydraulic behavior of rock joints under cyclic shear loading, Ph.D. Thesis, Department of Mineral and Petroleum Engineering, Seoul National University, Republic of Korea.

Lee JW, Min KB and Stephansson O (2013). Probabilistic Analysis of fracture reactivation associated with deep underground CO2 injection, Rock Mech Rock Engng, 46:801-820.

Leonard M (2010), Earthquake fault scaling: Self-consistent relating of rupture length, width, average displacement, and moment release, Bull Seismol Soc Am, 100(5A):1971-1988.

Liu HH, Rutqvist J, Zhou Q and Böðvarsson GS (2003). Upscaling of normal stress-permeability relationships for fracture networks obeying fractional Levy motion, In GeoProc 2003 International Conference on Coupled T-H-M-C processes in Geo-systems: Fundamentals, Modelling, Experiments & Applications.

Martin CD, Davison CC and Kozak ET (1990). Characterizing normal stiffness and hydraulic conductivity of a major shear zone in granite, Rock joints (Barton & Stephansson, eds), Balkema, Rotterdam, Netherlands.

Min KB, Rutqvist J, Tsang CF and Jing L (2004). Stress-dependent permeability of fractured rock masses: a numerical study, Int J Rock Mech Min Sci, 41(7):1191-1210.

Min KB and Stephansson O (2009). Shear-induced fracture slip and permeability change – Implications for long-term performance of a deep geological repository, SSM 2009:08, ISSN:2000-0456.

Min KB and Stephansson O (2012). Rock Mechanics related to long-term repository and site evolution, SSM Technical Note 2012:51, Swedish Radiation Safety Authority (SSM).

Min KB, Lee J and Stephansson O (2013). Implications of thermally-induced fracture slip and permeability change on the long-term performance of a deep geological repository, Int J Rock Mech Min Sci 61:175-288.

Olsson R (1998). Mechanical and hydromechanical behaviour of hard rock joints, A laboratory study, Ph.D. Thesis, Department of Geotechnical Engineering, Chalmers University of Technology, Sweden.

Olsson R and Barton N (2001). An improved model for hydromechanical coupling during shearing of rock joints, Int J Rock Mech Min Sci, 38: 317–329.

Pal S, Kaynia A. M., Bhasin R and Paul D. K. (2012). Earthquake stability analysis of rock slopes: a case study. Rock Mech Rock Eng, 45: 205–215.

Park JW and Song JJ (2009). Numerical simulation of a direct shear test on a rock joint using a bonded-particle model, Int J Rock Mech Min Sci, 46(8):1315-1328.

Pollard DD and Segall P (1987). Theoretical displacements and stresses near fractures in rock: with application to faults. Fracture Mechanics of Rock. Academic Press Inc, London, 277-349.

Rhén I, Forsmark T, Hartley L, Jackson P, Roberts D, Swan D and Gylling B (2008). Hydrogeological conceptualisation and parameterisation, Site descriptive modelling SDM–Site Laxemar, SKB R-08-78, Swedish Nuclear Fuel and Waste Management Co (SKB).

Rosengren L and Stephansson O (1993). Modelling of rock mass response to glaciation at Finnsjön, Central Sweden, Tunnelling and Underground Space Technology, 8(1), 75–82.

Rutqvist J, Noorishad J, Tsang C-F and Stephansson O (1998). Determination of fracture storativity in hard rocks using high-pressure injection testing, Water Resour Res, 34(10):2551–2560.

SKB (2009). Site engineering report Forsmark. Guidelines for underground design Step D2. SKB R-08-83, Swedish Nuclear Fuel and Waste Management Co (SKB).

SKB, (2010). Data report for the safety assessment SR-Site. SKB TR-10-52, Swedish Nuclear Fuel and Waste Management Co (SKB).

SKB (2011). Long-term safety for the final repository for spent nuclear fuel at Forsmark. Main report of the SR-Site project. SKB TR-11-01, Swedish Nuclear Fuel and Waste Management Co (SKB).

SKB (2012). Forsmark site investigation – Study of seismic background signals in the Forsmark area. SKB P-12-08, Swedish Nuclear Fuel and Waste Management Co (SKB).

SKI, 1992. Characterization of seismic ground motions for probabilistic safety analyses of nuclear facilities in Sweden, Project Seismic Safety, SKI Technical Report 92:3, Swedish Nuclear Power Inspectorate (SKI).

SSM (2011). European stress tests for nuclear power plants, The Swedish National Report, Doc. No. 11–1471, Swedish Radiation Safety Authority (SSM).

Stephens MB, Fox A, La Pointe P, Simenov A, Isaksson H, Hermanson J and Öhman J (2007). Geology Forsmark – site descriptive modelling Forsmark stage 2.2, SKB R-07-45, Swedish Nuclear Fuel and Waste Management Co (SKB).

Wibowo J (1994). Effect of Boundary Conditions and Surface Damage on the Shear Behavior of Rock Joints: Tests and Analytical Predictions. University of Colorado at Boulder, Boulder, CO. 200 pp.

Willis-Richards J, Watanabe K and Takahashi H (1996). Progress toward a stochastic rock mechanics model of engineered geothermal systems, Journal of Geophysical Research, 101:17481–17496.

Yeo IW, de Freitas MH and Zimmerman RW (1998). Effect of shear displacement on the aperture and permeability of a rock fracture, Int J Rock Mech Min Sci, 35(8):1051-1070.

APPENDIX 1

Coverage of SKB reports

Table A1-1: Coverage of SKB reports reviewed by the Authors.

Reviewed report	Reviewed sections	Comments
SKB TR-08-11 Effect of large earthquakes on a KBS-3 repository. Evaluation of modelling results and their implications for layout and design	Entire report	[There is no direct quantitative assessment of transmissivity change due to shearing and earthquake]
SKB TR-08-11	[1.2.1] p.16-17	[It was stated that the seismic impact on the transport properties is not an issue for the safety assessment and change of hydraulic system is related only with the canister damage. However, it is noted that fracture transmissivity change can be meaningful even the shear slip is not large enough to cause canister damage.]
SKB TR-10-23 THM-issues in repository rock – thermal, mechanical, thermo-mechanical and hydro-mechanical evolution of the rock at the Forsmark and Laxemar sites	Entire report	[There is no direct quantitative assessment of transmissivity change due to shearing although necessary information such as dilation angle (determined by direct shear test on 57 samples) was available.]
SKB TR-10-23	[4.7.2] p.42.	[Fig.4-9 showed the normal stress-transmissivity model. Similar model needs to be considered with respect to shear stress]
SKB TR-10-23	[5.8.2] p.89-90.	[Shear displacements were calculated in various scanlines. However, there was no information about transmissivity change.]
SKB TR-10-23	[6.8.2] Figure 6-27, p.89.	[Shear displacements at 450 m were recovered at 10,000 years. As shear displacement due to Coulomb slip is not reversible process this process does not seem to make physical sense.]
SKB TR-10-23	[1.2] p.11	[It was concluded that quantifying the hydraulic change in host rock as a response to earthquake is neither meaningful nor necessary. However, there is no quantitative

		explanation on this.]
SKB TR-06-88 T-H-M couplings in rock. Overview of results of importance to the SR-Can safety assessment.	[5.3] p.45	[The fracture dilation angle was set at 10 degrees as suggested by /Olsson 1998/ (cf. Figure 4‑6). How was this dilation angle incorporated into the numerical calculation? What would be the significance of having this value?]
SKB R-09-13 Literature survey: relations between stress change, deformation and transmissivity for fractures and deformation zones based on in situ investigations	Entire report	A good overview of fracture stress, deformability, and transmissivity

APPENDIX 2

Description of the Discrete Fracture Network used in this study

Based on a note by Joel Geier (Clearwater Hardrock Consulting)

The discrete-fracture network (DFN) approach is based on a conceptual model in which fractures are considered to be representable as a set of planar discontinuities, which can be characterized in terms of statistical distributions for their geometrical attributes. A wide variety of DFN conceptual models have been proposed in the scientific literature. The DFN models used in the present study follow SKB's approach (Fox et al., 2007, SB R-07-46) which makes use of DFN models consisting of disc-shaped fractures as proposed by Baecher et al. (1977), and characterized in terms of independent statistical distributions for the following fracture properties:

- Size (disc radius)
- Orientation (normal or pole vector)
- Transmissivity

Fracture centers are located randomly according to a Poisson process in 3-D space. The intensity of fracturing is characterized in terms of the total fracture area per unit volume, P_{32}, as defined by Dershowitz and Herda (1992).
Statistical models of this basic form are developed for each of several fracture sets in a given fracture domain. A fracture domain, by SKB's nomenclature, is considered to be a 3-D region of the rock within which the fracturing is homogeneous, in a statistical sense. A fracture set is generally defined (in the scientific literature) to be a set of fractures that have similar properties in terms of geometry as well as geological characteristics, but the fracture sets used in SKB's models are defined primarily based on fracture orientation. Fracture size (disc radius) in SKB's models is described by a power-law (Pareto) distribution, which is parameterized by an exponent k_r and a minimum radius r_0. Fracture orientation is described in terms of a Fisher distribution for fracture pole vectors, which is parameterized by the trend and plunge of a mean pole vector, and a parameter κ which is inversely related to the dispersion of fracture poles about the mean pole. Within a given fracture set, size and orientation are assumed to be statistically independent.
SKB's models are considered to apply for fractures (possibly including minor deformation zones as well as single, discrete fractures) with a length scale smaller than 1 km. In terms of disc-shaped fractures, a 1 km x 1 km square fracture has approximately the same surface area as a disc-shaped fracture of radius 564.2 m, so this is used as the upper bound for simulating values of fracture radius.
Fracture intensity (P_{32}) has been assessed by SKB mainly on the basis of the frequency of fractures in core-drilled holes. For the rock volume at repository depth, the main source of data is drill holes that are close to vertical, which implies good sampling of fractures that are close to horizontal, but poor sampling of fractures that

are close to vertical. Theoretical corrections for this sampling bias have been applied by SKB to produce estimates of the volumetric measure of fracture intensity, P_{32}. However, for fractures that are close to vertical, these corrections are sensitive to the geometrical assumptions that are implicit to the theoretical corrections (e.g. planar rather than undulating fractures, and equidimensional rather than elongated fractures).For the subset of fractures that conduct water, estimates of P_{32} by SKB have been derived by calibration of a DFN flow model based on flowmeter logging data. For the present simulations, these estimates of "conductive" P_{32} are represented by the "hydro [geological]" fracture sets based on data from Selroos and Follin (2009), with the remaining P_{32} assigned to fracture sets which are assumed to be "tight," with minimal fracture transmissivity.

For the present study, stochastic realizations of the DFN model are generated by simulation, using a different seed value for the random number generator to produce each realization. Parameters for the fracture sets are taken directly from SKB's GeoDFN model for Fracture Domain FFM01 (r_0-fixed variant) as given by Munier (2010, SKB TR 10-21, Appendix 3, Table A3.1). The derivation of this model by SKB is described in detail by Fox et al. (2007). Fracture orientation statistics (trend and plunge of the mean pole vector, and Fisher concentration parameter κ) are obtained by fitting to data for fracture orientations measured in core-drilled holes, using the hard-sector method of the FracMan code as described by Dershowitz et al. (2004).

For hydrogeomechanical modelling, an initial value of transmissivity for fractures could be required. SKB's Geo-DFN model does not specify transmissivities. Transmissivity distributions are specified for the fracture sets in SKB's Hydro-DFN model. The Hydro-DFN sets are here treated as subsets of the corresponding Geo-DFN sets, representing only a fraction of the fracture intensity (P_{32}) of the Geo-DFN sets.

Fracture sets labeled as "hydro" in Table 1 represent the subsets of the respective sets that are considered to have non-negligible transmissivity in SKB's Hydro-DFN model. The remaining fractions of these sets are labelled as "tight." SKB's definition of the Geo-DFN model does not include hydrogeological parameterization (fracture transmissivity, etc.). For all of the sets labeled as "hydro" in Table A2-1, transmissivity is related to fracture radius according to the "semi-correlated" model for the corresponding fracture set in the Hydro-DFN model (SKB R-09-22 Table 2-2 of Selroos and Follin, 2009), for the case of z < -400 m. The semi correlated model for transmissivity T vs. fracture radius r is defined as:

$$T = \exp[\log \bar{y} + b \log r + \sigma N] = \bar{y} r^b 10^{\sigma_{10} N} \qquad \text{Eq. (A.1)}$$

where $b, \bar{y}$, and σ_{10} are correlation parameters representing the logarithmic slope, the intercept value, and scatter about the fitted logarithmic trend, respectively, N is the truncated normal distribution $N(0,1)$ on the interval [-2,2], $\sigma = \sigma_{10}\log(10)$, and log denotes the natural logarithm.

The fracture realizations and extraction of 2-D datasets for the hydrogeomechanical simulations are carried out in a single Linux C-shell script for each calculation case, in the following steps for each realization:

1. Generation of the fracture realization.

2. Conversion of the resulting (thinned) set of hexagonal fractures to disks (not used directly for the production of these datasets, but used to simplify checks of the statistical properties of the fracture population);
3. Identification of fractures that cross a vertical plane striking N35W, using the DFM module dfmslice v. 2.4.1.1.
4. Identification of fractures that cross a vertical plane striking N55E, using the DFM module dfmslice v. 2.4.1.1.
5. Identification of fractures that cross a horizontal plane at z = -468 m and extraction fracture traces on that plane, using the DFM module dfmslice v. 2.4.1.1.
6. Further processing of the 2-D cross-section data to the format requested by SNU.

For the r0-fixed base case these steps are carried out by the following Linux C-shell script:

run fracgen batch v2

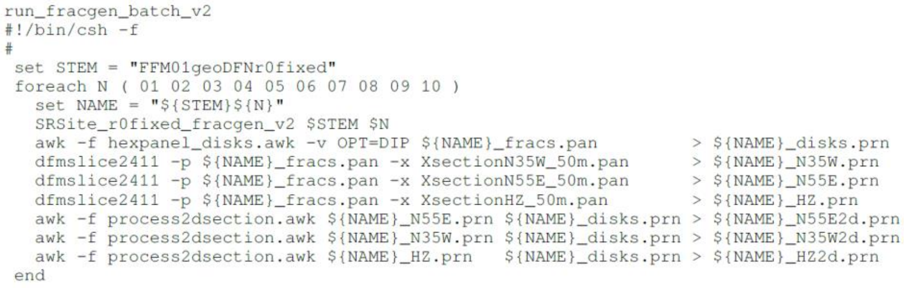

```
run_fracgen_batch_v2
#!/bin/csh -f
#
 set STEM = "FFM01geoDFNr0fixed"
 foreach N ( 01 02 03 04 05 06 07 08 09 10 )
   set NAME = "${STEM}${N}"
   SRSite_r0fixed_fracgen_v2 $STEM $N
   awk -f hexpanel_disks.awk -v OPT=DIP ${NAME}_fracs.pan         > ${NAME}_disks.prn
   dfmslice2411 -p ${NAME}_fracs.pan -x XsectionN35W_50m.pan      > ${NAME}_N35W.prn
   dfmslice2411 -p ${NAME}_fracs.pan -x XsectionN55E_50m.pan      > ${NAME}_N55E.prn
   dfmslice2411 -p ${NAME}_fracs.pan -x XsectionHZ_50m.pan        > ${NAME}_HZ.prn
   awk -f process2dsection.awk ${NAME}_N55E.prn ${NAME}_disks.prn > ${NAME}_N55E2d.prn
   awk -f process2dsection.awk ${NAME}_N35W.prn ${NAME}_disks.prn > ${NAME}_N35W2d.prn
   awk -f process2dsection.awk ${NAME}_HZ.prn   ${NAME}_disks.prn > ${NAME}_HZ2d.prn
 end
```

For the r0-fixed case with elevated P32 these steps are carried out by a similar script:

run fracgen batch Pelev v2

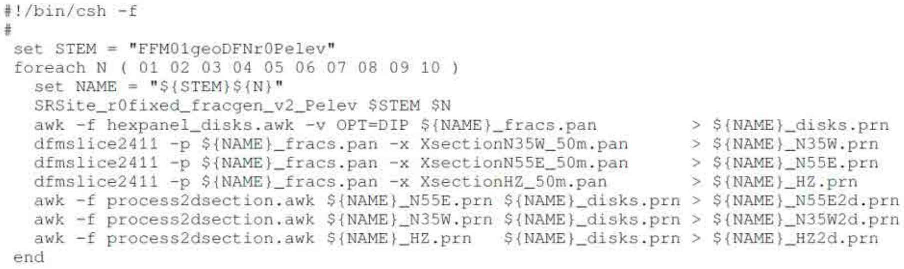

```
#!/bin/csh -f
#
 set STEM = "FFM01geoDFNr0Pelev"
 foreach N ( 01 02 03 04 05 06 07 08 09 10 )
   set NAME = "${STEM}${N}"
   SRSite_r0fixed_fracgen_v2_Pelev $STEM $N
   awk -f hexpanel_disks.awk -v OPT=DIP ${NAME}_fracs.pan         > ${NAME}_disks.prn
   dfmslice2411 -p ${NAME}_fracs.pan -x XsectionN35W_50m.pan      > ${NAME}_N35W.prn
   dfmslice2411 -p ${NAME}_fracs.pan -x XsectionN55E_50m.pan      > ${NAME}_N55E.prn
   dfmslice2411 -p ${NAME}_fracs.pan -x XsectionHZ_50m.pan        > ${NAME}_HZ.prn
   awk -f process2dsection.awk ${NAME}_N55E.prn ${NAME}_disks.prn > ${NAME}_N55E2d.prn
   awk -f process2dsection.awk ${NAME}_N35W.prn ${NAME}_disks.prn > ${NAME}_N35W2d.prn
   awk -f process2dsection.awk ${NAME}_HZ.prn   ${NAME}_disks.prn > ${NAME}_HZ2d.prn
 end
```

The source files for these calculations are contained in the directory:
        ~/Desktop/modelling/GeoDFNsimulations
An auxiliary directory with identical setup:
        ~/Desktop/modelling/GeoDFNsimulations2
was used to run some of the realizations for the elevated P_{32} case in parallel.

Table A2-1. Geometric parameters for generation of fracture sets for the r0-fixed base case for the Geo-DFN simulations for hydrogeomechanical modelling. Note that the specified maximum radius r_{max} is larger than an effective value which is a function of limited resolution of the simulation algorithm and the specified value of the minimum radiusr_{min}, as discussed later in this memorandum.

FFM01	Mean pole trend (°)	Mean pole plunge (°)	Fisher concentration κ	r_0	k_r	P_{32} (m^2/m^3) (unscaled)	r_{min} (m)	r_{max} (m)
NE global (hydro)	314.9	1.3	20.94	0.039	2.72	0.193	0.3	564.2
NS global (hydro)	270.1	5.3	21.34	0.039	2.75	0.122	0.3	564.2
NW global (hydro)	230.1	4.6	15.70	0.039	2.61	0.100	0.3	564.2
SH global (hydro)	0.8	87.3	17.42	0.039	2.58	0.158	0.3	564.2
EW local (hydro)	0.4	11.9	13.89	0.039	2.93	0.105	0.3	564.2
NE global (tight)	314.9	1.3	20.94	0.039	2.72	1.540	0.3	564.2
NS global (tight)	270.1	5.3	21.34	0.039	2.75	1.170	0.3	564.2
NW global (tight)	230.1	4.6	15.70	0.039	2.61	0.848	0.3	564.2
SH global (tight)	0.8	87.3	17.42	0.039	2.58	0.466	0.3	564.2
ENE local	157.5	3.1	34.11	0.039	2.97	0.256	0.3	564.2
EW local (tight)	0.4	11.9	13.89	0.039	2.93	0.064	0.3	564.2
NNE local	293.8	0.0	21.79	0.039	3.00	0.658	0.3	564.2
SH2 local	164.0	52.6	35.43	0.039	2.61	0.081	0.3	564.2
SH3 local	337.9	52.9	17.08	0.039	2.61	0.067	0.3	564.2

The values of the correlation parameters used for the “hydro” sets in this data delivery are:

b = 0.5
$\bar{y} = 5.3e^{-11}\ m^2/s$
$\sigma_{10} = 1.0$

For the other fracture sets (those not labeled as “hydro” in Table 1), the fracture transmissivity is set to an arbitrary low, constant value:

$T = 10^{-13}\ m^2/s$

In order to consider the variability of connectivity, fracture intensity (P_{32}) has been increased by 20% for all fracture sets. This increase is justified based on the recommendation of Fox et al. (2007) to consider P_{32}

As a stochastic variable, distributed as a gamma distribution. Fox et al. (2007, SKB R-07-46) suggested a gamma distribution as a model for variability in P_{32} for the GeoDFN (on a 30 m scale for most fracture sets).

The quantiles of the gamma distribution with shape parameter α and scale parameter β can be calculated by solving:

$$P(\alpha, P_{32}/\beta) = p \qquad \text{Eq. (A.2)}$$

In terms of P_{32} for a given quantile p, and where $P(\alpha, x)$ is the normalized incomplete gamma function $\gamma(\alpha, x))/\Gamma(\alpha)$.
For fracture domain FFM01, using 60th percentile values for each fracture set results in an 18% increase in total P_{32} compared with the median (50%) values. Thus (using round values), a 20% increase in total P_{32} is a reasonable variation to consider.

Quality Check 1: Comparison of expected and simulated P_{32} fracture intensity as a function of fracture radius

This quality check is based on the increments ofP_{32}, the fracture intensity per unit volume, for a given range of fracture radii [r1, r2]. For brevity these increments are referred to as P_{32} [r1, r2]. It may be noted that the overall fracture intensity P_{32} [0, ∞] is obtained as a particular case.

The DFN realizations for these calculation cases use selective thinning of fractures outside of sphere of 44 m radius of (0, 0, -468 m), which is the center the 50 m cubical region for which results are provided, bounded by (-25 m ,-25 m,-493 m) and (25 m, 25 m, -443 m). The 44 m radius is chosen to be slightly larger than the diagonal distance from the center of the cube to its corners:

$$\sqrt{3} \cdot 25\text{m} \approx 43.3\text{m}$$

Outside of this sphere, smaller fractures are deleted as a function of fracture radius, in order to minimize the number of fractures to be stored, while ensuring that all fractures within the 50 m cubical region are preserved. Therefore the check of P_{32} [r1, r2] is based only on the volume within this 50 m cube.

The results for realizations 01-04 of the r0-fixed base case are plotted in Figure A2-1 and A2-2, and for the realizations 01-04 of the elevated-P_{32} variant in Figure A2-3 and A2-4. In each figure, the top graph shows the expected distribution while the lower two graphs give the simulated results. The bars represent P_{32}[r1, r2] for increments of a quarter order of magnitude in fracture (equivalent) radius. Note that fractures of r < 0.3 m have been omitted from the stochastic realizations, so only fractures in size ranges beginning with (10-0.25 m , 1 m) ≈ (0.56 m, 1 m) are shown for comparison.

For the fracture sets that are divided into “hydro” and “tight” subsets, the theoretical distribution has been plotted only for the combination of these subsets. This way the same theoretical distribution as calculated for the Geo-DFN model used in other geomechanical calculations can be used. In the plots of simulated data, a lighter shade of the same color is used to distinguish the “tight” subset vs. the “hydro” subset.

It can be seen that there is visually very good agreement both in terms of total fracture intensity and the fracture intensity for individual fracture sets. The exceptions are (1) for size ranges with approaching the dimension of the 50 m cube, where stochastic effects due to the large impact of individual fractures on the increments of P_{32} are apparent, and (2) for size ranges with r larger than 56.2 m, for which no fractures occur in these realizations.

Table 2 gives the numerical values of simulated P_{32} for each of the fracture radius ranges larger thanr_{min}, compared with the theoretical values of P_{32} for the same ranges. It can be seen that the average total simulated P_{32} (the average of the sum over all fracture sets) is slightly higher than the theoretical value for all of the size ranges except for the ranges 10 m to 17.8 m and 17.8 m to 31.6m. However the average total simulated P_{32} is within one standard deviation of the theoretical value, for all except the smallest size ranges (fracture radius less than 3.16 m).

a) Theoretical distribution

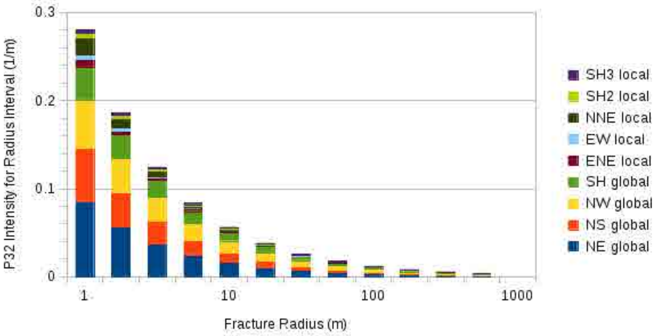

b) Simulated distribution (Realization 01)

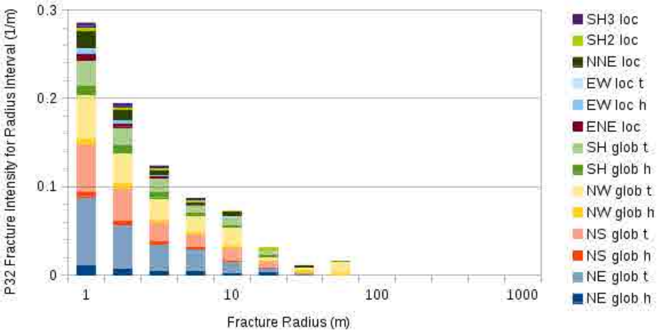

c) Simulated distribution (Realization 02)

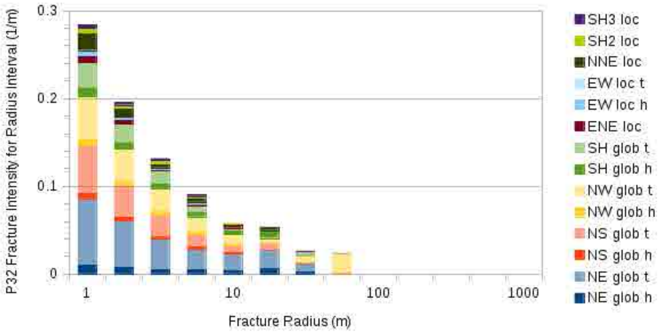

Figure A2-1. Comparison of theoretical and simulated increments of P_{32} fracture intensity for each of the fracture sets in the r0-fixed base case, for realizations 01 and 02. Abbreviations in the legend are: glob = global, loc = local, h = hydro, and t = tight. Each histogram bar represents ¼ order of magnitude range of fracture radius, and is labeled based on the maximum radius in the interval.

a) Theoretical distribution

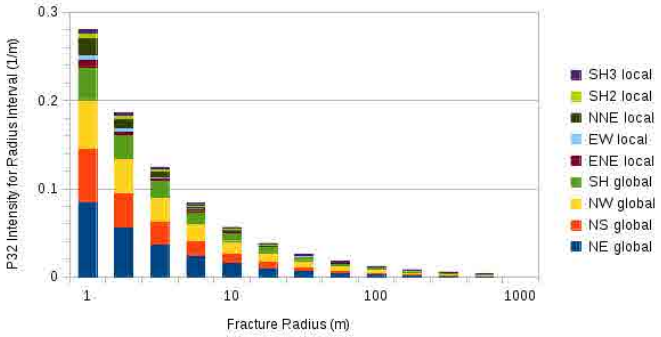

b) Simulated distribution (Realization 03)

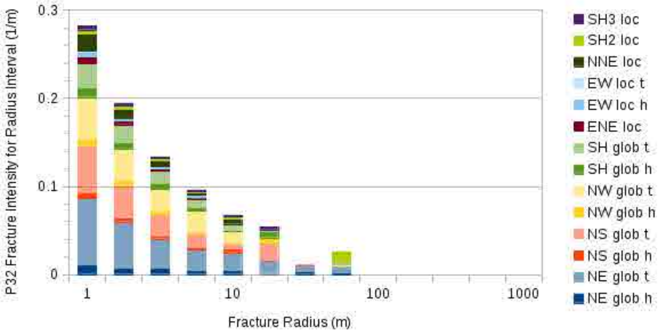

c) Simulated distribution (Realization 04)

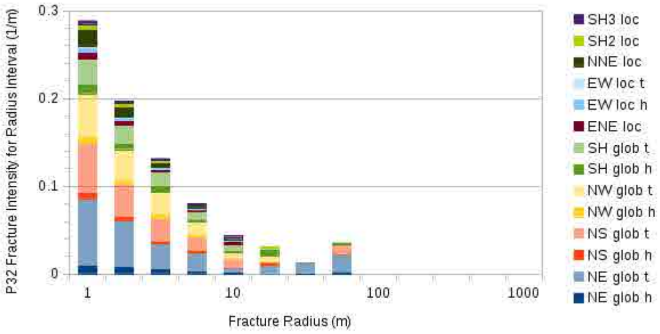

Figure A2-2. Comparison of theoretical and simulated increments of P_{32} fracture intensity for each of the fracture sets in the r0-fixed base case, for realizations 03 and 04. Abbreviations in the legend are: glob = global, loc = local, h = hydro, and t = tight. Each histogram bar represents ¼ order of magnitude range of fracture radius, and is labeled based on the maximum radius in the interval.

a) Theoretical distribution

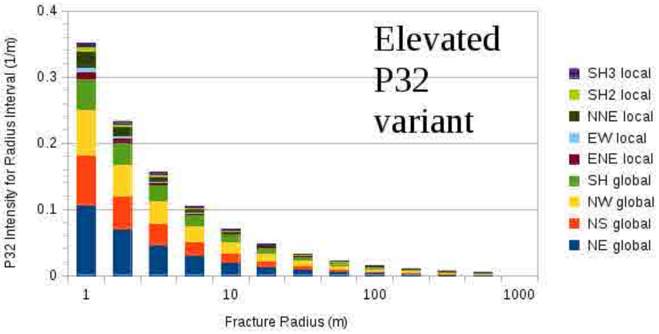

b) Simulated distribution (Realization 01)

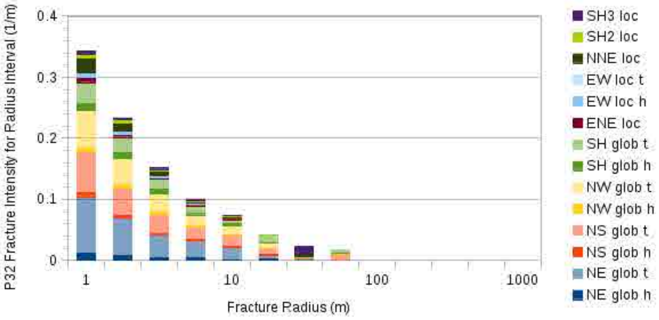

c) Simulated distribution (Realization 02)

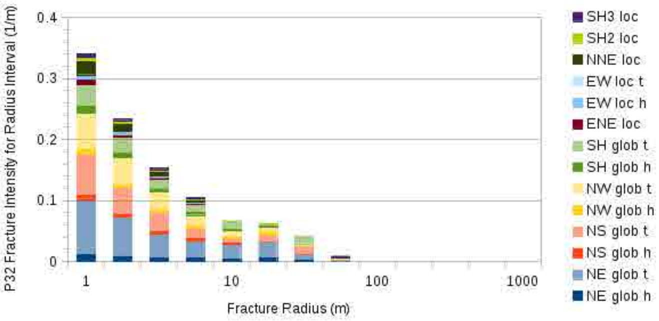

Figure A2-3. Comparison of theoretical and simulated increments of P_{32} fracture intensity for each of the fracture sets in the elevated-P_{32} variant of the r0-fixed model, for realizations 01 and 02. Abbreviations in the legend are: glob = global, loc = local, h = hydro, and t =tight. Each histogram bar represents ¼ order of magnitude range of fracture radius, and is labeled based on the maximum radius in the interval.

a) Theoretical distribution

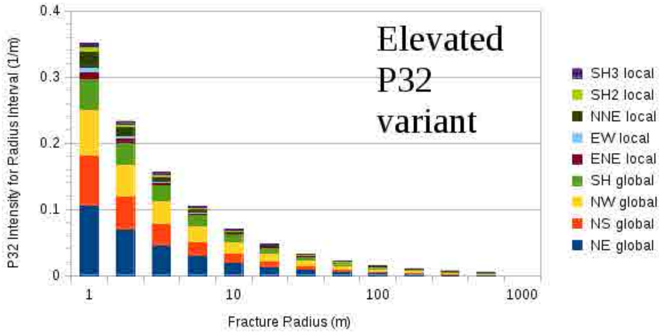

b) Simulated distribution (Realization 03)

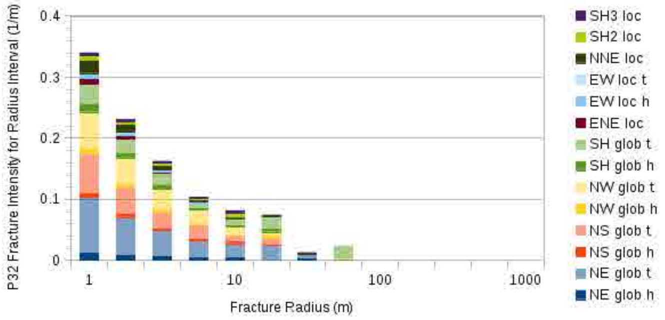

c) Simulated distribution (Realization 04)

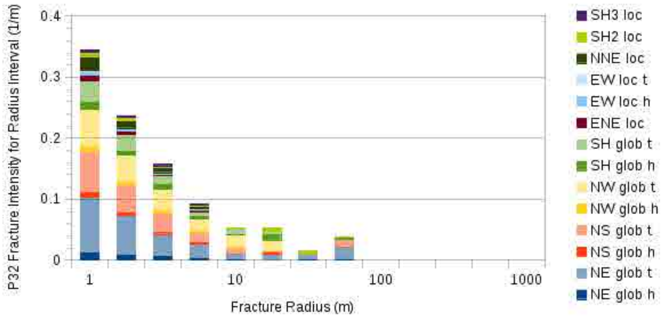

Figure A2-4. Comparison of theoretical and simulated increments of P_{32} fracture intensity for each of the fracture sets in the elevated-P_{32} variant of the r0-fixed model, for realizations 03 and 04. Abbreviations in the legend are: glob = global, loc = local, h = hydro, and t =tight. Each histogram bar represents ¼ order of magnitude range of fracture radius, and is labeled based on the maximum radius in the interval.

Table A2-2. Theoretical (theo) versus average (avg), standard deviation (std), minimum (min), and maximum (max) values of simulated P_{32} increments for 10 realizations of the r_0-fixed base case for fracture radius [r_1, r_2]. For the largest four ranges of fracture radius, no fractures were generated in any of the 10 realizations, so this is indicated just by listing the zero values for the maximum P_{32}.

r_1 (m)	r_2 (m)		Total P32 (1/m)	NE global hydro	NS global hydro	NW global hydro	SH global hydro	EW local hydro	NE global tight	NS global tight	NW global tight	SH global tight	ENE local	EW local tight	NNE local	SH2 local	SH3 local
0.3	0.32	theo	0.0488	0.0017	0.0010	0.0009	0.0015	0.0008	0.0132	0.0098	0.0077	0.0043	0.0018	0.0005	0.0044	0.0007	0.0006
		avg	0.0460	0.0016	0.0010	0.0009	0.0014	0.0007	0.0125	0.0092	0.0073	0.0041	0.0017	0.0004	0.0041	0.0007	0.0006
		std	0.0002	0.0001	0.0001	0.0001	0.0001	0.0000	0.0001	0.0002	0.0001	0.0001	0.0001	0.0000	0.0001	0.0000	0.0000
		min	0.0457	0.0014	0.0009	0.0008	0.0013	0.0007	0.0123	0.0089	0.0071	0.0040	0.0016	0.0004	0.0040	0.0007	0.0005
		max	0.0464	0.0017	0.0010	0.0010	0.0015	0.0008	0.0126	0.0095	0.0074	0.0042	0.0017	0.0005	0.0042	0.0007	0.0006
0.32	0.56	theo	0.4276	0.0145	0.0089	0.0083	0.0133	0.0062	0.1158	0.0854	0.0701	0.0393	0.0144	0.0038	0.0355	0.0067	0.0055
		avg	0.4443	0.0151	0.0093	0.0086	0.0139	0.0064	0.1200	0.0889	0.0734	0.0411	0.0146	0.0039	0.0365	0.0070	0.0057
		std	0.0012	0.0002	0.0002	0.0002	0.0003	0.0002	0.0006	0.0005	0.0004	0.0004	0.0004	0.0001	0.0003	0.0002	0.0006
		min	0.4426	0.0148	0.0090	0.0084	0.0134	0.0062	0.1192	0.0880	0.0727	0.0404	0.0139	0.0038	0.0360	0.0067	0.0055
		max	0.4462	0.0154	0.0098	0.0089	0.0143	0.0067	0.1213	0.0897	0.0739	0.0419	0.0153	0.0042	0.0370	0.0072	0.0060
0.56	1	theo	0.2828	0.0096	0.0058	0.0058	0.0095	0.0036	0.0765	0.0554	0.0493	0.0281	0.0082	0.0022	0.0200	0.0047	0.0039
		avg	0.2848	0.0098	0.0057	0.0060	0.0097	0.0037	0.0765	0.0559	0.0497	0.0287	0.0082	0.0022	0.0200	0.0048	0.0040
		std	0.0019	0.0005	0.0002	0.0003	0.0002	0.0002	0.0011	0.0012	0.0006	0.0007	0.0003	0.0002	0.0006	0.0002	0.0057
		min	0.2819	0.0092	0.0054	0.0056	0.0095	0.0033	0.0745	0.0545	0.0488	0.0276	0.0078	0.0020	0.0193	0.0046	0.0037
		max	0.2884	0.0105	0.0062	0.0063	0.0102	0.0041	0.0780	0.0578	0.0504	0.0297	0.0089	0.0026	0.0212	0.0051	0.0042
1	1.78	theo	0.1878	0.0063	0.0038	0.0041	0.0068	0.0021	0.0506	0.0360	0.0347	0.0202	0.0047	0.0013	0.0112	0.0033	0.0027
		avg	0.1953	0.0066	0.0038	0.0042	0.0069	0.0022	0.0526	0.0375	0.0362	0.0213	0.0048	0.0012	0.0115	0.0036	0.0030
		std	0.0021	0.0007	0.0004	0.0006	0.0008	0.0003	0.0014	0.0009	0.0013	0.0005	0.0003	0.0001	0.0007	0.0003	0.0040
		min	0.1924	0.0059	0.0033	0.0033	0.0060	0.0017	0.0505	0.0359	0.0340	0.0204	0.0044	0.0011	0.0107	0.0032	0.0024
		max	0.1987	0.0079	0.0046	0.0053	0.0085	0.0026	0.0545	0.0385	0.0383	0.0219	0.0052	0.0015	0.0130	0.0041	0.0033
1.78	3.16	theo	0.1253	0.0042	0.0024	0.0029	0.0049	0.0013	0.0334	0.0234	0.0244	0.0144	0.0027	0.0008	0.0063	0.0023	0.0019
		avg	0.1314	0.0045	0.0025	0.0029	0.0057	0.0014	0.0333	0.0248	0.0262	0.0157	0.0030	0.0008	0.0063	0.0025	0.0019
		std	0.0053	0.0007	0.0006	0.0007	0.0007	0.0005	0.0030	0.0013	0.0010	0.0009	0.0006	0.0003	0.0010	0.0005	0.0030
		min	0.1212	0.0037	0.0017	0.0020	0.0048	0.0008	0.0276	0.0224	0.0245	0.0141	0.0020	0.0003	0.0050	0.0019	0.0015
		max	0.1381	0.0061	0.0039	0.0041	0.0067	0.0024	0.0367	0.0269	0.0275	0.0168	0.0039	0.0014	0.0082	0.0034	0.0028
3.16	5.62	theo	0.0839	0.0028	0.0016	0.0020	0.0035	0.0007	0.0221	0.0152	0.0172	0.0103	0.0015	0.0005	0.0036	0.0016	0.0014
		avg	0.0860	0.0032	0.0017	0.0018	0.0028	0.0006	0.0240	0.0158	0.0178	0.0098	0.0015	0.0003	0.0035	0.0017	0.0016
		std	0.0053	0.0012	0.0007	0.0009	0.0012	0.0006	0.0012	0.0029	0.0034	0.0019	0.0008	0.0003	0.0011	0.0005	0.0021
		min	0.0769	0.0012	0.0002	0.0005	0.0016	0	0.0223	0.0103	0.0135	0.0059	0.0004	0.0000	0.0025	0.0005	0.0005
		max	0.0957	0.0049	0.0027	0.0032	0.0050	0.0018	0.0258	0.0206	0.0252	0.0127	0.0026	0.0008	0.0061	0.0023	0.0029
5.62	10	theo	0.0564	0.0018	0.0010	0.0014	0.0025	0.0004	0.0146	0.0099	0.0121	0.0074	0.0009	0.0003	0.0020	0.0012	0.0010
		avg	0.0567	0.0018	0.0010	0.0010	0.0017	0.0003	0.0145	0.0103	0.0130	0.0072	0.0011	0.0005	0.0025	0.0008	0.0010
		std	0.0088	0.0012	0.0011	0.0009	0.0017	0.0006	0.0051	0.0033	0.0042	0.0024	0.0016	0.0007	0.0020	0.0007	0.0021
		min	0.0435	0.0005	0	0	0	0	0.0060	0.0067	0.0073	0.0036	0	0	0.0003	0	0
		max	0.0727	0.0040	0.0035	0.0021	0.0055	0.0018	0.0212	0.0170	0.0216	0.0105	0.0039	0.0018	0.0066	0.0021	0.0027
10	17.8	theo	0.0381	0.0012	0.0007	0.0010	0.0018	0.0003	0.0096	0.0064	0.0085	0.0053	0.0005	0.0002	0.0011	0.0008	0.0007
		avg	0.0340	0.0014	0.0011	0.0004	0.0023	0.0001	0.0107	0.0062	0.0065	0.0029	0.0000	0.0003	0.0006	0.0010	0.0006
		std	0.0113	0.0020	0.0024	0.0013	0.0030	0.0002	0.0061	0.0056	0.0035	0.0027	0.0001	0.0009	0.0012	0.0016	0.0018
		min	0.0175	0	0	0	0	0	0.0024	0.0003	0.0024	0	0	0	0	0	0
		max	0.0540	0.0060	0.0073	0.0040	0.0069	0.0007	0.0206	0.0199	0.0150	0.0088	0.0004	0.0028	0.0037	0.0050	0.0035
17.8	31.6	theo	0.0257	0.0008	0.0004	0.0007	0.0013	0.0002	0.0064	0.0042	0.0060	0.0038	0.0003	0.0001	0.0006	0.0006	0.0005
		avg	0.0205	0.0006	0	0.0010	0.0008	0	0.0057	0.0036	0.0043	0.0030	0	0.0002	0.0001	0.0012	0.0000
		std	0.0089	0.0010	0	0.0023	0.0018	0	0.0040	0.0042	0.0062	0.0034	0	0.0005	0.0004	0.0028	0.0013
		min	0.0106	0	0	0	0	0	0	0	0	0	0	0	0	0	0
		max	0.0389	0.0025	0	0.0072	0.0058	0	0.0123	0.0115	0.0173	0.0101	0	0.0015	0.0011	0.0080	0.0002
31.6	56.2	theo	0.0175	0.0005	0.0003	0.0005	0.0009	0.0001	0.0042	0.0027	0.0042	0.0027	0.0002	0.0001	0.0004	0.0004	0.0003
		avg	0.0203	0.0002	0	0.0001	0.0011	0	0.0088	0.0018	0.0054	0.0009	0	0	0	0.0020	0
		std	0.0119	0.0005	0	0.0004	0.0029	0	0.0095	0.0039	0.0073	0.0016	0	0	0	0.0041	0
		min	0	0	0	0	0	0	0	0	0	0	0	0	0	0	0
		max	0.0363	0.0015	0	0.0014	0.0094	0	0.0221	0.0125	0.0221	0.0042	0	0	0	0.0105	0
56.2	100	theo	0.0119	0.0003	0.0002	0.0004	0.0007	0.0001	0.0028	0.0018	0.0030	0.0019	0.0001	0.0000	0.0002	0.0003	0.0002
		max	0	0	0	0	0	0	0	0	0	0	0	0	0	0	0
100	178	theo	0.0081	0.0002	0.0001	0.0002	0.0005	0.0000	0.0018	0.0011	0.0021	0.0014	0.0001	0.0000	0.0001	0.0002	0.0002
		max	0	0	0	0	0	0	0	0	0	0	0	0	0	0	0
178	316	theo	0.0055	0.0002	0.0001	0.0002	0.0003	0.0000	0.0012	0.0007	0.0015	0.0010	0.0000	0.0000	0.0001	0.0001	0.0001
		max	0	0	0	0	0	0	0	0	0	0	0	0	0	0	0
316	562	theo	0.0038	0.0001	0.0001	0.0001	0.0002	0.0000	0.0008	0.0005	0.0010	0.0007	0.0000	0.0000	0.0000	0.0001	0.0001
		max	0	0	0	0	0	0	0	0	0	0	0	0	0	0	0

The absence of a P_{32} contribution from fractures larger than the range (101.5 m, 101.75 m) ≈ (31.6 m, 56.2 m) is found to be a result of the discrete nature of the pseudo-random number generator that is used for Monte Carlo simulation of the fracture size distribution, in combination with the low minimum radius (0.3 m). The pseudo-random number generator (based on an algorithm given by Press et al., 1986) produces 714025 discrete values on the interval [0, 1). In combination with the algorithm used for generating values of r from a power-law distribution, this leads to an effective maximum radius:

rmax ,eff = rmin · exp[−log(1−1/714025)kr]

For the main (global) fracture sets and the subhorizontal local sets which account for 83% of the total P_{32}, the value of rmax,eff varies from 40.7 m to 55.8 m. In terms of fracture intensity the fracturesin these sets with radius r in the range rmax,eff < r <rmax account for 0.0348 m2/m3. The EW, ENE, and NNE local sets have lower rmax, eff values in the range 26.9 m to 29.9 m, but due to their much lower intensity they account for only 0.00165 m2/m3 of the fracture intensity.

These increments of P_{32} are a small percentage of the total P_{32} of 1.330 m2/m3 for fractures in the simulated range (r > 0.3 m) However fractures larger than rmax,eff, if they happen to intersect the 50m block, would tend to be through-cutting features.

The implications of omitting these fractures has been addressed by producing supplementary datasets for fractures in the size range rmax, eff < r < rmax, as described in a separate memorandum(dated 28 Mar 2014). When combined with the datasets from this delivery, these fractures cover the full range of sizes from r = 0.3 m to 564.2 m. The total fracture intensity that results from combining the supplementary datasets with the datasets described in this memorandum is about2.6% higher than the specified value ofP_{32}.

Quality Check 2: Fracture orientation distributions

The simulated fracture orientation distributions have been confirmed both quantitatively by statistical measures, and qualitatively by equal-area stereonet plots for individual fracture sets.

The consistency of the fitted Fisher mean poles (mean pole trend and plunge in degrees, as given in parentheses) and concentration parameters κ in the following listing have been checked against the same parameters for the same 14 sets as listed in Table 1.

The mean pole directions are generally in very close agreement, usually within a fraction of a degree (somewhat larger for the Hydro-DFN sets which represent a smaller sample). It should be noted that for Set 9 (SH global/tight), fitted values for trend and plunge such as (359.34, 87.37) are in close agreement with the specified values (0.8, 87.3) when it is recalled that the azimuth of strike is a cyclic value. Similarly for Set 12, fitted directions such as (113.75, 0.10) are in close agreement with the specified value of (293.8, 0.0) when it is considered that fracture poles are bidirectional so can be represented equivalently by a direction that is 180 degrees opposed.

Values of the Fisher concentration κ in general agree with the specified values within 5%. Supplementary to these quantitative checks, stereonet plots were also produced for graphical comparison. These are shown for Realization 01 of the base case in Figures A2-5 through A2-7. Plots were generated for all realizations including both the base case and the elevated-P_{32} variant. Although only plots for realization 01 of the base case are shown here, visual comparison of all plots was done by means of "thumbnail" versions of these plots such as illustrated in Figure 8.

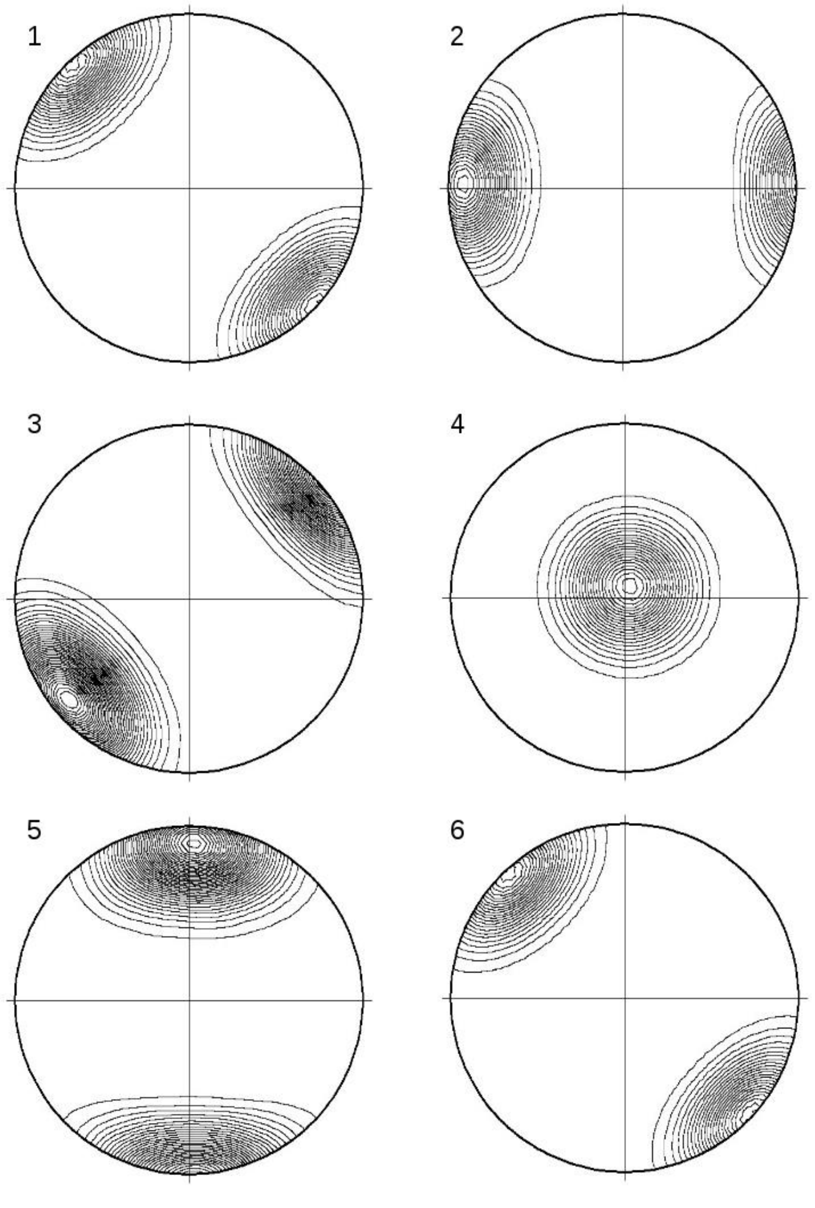

Figure A2-5. Equal-area stereonet plots of simulated fracture pole directions for the first six fracture sets in the r0-fixed base case model:(1) NE global/hydro, (2) NS global/hydro, (3) NW global/hydro, (4) SH global/hydro, (5) EW local, and (6) NE global/tight.

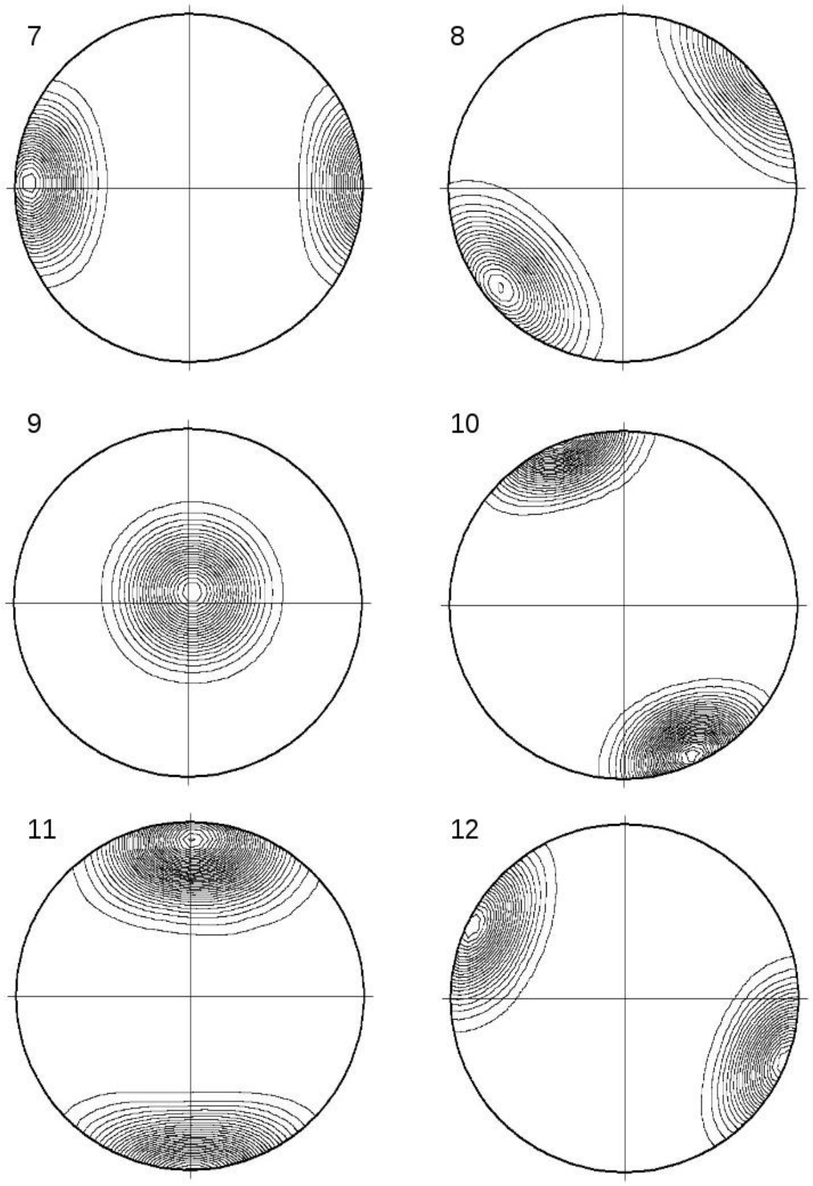

Figure A2-6. Equal-area stereonet plots of simulated fracture pole directions for fracture sets 7 through 12 in the r0-fixed base case model: ,(7) NS global/tight, (8) NW global/tight, (9) SH global/tight, (10) ENE local, (11) EW local/tight, and (12) NNE local.

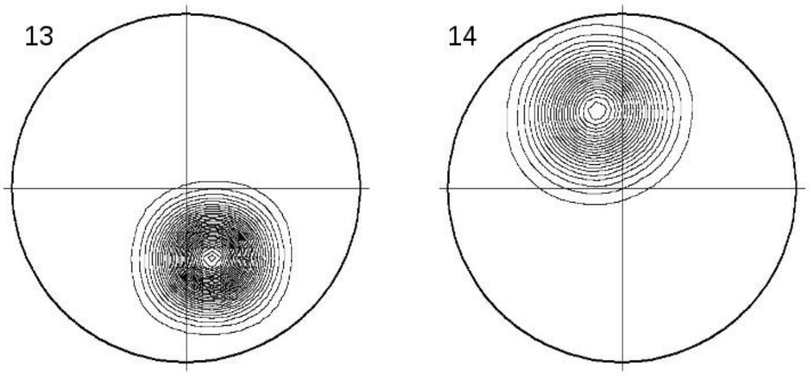

Figure A2-7. Equal-area stereonet plots of simulated fracture pole directions for the last two fracture sets in the r0-fixed base case model: (13) SH2 local, and (14) SH3 local.

Quality Check 3: Comparison of expected and simulated P21 fracture intensity on the sampling plane

The third main check of quality is to compare the observed values of fracture intensity as measured in the same 2-D cross-sections for which data area delivered, in terms of the P21 fracture intensity (trace length per unit area). This can be estimated from the volumetric fracture intensity P_{32}, after correcting for the effects of truncating the fracture size distribution by thinning out the fractures smaller than 0.3 m radius, and the orientation bias that results from the orientation of sampling planes (either horizontal, vertical with strike N35W, or vertical with strike N55E) relative to the fractures in each fracture set. The orientation bias is quantified by the factor C23 as defined by Wang (2005; see Geier, 2014 for details and method of calculation). The results are listed in Table 3. The expected P21 values for the elevated-P_{32} variant can be calculated simply by scaling the values in Table 3 by a factor of 1.2. The expected P_{21} values can be compared with the total fracture trace length per unit area of the cross-section. This needs to be taken in the portion of the model within the volume that has been focused on for the repository simulates, to avoid other censoring effects. The results as shown in Table 4 (for the base case) and Table 5 (for the elevated-P_{32} variant) show generally good agreement. For both the base case and the elevated-P_{32} variant, the average simulated P21 over 10 realizations is within about 1% of the expected value, for all three cross-section orientations.

Table A2-3. Parameters for fracture sets for the r0-fixed base case, and resulting values of truncated P32 (for minimum fracture radius of 0.3 m), and corresponding values of the geometric factor C23 and P21.

FFM01	**Mean pole trend**	**Mean pole plunge**	**Fisher conc. κ**	P_{32} **(unscaled)**	P_{32} **(scaled)**	**Horizontal**			**Vertical N35W**			**Vertical N55E**		
						ρ	$1/C_{23}$	P_{21}	**ρ**	$1/C_{23}$	P_{21}	**ρ**	$1/C_{23}$	P_{21}
NE global (hydro)	314.9	1.3	20.94	0.193	0.0434	88.7	0.98	0.0423	79.9	0.96	0.0417	10.2	0.31	0.0134
NS global (hydro)	270.1	5.3	21.34	0.122	0.0258	84.7	0.97	0.0251	35.4	0.60	0.0154	55.1	0.81	0.0209
NW global (hydro)	230.1	4.6	15.70	0.100	0.0280	85.4	0.97	0.0270	6.7	0.32	0.0090	85.1	0.97	0.0270
SH global (hydro)	0.8	87.3	17.42	0.158	0.0469	2.7	0.30	0.0139	88.4	0.97	0.0455	87.8	0.97	0.0455
EW local (hydro)	0.4	11.9	13.89	0.105	0.0154	78.1	0.94	0.0145	55.5	0.81	0.0124	37.1	0.62	0.0095
NE global (tight)	314.9	1.3	20.94	1.540	0.3461	88.7	0.98	0.3378	79.9	0.96	0.3329	10.2	0.31	0.1064
NS global (tight)	270.1	5.3	21.34	1.170	0.2474	84.7	0.97	0.2407	35.4	0.59	0.1470	55.1	0.81	0.2004
NW global (tight)	230.1	4.6	15.70	0.848	0.2374	85.4	0.97	0.2293	6.7	0.32	0.0766	85.1	0.97	0.2292
SH global (tight)	0.8	87.3	17.42	0.466	0.1383	2.7	0.30	0.0411	88.4	0.97	0.1344	87.8	0.97	0.1343
ENE local	157.5	3.1	34.11	0.256	0.0345	86.9	0.98	0.0339	77.5	0.96	0.0332	12.9	0.29	0.0101
EW local (tight)	0.4	11.9	13.89	0.064	0.0094	78.1	0.95	0.0088	55.5	0.81	0.0076	37.1	0.62	0.0058
NNE local	293.8	0.0	21.79	0.658	0.0833	90	0.98	0.0814	58.8	0.84	0.0703	31.2	0.54	0.0451
SH2 local	164.0	52.6	35.43	0.081	0.0227	37.4	0.61	0.0139	78.6	0.97	0.0219	55.0	0.81	0.0184
SH3 local	337.9	52.9	17.08	0.067	0.0188	37.1	0.62	0.0116	82.3	0.96	0.0181	54.0	0.80	0.0150
Total				5.828	1.2971			1.1215			0.9660			0.8811

Table A2-4. Comparison of expected and simulated values of P21 for the r0-fixed base case.

Realization	Horizontal Section P_{21}	Vertical N35W P_{21}	Vertical N55E P_{21}
01	1.1033	0.9419	0.8871
02	1.1618	0.9794	0.9268
03	1.1131	0.9844	0.9478
04	1.0964	0.9165	0.8710
05	1.1596	0.9840	0.9057
06	1.1220	0.9958	0.8690
07	1.1268	0.9298	0.8947
08	1.1100	0.9425	0.8673
09	1.1632	0.9732	0.8704
10	1.1261	0.9946	0.8531
Expected	1.1215	0.9660	0.8811
Average	1.1282	0.9642	0.8893
Ratio	1.0060	0.9981	1.0093

Table A2-5. Comparison of expected and simulated values of P21 for for the r0-fixed, elevated-P32 case.

Realization	Horizontal Section P_{21}	Vertical N35W P_{21}	Vertical N55E P_{21}
01	1.3293	1.1672	1.0707
02	1.3665	1.1765	1.0838
03	1.3174	1.1766	1.1269
04	1.3372	1.1073	1.0570
05	1.3853	1.1910	1.1434
06	1.3510	1.2099	1.0562
07	1.3681	1.1028	1.0583
08	1.3025	1.1433	1.0427
09	1.3835	1.1866	1.0415
10	1.3460	1.1819	1.0059
Expected	1.3458	1.1592	1.0573
Average	1.3487	1.1643	1.0686
Ratio	1.0021	1.0044	1.0107

References

Baecher GB, Lanney NA, Einstein HH (1977) Statistical description of rock properties and sampling. In: Proceedings of the 18th U.S. Symposium on Rock Mechanics, American Institute of Mining Engineers, 5C1-8.

Dershowitz WS, Herda H (1992) Interpretation of fracture spacing and intensity. In: Proceedings, 32nd US rock mechanics symposium, Santa Fe, New Mexico.

Dershowitz W, Lee G, Geier J, Foxford T, LaPointe P, Thomas A (2004) FracMan, interactive discrete feature data analysis, geometric modelling, and exploration simulation. User documentation. Golder Associates Inc, Seattle, Washington

Fox A, La Pointe P, Hermanson J and Öhman, J (2007). Statistical geological discrete fracture network model. Forsmark modelling stage 2.2. SKB R-07-46, Swedish Nuclear Fuel and Waste Management Co (SKB).

Selroos J-O, Sven F (2009), SR-Site groundwater flow modeling methodology, setup and results. SKB R-09-22, Swedish Nuclear Fuel and Waste Management Co (SKB).

APPENDIX 3

Thermo-mechanical modelling – Supplementary results

In this Appendix, evolution of stresses in horizontal (x-direction in 2D modelling) and vertical directions (y-direction in 2D modelling) and total displacements of thermo-mechanical analysis are presented as five cases; no fracture model in Figure A3-1, NE02 DFN model in Figure A3-2, elevated NE02 DFN model in Figure A3-3, NW02 DFN model in Figure A3-4 and HZ02 DFN model in Figure A3-5. The evolutions of five cases are similar although there are some effect of the presence of fractures and geometry. The general observations are summarized as follows;

- The increase of horizontal stress from the heat of the spent nuclear fuel is in the order of 20 MPa, and stresses actually recover to the initial state after about 1,000 years.
- The change of vertical stress is negligible except the region close, e.g., 2 m, to the repository tunnel. This is explained by the fact that the overlying rock is free to expand in the vertical direction at the ground surface.
- The increases of horizontal stress are much greater than the vertical stress, and this results in the increase of the stress ratio of horizontal stress to vertical stress at the repository level and above. This increase of stress ratio can induce more failure of fractures in the repository.
- Total displacement evolution in the rock shows that the rock undergoes heaving due to the heating and expansion. When the rock cools down, it eventually recovers to the initial state.
- It is noted that the recovery of stress and total displacement in the rock are contrary to the irreversible displacement in the fractures, which were observed in Figure 36 and Figure 40.

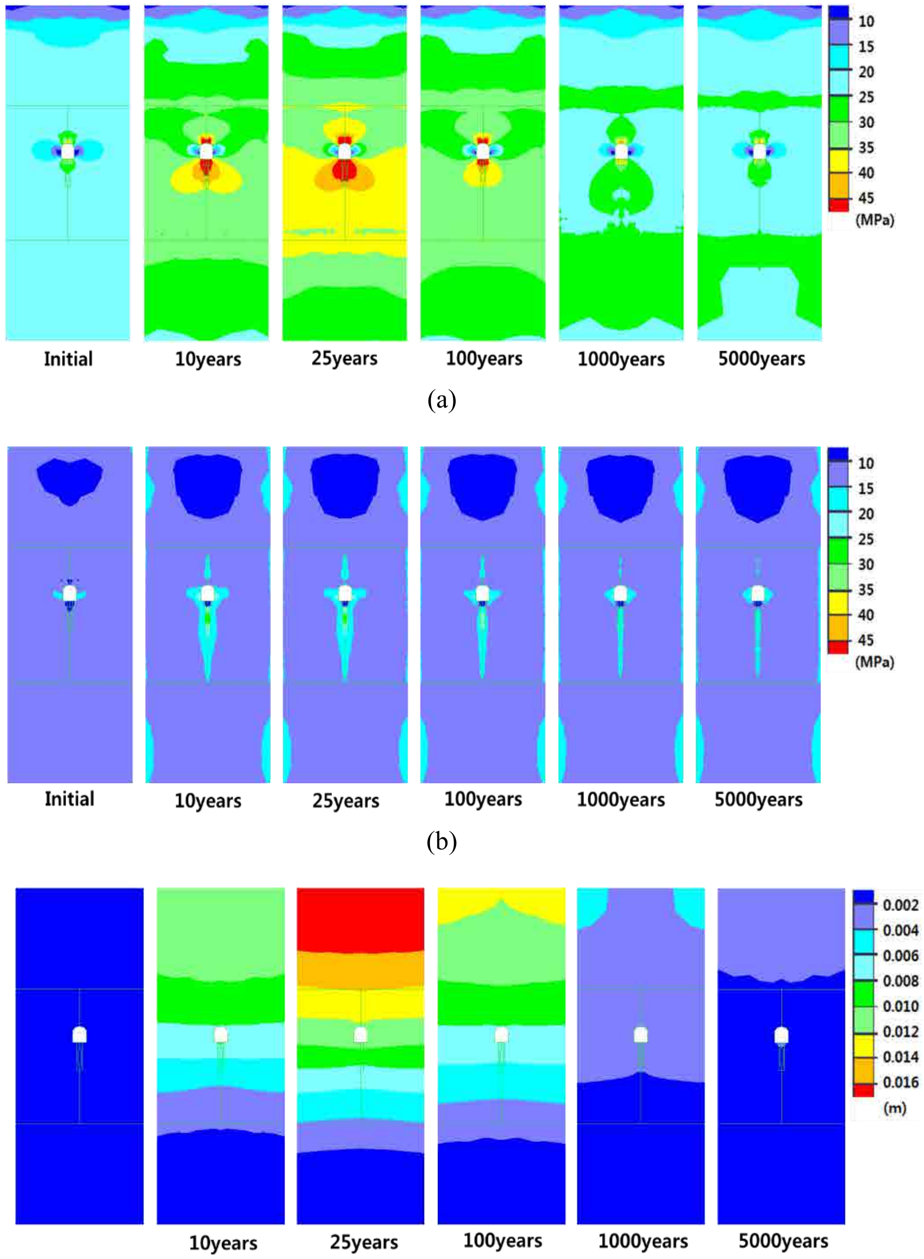

(a)

(b)

(c)

Figure A3-1. Evolution of stresses and displacements around repository during the thermal phase until 5000 years after deposition of the canisters. The model does not contain any fractures. (a) Horizontal stress, (b) vertical stress and (c) total displacement.

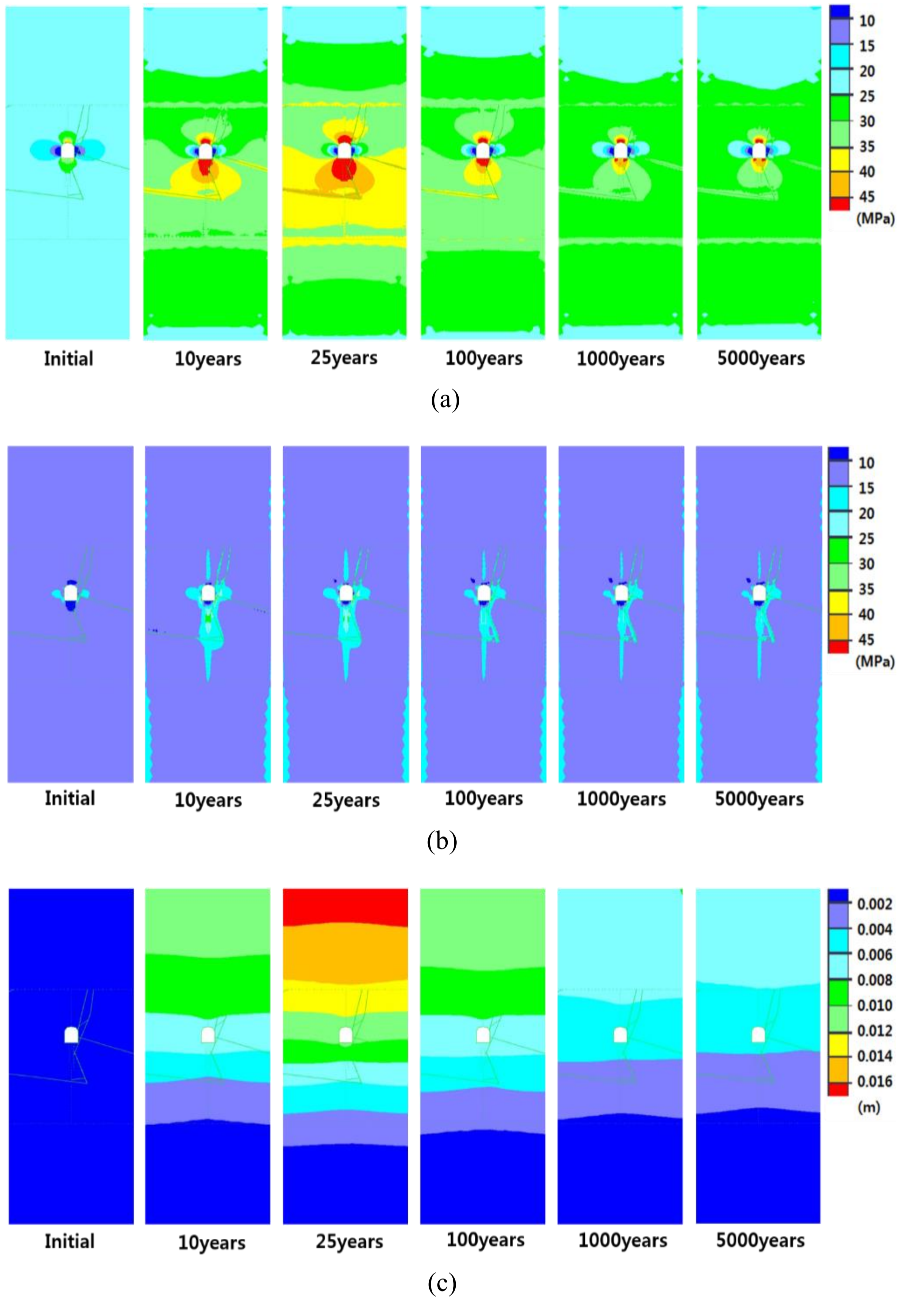

Figure A3-2. Stress and displacement evolution around the repository of T_NE02 model during the thermal phase until 5000 years after deposition of the canisters. The fractures are explicitly modelled. (a) Horizontal stress, (b) vertical stress and (c) total displacement.

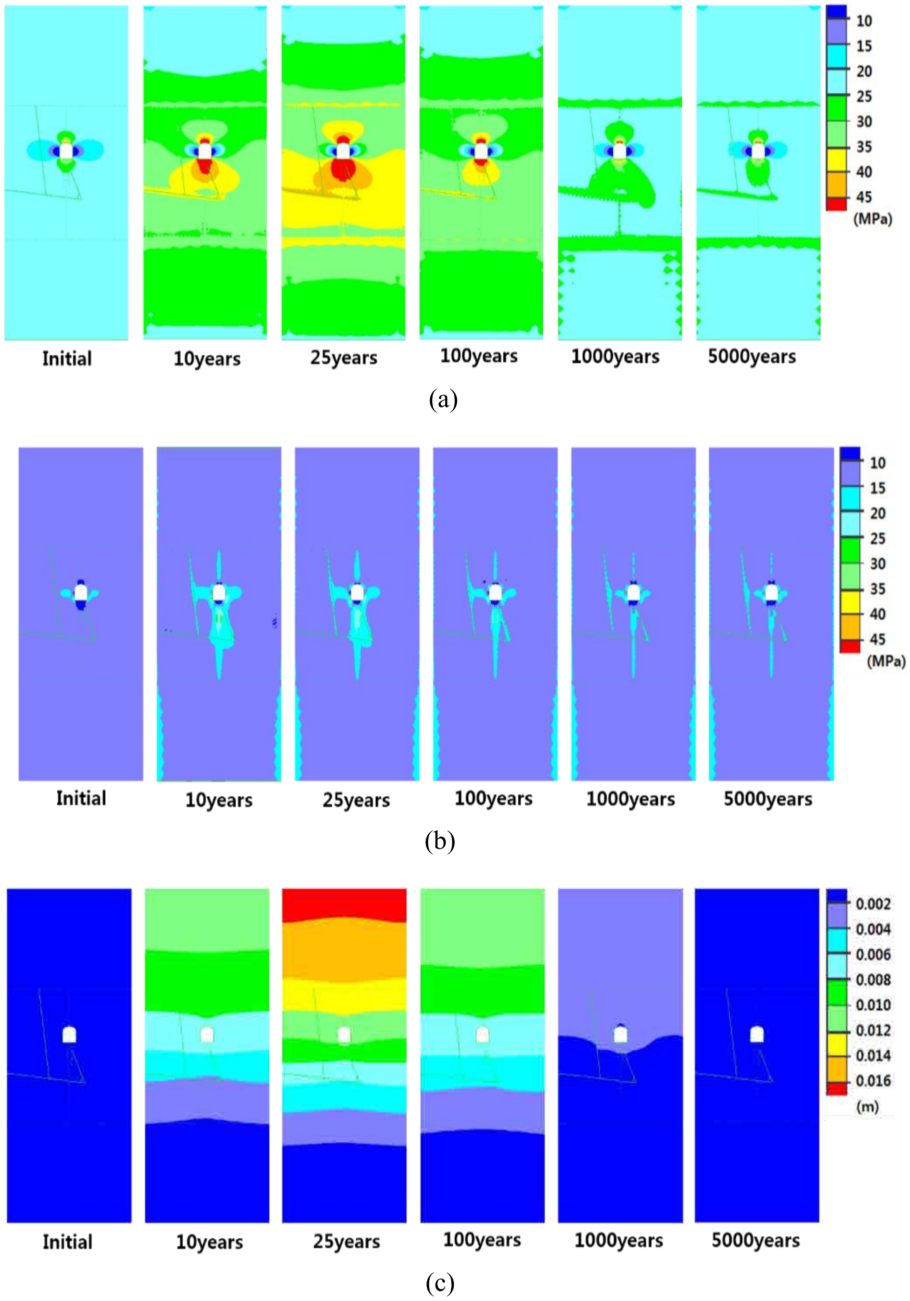

Figure A3-3. Stress and displacement evolution around the repository of T_elNE02 model during the thermal phase until 5000 years after deposition of the canisters. The fractures are explicitly modelled. (a)\Horizontal stress, (b) vertical stress and (c) total displacement.

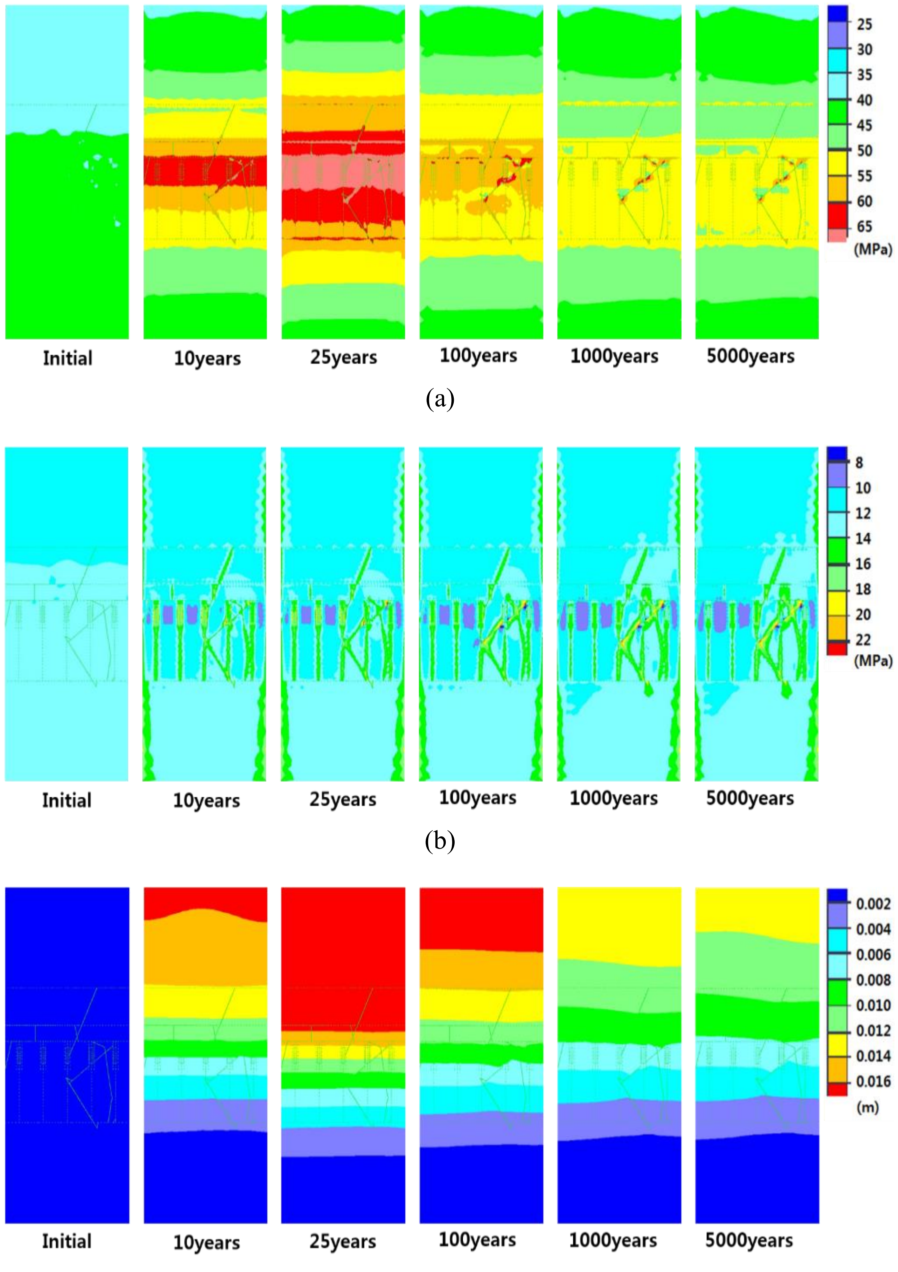

(a)

(b)

(c)

Figure A3-4. Stress and displacement evolution around the repository of T_NW02model during the thermal phase until 5000 years after deposition of the canisters. The fractures are explicitly modelled. (a) Horizontal stress, (b) vertical stress and (c) total displacement.

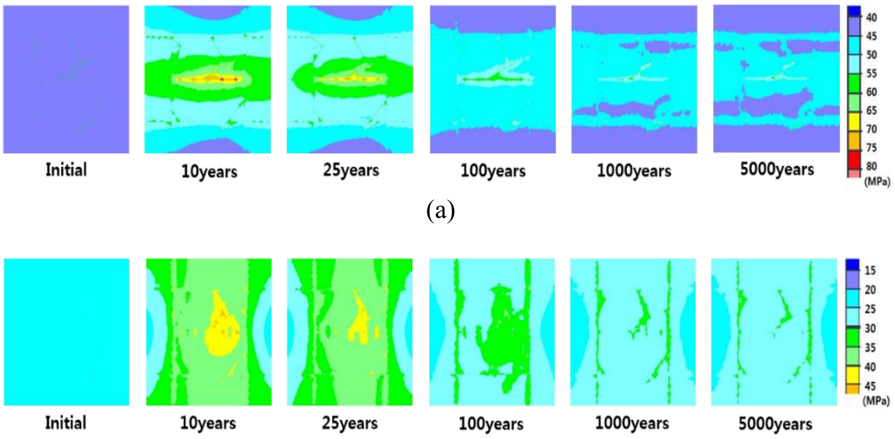

(a)

(b)

Figure A3-5. Stress and displacement evolution around the repository of T_HZ02 model during the thermal phase until 5,000 years after deposition of the canisters. The fractures are explicitly modelled. (a) Horizontal stress (maximum horizontal stress), (b) vertical stress (minimum horizontal stress).

Earthquake modelling – Supplementary results

In this Appendix, evolution of shear displacement and normal displacement are presented for different stages of the glaciation cycle, see Figure 85; T3 (38,000 years) in Figure A3-1, T4 (55,000 years) in Figure A3-2, T5 (58,000 years) for TGEQ_NE02 model and TGEQ_NW02 model.

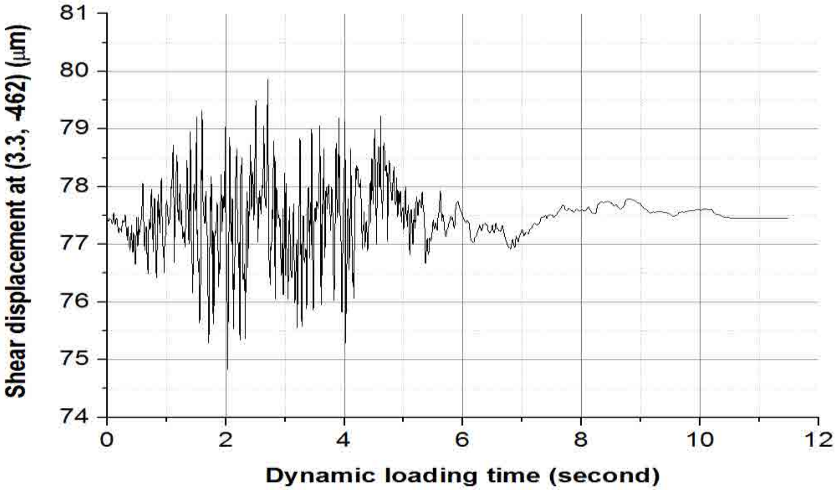

(a)

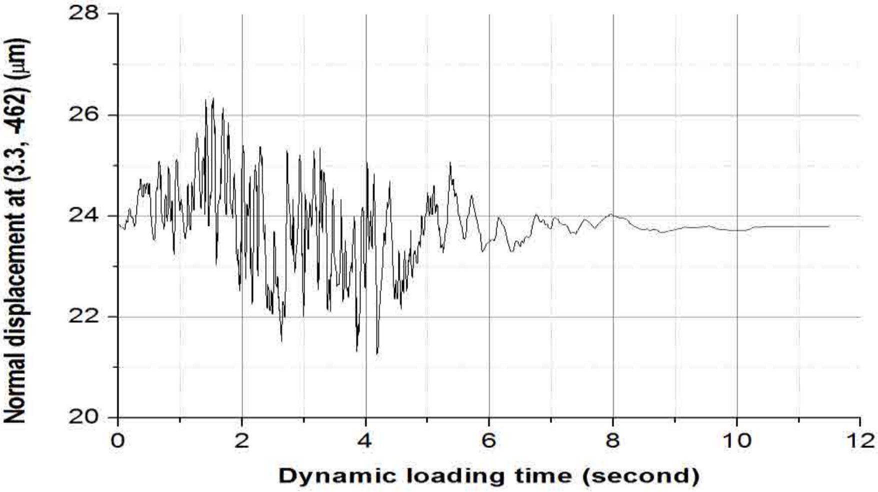

(b)

Figure A4-1. Dynamic loading at T3 (38,000 years) of TGEQ_NE02: (a) shear and (b) normal displacement at point (3.3, -462). Magnitudes of shear (from 77.39 μm to 77.45 μm) and normal displacement (from 23.84 μm to 23.79 μm) are fluctuated according to the input stress.

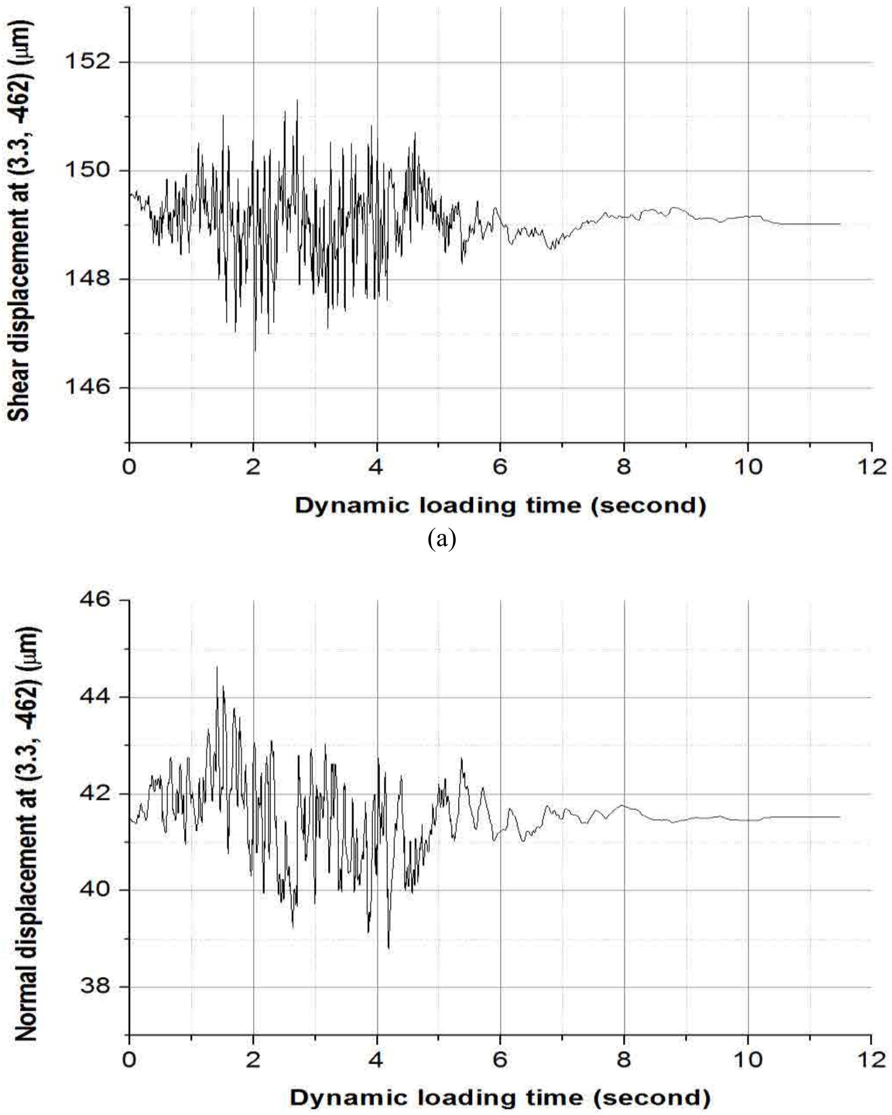

(a)

(b)

Figure A4-2. Dynamic loading at T4 (55,000 years) of TGEQ_NE02: (a) shear and (b) normal displacement at point (3.3, -462). Magnitudes of shear (from 149.62 μm to 149.02 μm) and normal displacement (from 41.44 μm to 41.53 μm) are fluctuated according to the input stress.

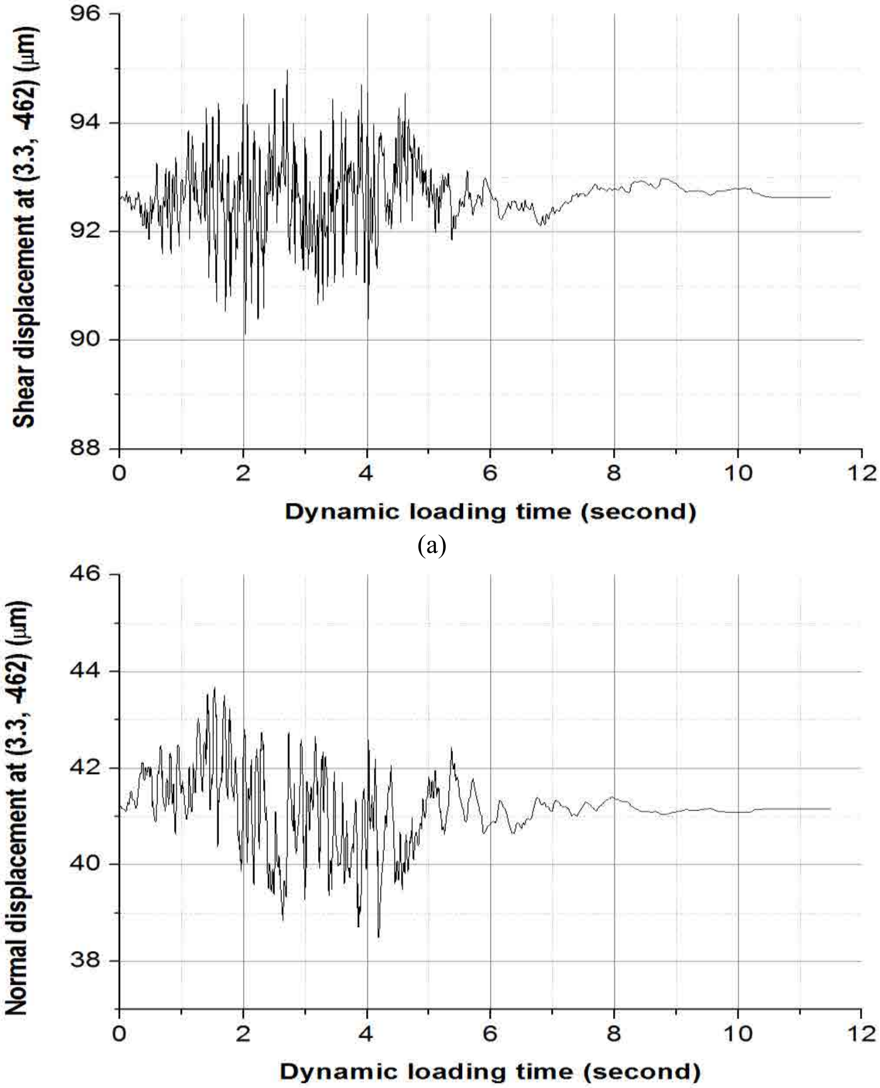

(a)

(b)

Figure A4-3. Dynamic loading at T5 (58,000 years) of TGEQ_NE02: (a) shear and (b) normal displacement at point (3.3, -462). Magnitudes of shear (from 92.62 μm to 92.64 μm) and normal displacement (from 41.20 μm to 41.16 μm) are fluctuated according to the input stress.

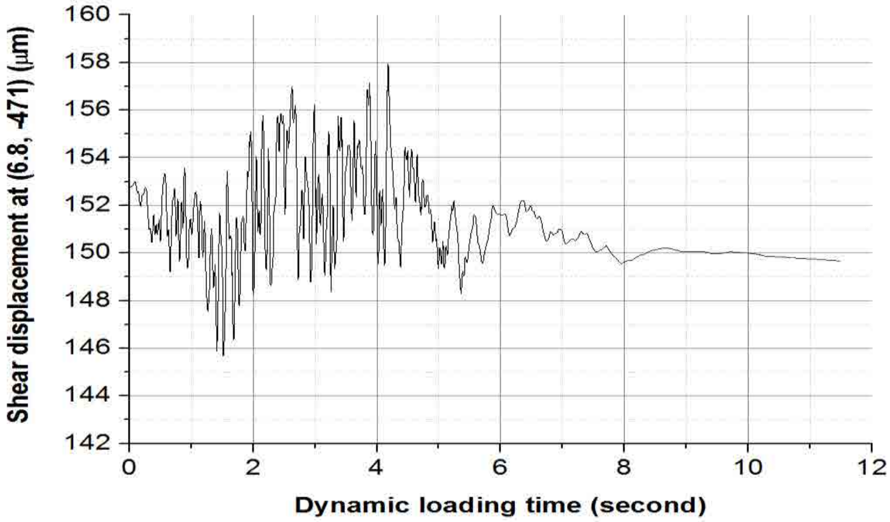

(a)

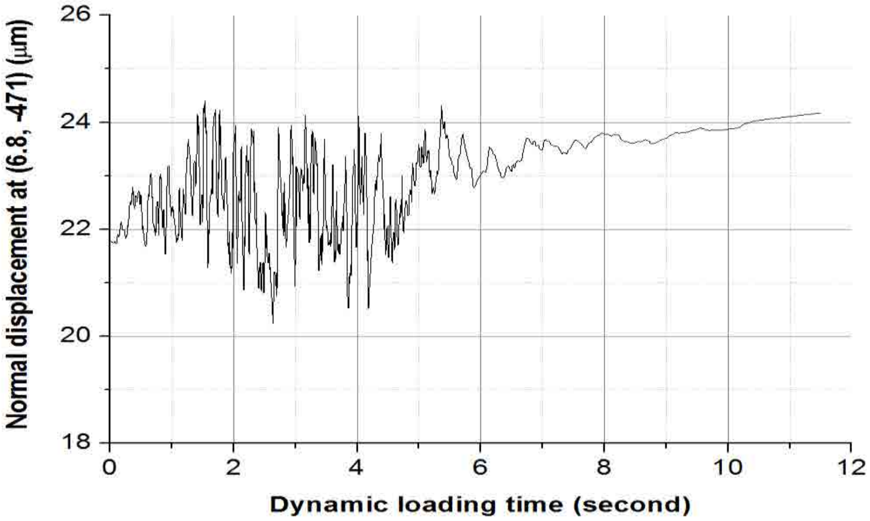

(b)

Figure A4-4. Dynamic loading at T3 (38,000 years) of TGEQ_NW02: (a) shear and (b) normal displacement at point (6.8, -471). Magnitudes of shear (from 152.8 μm to 149.7 μm) and normal displacement (from 21.78 μm to 24.17 μm) are fluctuated according to the input stress.

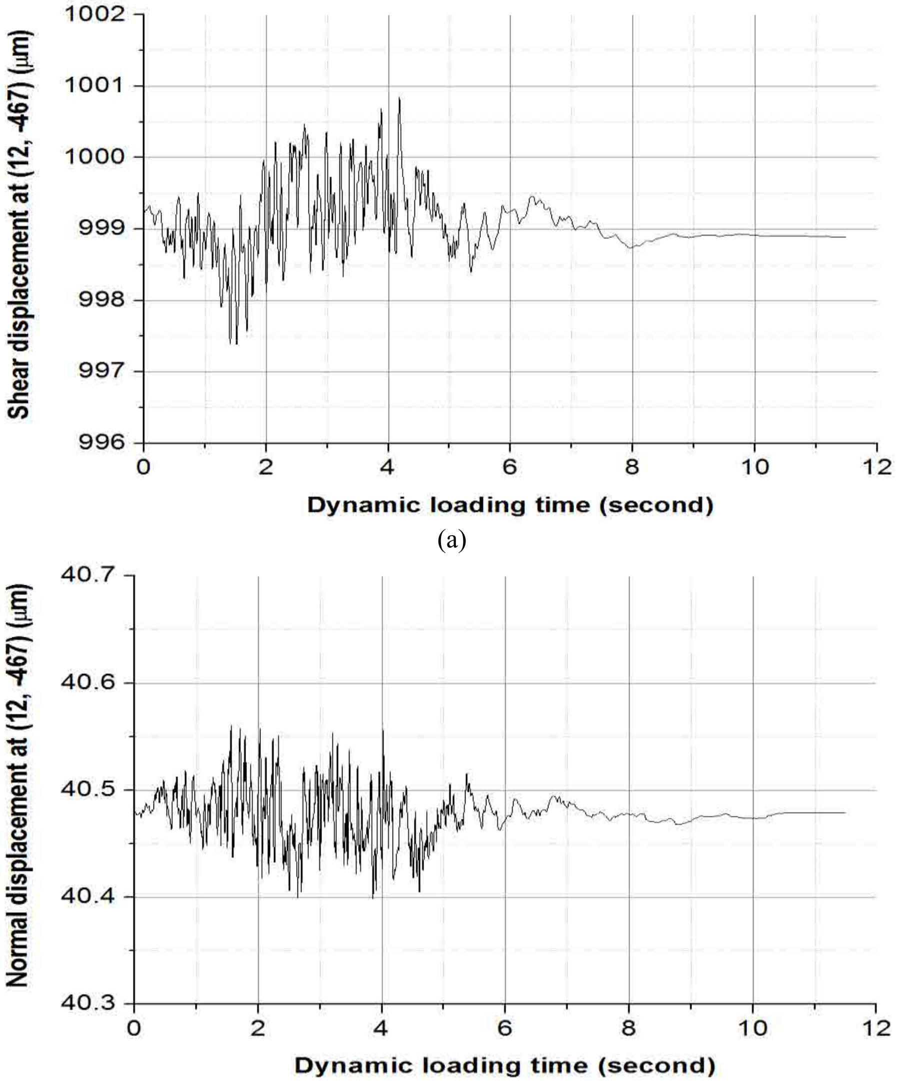

(a)

(b)

Figure A4-5. Dynamic loading at T4 (55,000 years) of TGEQ_NW02: (a) shear and (b) normal displacement at point (12, -467). Magnitudes of shear (from 999.2 μm to 998.9 μm) is fluctuated according to the input stress. Permanent normal displacement is not occurred.

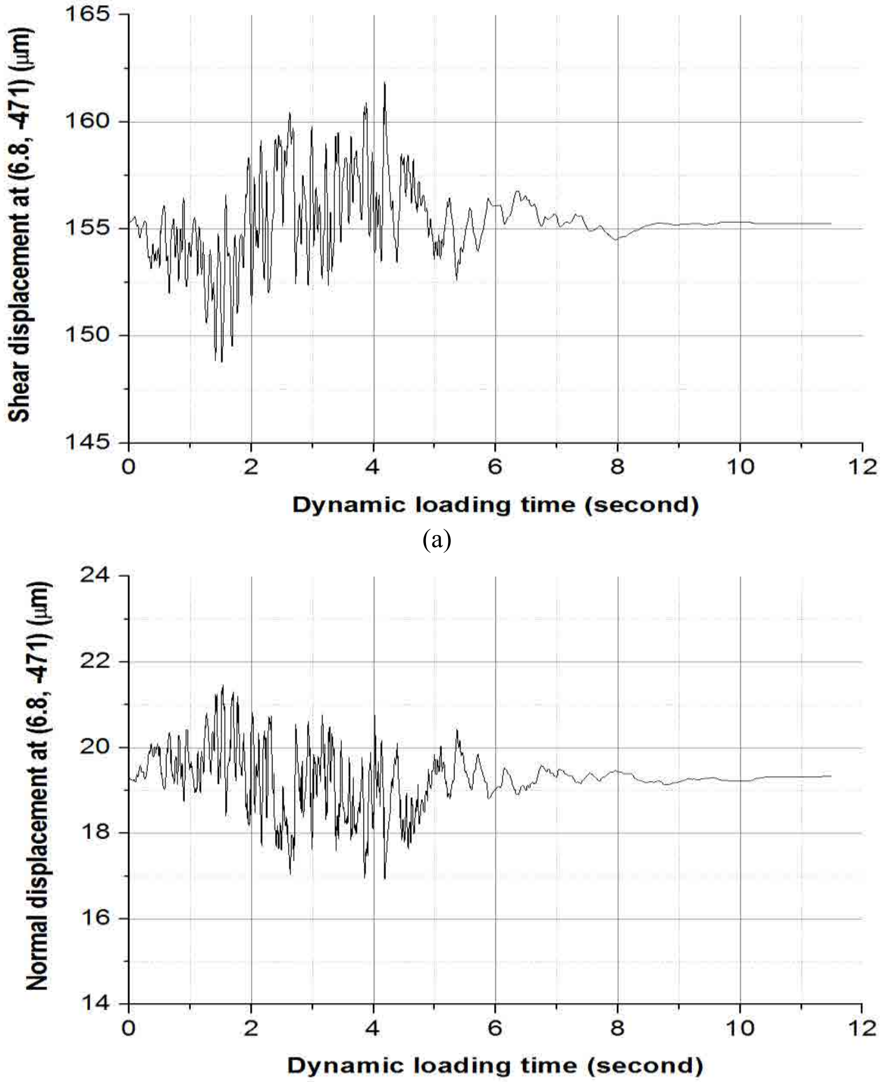

(a)

(b)

Figure A4-6. Dynamic loading at T5 (58,000 years) of TGEQ_NW02: (a) shear and (b) normal displacement at point (6.8, -471). Magnitudes of shear (starting from 155.27 μm, to 155.25 μm at the end of loading) and normal displacement (from 19.25 μm to 19.32 μm) are fluctuated according to the input stress.

2013:37

The Swedish Radiation Safety Authority has a comprehensive responsibility to ensure that society is safe from the effects of radiation. The Authority works to achieve radiation safety in a number of areas: nuclear power, medical care as well as commercial products and services. The Authority also works to achieve protection from natural radiation and to increase the level of radiation safety internationally.

The Swedish Radiation Safety Authority works proactively and preventively to protect people and the environment from the harmful effects of radiation, now and in the future. The Authority issues regulations and supervises compliance, while also supporting research, providing training and information, and issuing advice. Often, activities involving radiation require licences issued by the Authority. The Swedish Radiation Safety Authority maintains emergency preparedness around the clock with the aim of limiting the aftermath of radiation accidents and the unintentional spreading of radioactive substances. The Authority participates in international co-operation in order to promote radiation safety and finances projects aiming to raise the level of radiation safety in certain Eastern European countries.

The Authority reports to the Ministry of the Environment and has around 300 employees with competencies in the fields of engineering, natural and behavioural sciences, law, economics and communications. We have received quality, environmental and working environment certification.

Strålsäkerhetsmyndigheten
Swedish Radiation Safety Authority

SE-171 16 Stockholm
Solna strandväg 96

Tel: +46 8 799 40 00
Fax: +46 8 799 40 10

E-mail: registrator@ssm.se
Web: stralsakerhetsmyndigheten.se